COMPUTATIONAL MODELING OF INTRINSIC DISSIPATION IN NANO-STRUCTURE

BY

KUMAR KUNAL

DISSERTATION

Submitted in partial fulfillment of the requirements
for the degree of Doctor of Philosophy in Theoretical and Applied Mechanics
in the Graduate College of the
University of Illinois at Urbana-Champaign, 2016

Urbana, Illinois

Doctoral Committee:

Professor Narayana R. Aluru, Chair and Director of Research
Professor M. Taher Saif
Associate Professor Sanjiv Sinha
Assistant Professor Elif Ertekin

Abstract

In this work, using computational modeling, we study the different mechanisms of intrinsic dissipation in nano-electro mechanical systems (NEMS). We, first, use molecular dynamics (MD) simulation and gain an understanding of the underlying loss mechanisms. Using insights from the MD simulation, a multi-scale method to model intrinsic damping is developed. The high frequency vibration in NEMS have important applications. A few examples include the sensing of atomic mass, detection of biological molecules and observation of quantum effects in macroscopic objects. For all these potential applications, dissipation plays a limiting role. While a number of experimental and theoretical studies have been performed, the individual role of different mechanisms remains unclear. In this work, we attempt to isolate and understand the surface and size effect on some of the intrinsic mechanisms. We, first, consider the case of the Akhiezer damping. The Akhiezer dynamics is expected to play an important role in nano-resonators with frequencies in the GHz range. Using a judiciously devised MD set-up, we isolate Akhiezer dynamics. We show that the surfaces aid in reducing the dissipation rate through increasing the rate of thermalization of the phonons. We, next, study damping under the flexure mode of operation. A comparative analysis with the stretching mode shows that the flexure mode is less dissipative. A reduced order model is considered to understand this novel behavior. We, also, investigate the role of tension on the Q factor, a measure of the inverse of dissipation rate.

From these studies, we conclude that Akhiezer dynamics plays a dominant role in nano-resonators. We, then, develop a quasi-harmonic based multi-scale method to model Akhiezer damping. A stress component, that characterizes the non-equilibrium phonon population, is derived. We obtain constitutive relation that governs the time evolution of the non-equilibrium stress. Different methods to parametrize the constitutive relation are discussed. Using the proposed formulation, we compute the dissipation rate for different cases. The results are compared with those obtained using MD. Next, we use the Boltzmann transport equation and investigate the Q factor due to the thermo-elastic dissipation (TED). The Q factor obtained shows deviations from the classical theory of TED. Correction to the classical formula, for the case of longitudinal modes, is provided.

We, then, study damping is low dimensional structure. We first consider the case of two dimensional graphene sheet and under in-plane stretching. We show that the coupling between the in-plane and the out-of-plane motions plays an important role in the loss of mechanical energy. Further, a hysteresis behavior in the out-of-plane dynamics is observed. Next, we investigate the stretching motion of graphene nano-ribbon. A normal mode Langevin dynamics is devised to understand the results from the MD simulation.

To my family.

Table of Contents

List of Tables

List of Figures

Chapter 1

Introduction

The high frequency vibrations in nano-electro mechanical systems (NEMS) are being used for different practical applications and for the fundamental understanding of physical phenomena. A few technological applications include atomic scale mass sensors [46], detection of biological molecules [20, 27, 53] and the detection of electron spin flip [81]. NEMS devices are, also, being used to probe the fundamental physical processes in nature. For example, the observation of quantum effects in macroscopic sized nano-resonator is one of the promising goals. An important consideration for all these applications is the dissipation which limits its performance. Dissipation is often quantified in terms of a dimensionless Q factor which is defined as

$$Q = 2\pi \frac{E_{stored}}{E_{disp}}. \tag{1.1}$$

Here, E_{stored} is the maximum elastic energy stored in the structure and E_{disp} is the energy dissipated per unit period. For most applications it is desired to have low dissipation or high Q factor. For example, in-order to observe quantum effects in a nano-structure, it must be in the quantum ground state. For a resonator with angular frequency ω_n this necessitates that $\hbar\omega_n >> k_bT$. Here, $\hbar$ is the Planck's constant, ω_n is the angular frequency, k_b is the Boltzmann constant and T is the temperature. This explains the need for high values of ω_n. However, dissipation or coupling with the environment leads to thermalization and smears out the quantum effect. A low dissipation rate is, therefore, desired.

Dissipation is the process of transfer of energy from the (mechanical) motion of interest into the other degrees of freedom. The motion of interest is, often, an eigen mode of a resonator. The other degrees of freedom include the external environment as well as the internal vibrations of the structure. Depending on the medium that exchanges energy with the mode, the dissipation mechanisms can be broadly classified into the intrinsic and the extrinsic mechanisms. Extrinsic damping involves the flow of energy into the surrounding environment. Anchoring losses[7, 9, 63], fluid damping[3, 28] etc. are a few select examples of extrinsic damping. Intrinsic dissipation involves energy transfer from the mechanical mode into the lattice vibrations or the electronic degrees of freedom of the system. The known mechanism of intrinsic damping include thermo-elastic dissipation[10, 45], Akhiezer damping[32, 44], electron damping, dissipation

due to defects[62, 66] etc. Extrinsic damping can often be eliminated with better design considerations. For example, operating the structure in vacuum eliminates fluid damping, increasing the stiffness of the surrounding substrate minimizes the anchoring losses. Intrinsic damping, however, sets a fundamental upper limit for the devise performance.

Figure 1.1 illustrates the process of intrinsic loss in nano-resonators. Dissipation, for such a case, is the transfer of energy from the excited mode into the phononic bath. For structures with dimensions in the range of few nm, the natural frequency of the fundamental modes is of the order of few GHz. The thermal phonons have frequencies in the THz range. The flow of energy, then, takes place between motion with these two time-scales. It should be pointed out that we have not taken into consideration the electronic degrees of freedom. They have time-scales which is faster than that of the phonons. The Born-Oppenheimer approximation, then, suffices in most of the cases. The electrons follow the nuclear motion adiabatically, no resultant flow of energy takes place between the two sub-systems.

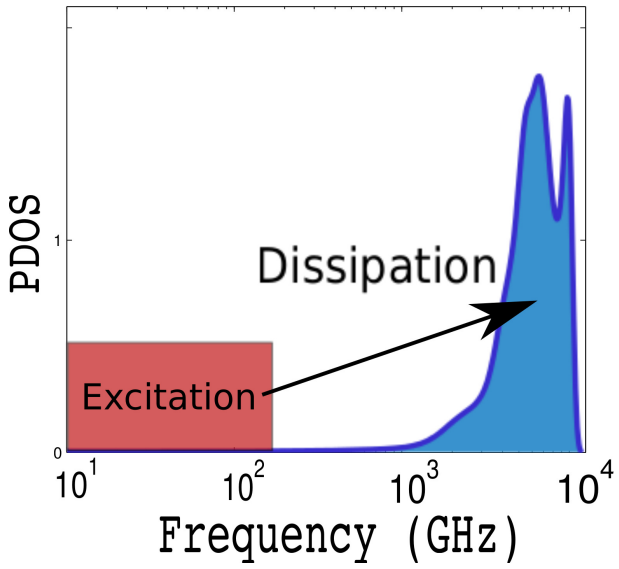

Figure 1.1: The process of intrinsic loss in nano-structures. The time-scales associated with different motions are illustrated.

A number of experimental[57, 58, 64] and theoretical studies[17, 30, 31] have been carried out to study dissipation in NEMS. These studies have shown that surfaces[12, 56] have an important role on the dissipation in nano-structure. Using experimental investigation it is, however, difficult to discern the relative role of the different mechanisms. The individual role of the different mechanisms and their scaling with size remains less well understood. In this work, using computational methods, we attempt to isolate some of the intrinsic loss mechanisms. We, then, study the effect of size and surface on these mechanisms. For this purpose, different modeling methods are employed. Non-equilibrium molecular dynamics (NEMD) is a powerful simulation

technique that can be used to probe damping in NEMS. The atomic level details provided by NEMD can be judiciously processed to gain insight into the different damping processes. The first objective of this work is to use NEMD to investigate the different intrinsic damping mechanisms operative in NEMS.

In a crystalline structure the two known intrinsic damping mechanisms are the Akhiezer damping and the thermo-elastic dissipation (TED). Akhiezer damping results from the local disturbance of the equilibrium phonon distribution while TED takes place due to a spatial flow of heat energy. When the time period of mechanical oscillation becomes comparable to the phonon equilibration time, Akhiezer damping becomes important. The Akhiezer dynamics is, therefore, expected to play an important role in NEMS. The first goal of this research work is to study Akhiezer damping in nano-structures using NEMD. In-order to isolate Akhiezer dynamics we develop a simulation method to generate a nearly uniform strain field in the structure. A uniform strain field ensures that there is no spatial flow of energy and hence TED is suppressed. Using the simulation method, we performed size and frequency study of the Q factor. For the cases considered, we find that the surface can have a positive role in reducing dissipation due to Akhiezer dynamics.

With the understanding of Akhiezer damping in nano-structure, we, next, study the total dissipation in a beam under flexure deformation. For such a case the resulting strain field is non-uniform and TED also becomes operative. We use the free vibration method to study dissipation for the flexure mode. In this method, the mode of interest is excited by imparting excess energy to it. From the subsequent decay rate of the mode amplitude, the Q factor is determined. We performed a comparative study of the dissipation in the bending and the stretching mode of operation. Surprisingly, we observe that a spatial flow of heat energy results in lowering the damping rate in the bending mode of operation. We consider a reduced order model, based on the Boltzmann transport equation, to explain this observation. The results show that the thermo-mechanical coupling at the nano-scale shows behavior which are fundamentally different from a macroscopic sized object. The classical thermo-elasticity is not applicable at these time and length scales. We, also, investigate the role of tension the Q factor.

Using NEMD we, therefore, gain insights into the two principal intrinsic loss mechanisms, namely the Akhiezer and the TED. While a powerful tool, NEMD is still limited in terms of length and the time-scale that it can simulate. The next objective of this work is, thus, to develop multi-scale methods to model intrinsic dissipation under high frequency vibrations. The classical thermo-elasticity theory does not capture the essential physics that become important at these time and length scales. In this work, we extend the quasi-harmonic (QHM) frame-work to describe intrinsic dissipation in solids. Mechanical motion with time-scales comparable to the phonon relaxation rates are considered. A non-equilibrium stress component, that characterizes the local deviation from equilibrium, is considered. We obtain constitutive relations that govern the time evolution of the non-equilibrium stress. Using the proposed frame-work, we study dissipation as a

function of different parameters. The results are compared with those obtained using NEMD.

The QHM based multi-scale method describes the dynamics due to the local disturbance of the phonon population. Next, we consider the spatial flow of heat energy and use the Boltzmann transport Eqn. (BTE) to study dissipation. BTE under the gray approximation is considered. We show that two effects become important in the case of nano-structures. For the high frequencies of vibration, the finite relaxation time of the heat flux becomes important. We consider the case of longitudinal modes and modify the classical Zener[78] theory to account for this phenomenon. Secondly, and as for the Akhiezer dynamics, the surface scattering of the phonons reduces the relaxation time for a thermal disturbance. For the cases considered, we show that the faster thermalization has an effect of increasing the damping rate. Compared with the classical prediction, the resultant Q factor is high for all the cases considered.

We also investigate the damping mechanisms in low dimensional structures. NEMD and Langevin dynamics are employed for this purpose. We consider the case of graphene sheet and graphene nano-ribbons. Graphene is a single atomic layer thin sheet of carbon atoms and has been shown to have excellent mechanical[41] and electrical properties[54]. Graphene based structures offer potential applications as membrane[6] and string resonators. A few theoretical[31, 65] and experimental[8] studies have been performed to study dissipation in graphene. However, the different damping mechanisms remain unidentified. In this work we study intrinsic damping in graphene sheet and graphene nano-ribbons under in-plane stretching. We show that the geometric non-linear coupling between the in-plane vibration and out-of-plane motion plays a dominant role in the loss of mechanical energy.

Chapter 2

Akhiezer Damping

2.1 Introduction

Akhiezer damping takes place as a result of heat flow between different phonon modes. The applied strain field modulates the frequency of the thermal phonons. The strength of coupling between the strain field and the phonon modes varies and is given by a mode-dependent Gruneisen parameter, which is a measure of the change in frequency of each mode with applied strain. The applied deformation, therefore, results in a temperature difference between different phonon modes, and each of them then tends to relax toward the mean temperature value. This results in an intramode heat flow and, hence, entropy generation leading to dissipation. While TED depends on the applied strain field, Akhiezer damping rate is a more fundamental property of the system. Under the application of a uniform strain field, and in the absence of any additional mechanism of dissipation, the damping rate in a structure will be governed by the Akhiezer mechanism. Since the original work of Akhiezer[1] the absorption of acoustic waves by Akhiezer mechanism has been the subject of extensive research. Bommel and Dransfeld[4] developed an expression for attenuation of elastic waves by assuming that the dominant heat flow takes place between two phonon branches. Woodruff and Ehrenreich[76] derived an expression for damping of elastic waves by solving the Boltzmann transport equation. Mason and Bateman[48] introduced a nonlinearity parameter D for the attenuation coefficient due to Akhiezer damping and found good agreement with the experimental results for silicon and germanium. The theories developed in these works have been applied to a number of other experimental works[24, 39, 42] wherein it has been demonstrated that the Akhiezer mechanism becomes particularly important when the time scale of oscillation becomes comparable to the phonon relaxation time τ_{ph-ph}. A metric for assessing the strength of this mechanism is the $\omega\tau_{ph-ph}$ value. The mechanism plays an important role for the absorption of acoustic waves in the ultrasonic and the hypersonic regimes.

The angular frequency of oscillation of the fundamental longitudinal mode ω_l of a beam is given as

$$\omega_l = \sqrt{\frac{E}{\rho}}\frac{\pi}{2L}, \tag{2.1}$$

where ρ is the mass density and L is the length of the beam. For L of the order of few nanometers, frequency in the range of tens of GHz is obtained. The phonon relaxation time is generally of the order of few picoseconds. Thus, for beams with dimension in the range of nanometers, $\omega\tau_{ph-ph}$ will be of the order of 10^{-2}. The Q factor due to Akhiezer mechanism scales as[4]

$$Q^{-1} \propto \frac{\omega\tau_{ph-ph}}{1+(\omega\tau_{ph-ph})^2}. \tag{2.2}$$

Q attains a minimum value Q_{min} for $\omega\tau_{ph-ph} = 1$. For $\omega\tau_{ph-ph}$ of the order of 10^{-2}, $\frac{Q}{Q_{min}}$ is of the order of 10^2 and one expects the Akhiezer damping to be an important loss mechanism at such length scales. A number of experimental as well as theoretical works have been carried out to elucidate the dissipation mechanisms in a nanostructure. These works have provided insight into the different possible dynamics operating at the nanoscale. Kiselev et al.[32] solved the Boltzmann transport equation and studied the relative importance of TED and Akhiezer damping in a nanobeam under flexure. The analysis, however, did not take into consideration the variation in material properties with size. For example, the value of τ_{ph-ph} was assumed to be the same for all sizes. Further attempts to isolate and study the role of individual dissipation dynamics at such small length scales have not been made. A more general study of the role of surface on individual dissipation mechanism is therefore lacking and we attempt to make some effort in this direction. In this work[35], we employ classical molecular dynamics (MD) to understand Akhiezer dynamics in nanostructures. The other known dissipation mechanism, namely, TED, is eliminated by applying a nearly uniform strain field. It is worth pointing out that additional mechanisms, such as the surface dissipation, may also be present and mask the dynamics that would have resulted solely from Akhiezer damping. Attempts have not been made to isolate such effects. In Sec. 2.2, we review the dynamics of a beam under longitudinal vibration and present a case of a nearly linear displacement profile. In Sec. 2.3, we describe the MD setup to study the vibration of a nickel nanostructure, using the idea of Sec. 2.2 to attain the desired objective. In Sec. 2.4, the results are summarized, and conclusions are given in Sec. 2.5.

2.2 Beam Dynamics

Figure 2.1 shows a schematic of the structure considered. The structure is anchored using a rigid support at one end, a perodic force is applied at the other end. The equation of motion for the displacement profile, $u(x,t)$, of a purely elastic beam under longitudinal vibration is given as

$$E\frac{\partial^2 u(x,t)}{\partial x^2} = \rho\frac{\partial^2 u(x,t)}{\partial t^2} + f(x,t), \tag{2.3}$$

where E is the Young's Modulus, ρ is the mass density and $f(x,t)$ is the applied force. A concentrated periodic load $f(x,t) = F_0\delta(x-L)cos(\omega t)$ is applied at the end. F_0 is the magnitude of the applied load, ω is the angular frequency of the applied force and L is the length of the beam. The solution of Eqn.(2.3) for such case is obtained as $u(x,t) = A_m sin(\frac{\pi}{2L_0})cos(\omega t)$. A_m is the measure of the amplitude of oscillation and $L_0 = \frac{\pi}{2\omega}\sqrt{\frac{E}{\rho}}$. The physical interpretation of L_0 is that it corresponds to the length of an imaginary beam, which has the same material properties as stated above and for which the angular frequency of the fundamental longitudinal mode is equal to ω. Under the condition that L is sufficiently smaller than L_0, $u(x,t)$ can be approximated as

$$u(x,t) = A_m sin(\frac{\pi x}{2L_0})cos(\omega t) \approx A\frac{\pi x}{2L_0}cos(\omega t) \tag{2.4}$$

This results in a linear displacement profile with a uniform strain field. The amplitude of oscillation at the end of beam A is then given as $A = A_m\frac{\pi L}{2L_0}$. The elastic energy U stored in the beam is then given as

$$U = \int_0^L \frac{1}{2}SE(\frac{A_m}{2L_0})^2 dx, \tag{2.5}$$

where S is the cross-sectional area of the beam.

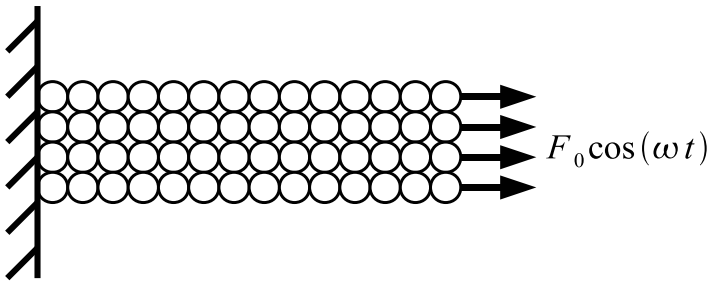

Figure 2.1: A schematic of the simulation set-up.

For a linear displacement profile, U is obtained as

$$U = \frac{1}{2}k(A)^2, \tag{2.6}$$

where k is effective stifnness of the beam and is given as $k = \frac{EA}{L}$

2.3 Simulation Set-up

A nickel structure was generated by arranging atoms on a face-centered cubic (fcc) lattice with a lattice spacing of 3.5374 $\mathring{A}$. A schematic of the simulation setup is illustrated in Fig 2.1. 20 unit cells, corresponding to a length of 7.07 nm, were taken in the longitudinal [100] direction, while the cross-section area was varied from 3.53 $\times$ 3.53 nm^2 to 7.07 $\times$ 7.07 nm^2 for different studies. All atoms within one unit cell from the left end were fixed by setting the forces on them to be zero. This corresponds to a clamped boundary condition. The embedded atom method (EAM) potential[14] was used to model the force field. Large-scale atomic/molecular massively parallel simulator (LAMMPS)[59] was used for all MD simulations. The structure was equilibrated at 300 K using a Nose-Hoover thermostat with a time constant of 1 ps. A time step of 1 fs was used for the entire simulation. After equilibration of the structure for 2 ns, a periodic force was applied to the atoms on the right longitudinal edge in the x direction. The system was further evolved as a canonical (NVT) ensemble for a simulation time of 30 ns.

For a perfectly elastic structure, the mean displacement of the end atoms would be in phase with the applied periodic force. However, because of dissipation, a phase lag exists between the applied force and the response. The work done by the applied force per unit period is a measure of the energy dissipation rate. In an isolated system (microcanonical ensemble), this work would result in an increase in the internal energy, and hence the temperature, of the system. For a system evolved as a canonical ensemble, the thermal bath takes away the excess energy and keeps the mean temperature constant. The energy dissipated per unit period E_{diss} is equal to the work done by the external force and is given as

$$E_{diss} = \frac{\omega}{2\pi T_f} \int_0^T \sum_{n_e} f_0 cos(\omega t) v_x dt, \tag{2.7}$$

where f_0 is the magnitude of the applied force on each of the end atom, v_x is the x component of the velocity, T_f is the total time for which the force is applied and n_e is the number of atoms at the end on which the external force is applied. F_0 is related to f_0 as $F_0 = n_e f_0$. We neglected an initial transient of 2 ns from the time the external force was imposed for computing the energy dissipation rate. In order to compute the energy stored, the Fourier transform of the x component of the center-of-mass displacement of the edge atoms was taken. The Fourier transform showed a dominant peak corresponding to the frequency of the applied force. The amplitude of oscillation was computed from the peak magnitude as

$$A = max(2abs(fft(xdata)))/(ndata), \tag{2.8}$$

where $xdata$ is the time series data of the center of mass of end atoms and $ndata$ is the number of data

points.

The effective stiffness of the structure was determined using a separate equilibirum simulation. After an initial equilibration at 300 K for 2 ns, a static force was applied on the end atoms. The structure was relaxed for 1 ns, the length value corresponding to the applied force was then computed using the data obtained for a subsequent time of 1.5 ns. The force magnitude was then increased and the procedure described above was followed to compute the new relaxed length for the increased applied force value.This was repeated with subsequent force increments and the length value was obtained for different magnitude of the applied force. The slope of the force displacement curve gives the value of k.

The energy stored E_{stored} was, then, computed as

$$E_{stored} = \frac{1}{2}kA^2. \tag{2.9}$$

The Q factor is then given as

$$Q = \frac{2\pi E_{stored}}{E_{diss}}. \tag{2.10}$$

2.4 Results and Discussion

We first studied the frequency dependence of Q factor for the bulk case. The bulk case was simulated by imposing the periodic boundary condition in the lateral direction. A size independence for a simulation domain with cross-sectional area larger than 3.53 $\times$ 3.53 nm^2 was observed. Figure 2.2(a) shows the plot of the Q factor versus frequency as obtained for the bulk case. The Q factor decreases and, hence, the dissipation rate increases with the increase in frequency.

Under the single mode relaxation time approximation, the Q factor for Akhiezer damping is given as [4]

$$Q^{-1} = \frac{C_p T \lambda_{av}^2}{\rho v^2} \frac{\omega\tau_{ph-ph}}{1 + (\omega\tau_{ph-ph})^2}, \tag{2.11}$$

where ρ is the density, v is the sound velocity, C_p is the specific heat capacity at constant pressure, T is temperature, λ_{av} is mean value of Gruneisen parameter, ω is the angular frequency of the applied strain field and τ_{ph-ph} is a measure of a phonon energy mean transfer time. Eqn.(2.11) states that, for $\omega\tau_{ph-ph} \leq 1$, Q factor decreases with the increase in frequency. The phonon relaxation time is of the order of a few picoseconds for which the above inequality is valid in the frequency range of the order of a few GHz. Eqn(2.11) can be further recasted as

$$Q\omega = m\omega^2 + c, \tag{2.12}$$

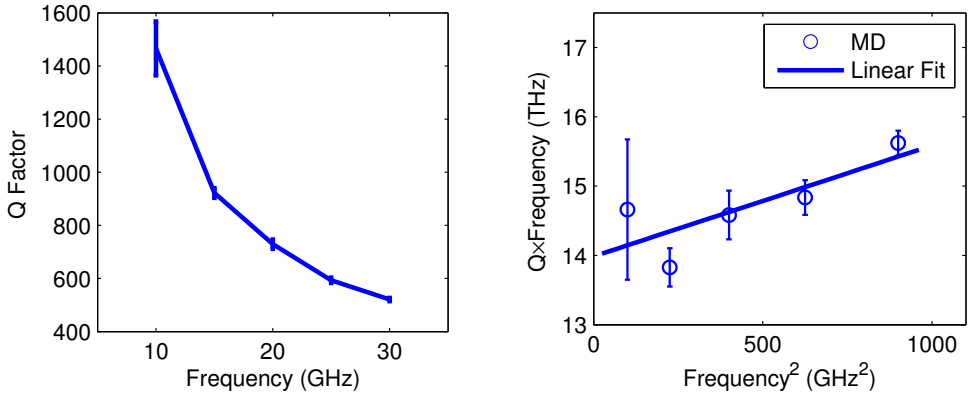

(a) (b)

Figure 2.2: a) Q Factor vs. Frequency for bulk nickel. b) A linear fit for $Q\omega$ vs. ω^2 for the same structure.

where $m = \dfrac{\rho\tau_{ph-ph}v^3}{C_pT{\lambda_{Av}}^2}$ and $c = \dfrac{m}{\tau^2}$. Eqn(2.12) states that $Q\omega$ and ω^2 have a linear relationship. Figure 2.2(b) shows the plot of $Q\omega$ vs ω^2 as obtained for the bulk case and a linear dependence between $Q\omega$ and ω^2 is observed. The slope and the intercept of the linear fit was used to compute the τ_{ph-ph} value which was estimated to be 1.72 ps.

Different studies have estimated different values of τ_{ph-ph}. According to Bomme et al.[4], the value of τ_{ph-ph} should be taken to be same as that of the thermal relaxation time, τ_{th}, given as

$$\tau_{th} = \frac{3\kappa}{C_v v^2}. \tag{2.13}$$

Here, κ is the thermal conductivity and C_v is the specific heat capacity at constant volume. Mason and Betman[48] used a value of $\tau_{ph-ph} = 2\tau_{th}$ for the longitudinal mode and obtained a very good agreement with the experimental data. Heino and Ristolainen[25] computed the phonon mean-free path l for nickel using MD, although they used a different version of the EAM potential to model the force field. Making use of $\tau_{th} = \dfrac{l}{v}$ and using the data given by Heino and Ristolainen[25], the value of τ_{th} comes out to be 0.96 ps. The ratio $\dfrac{\tau_{ph-ph}}{\tau_{th}} = 1.8$, it then follows that the relation given by Mason and Bateman[48] holds more applicable for our case.

Phonon relaxation time can be computed by taking the correlation of the mode potential or kinetic energy [50]. $20 \times 10 \times 10$ unit cells of nickel with periodic boundary condition in all directions were used. The relaxation time for phonons in the direction of 20 unit cells, which corresponded to [100] direction in a fcc lattice structure, were computed at 300 K. The correlation function of the mode kinetic energy was

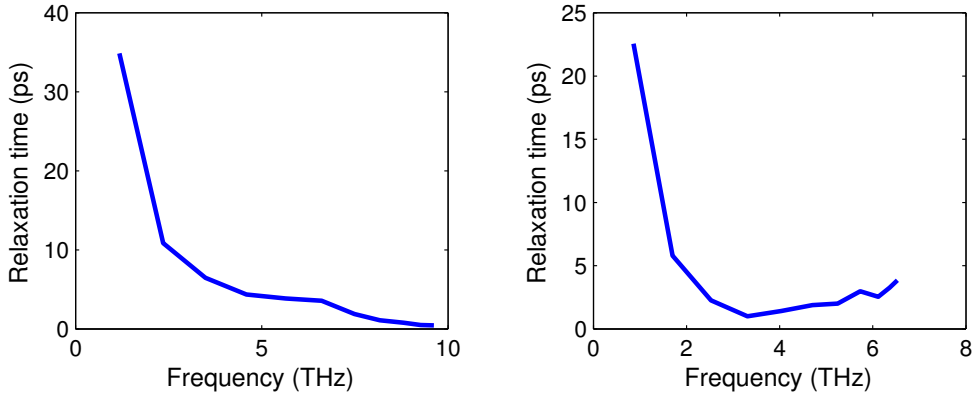

(a) (b)

Figure 2.3: Phonon relaxation time as a function of mode frequency.a) Longitudinal modes b) Transverse modes.

taken to estimate the decay rate. A phonon is a propagating wave for which the mode shape is given as

$$\vec{u}_p(\vec{x},t) = \vec{P}exp(i\vec{k}.\vec{x})exp(i\omega_0 t), \tag{2.14}$$

where $\vec{x}$ is the position vector of each atom, $\vec{u}_p$ is the displacement of an atom from the mean position, $\vec{k}$ is the wave vector, ω_0 is the phonon frequency and $\vec{P}$ is the polarization vector. $\vec{k}$ is given by the boundary condition. For a given value of $\vec{k}$, one can construct a force constant matrix[72] using second-order derivative of the potential function; the eigenvectors of the force constant matrix then give $\vec{P}$ and the eigenvalues scaled with atomic mass give ω_0^2. $\vec{k}$ and $\vec{P}$ completely characterize a mode shape. MD displacement and velocity are then projected on the mode shape to get the mode displacement d_m and the mode velocity v_m. The mode kinetic energy Ke_m is then computed as $Ke_m = \frac{1}{2}mv_m^2$. The correlation function of Ke_m was taken to estimate the decay rate. Figure 2.3 shows the relaxation time for the transverse and longitudinal phonons as obtained for the bulk case. The phonon density of state (PDOS) was computed by taking the fast Fourier transform (FFT) of the function $C(t)$ given as

$$C(t) = \frac{1}{n_{atoms}} \left\langle \sum_{n_{atoms}} \vec{v}_i(t_0).\vec{v}_i(t_0+t) \right\rangle, \tag{2.15}$$

where n_{atoms} is the total number of atoms and $\vec{v}_i(t)$ are the velocity components. Figure 2.4 shows the PDOS obtained. The PDOS has two peaks, the peak at 6 THz corresponds to the transverse mode while the peak at 9 THz corresponds to the longitudinal mode. At 5.73 GHz the transverse mode has a relaxation time of 2.97 ps and at 8.8 GHz the longitudinal mode has a relaxation time of 0.78 ps, the mean of these

two values comes to be 1.875 ps which is comparable to the phonon relaxation time estimated from Q vs ω scaling.

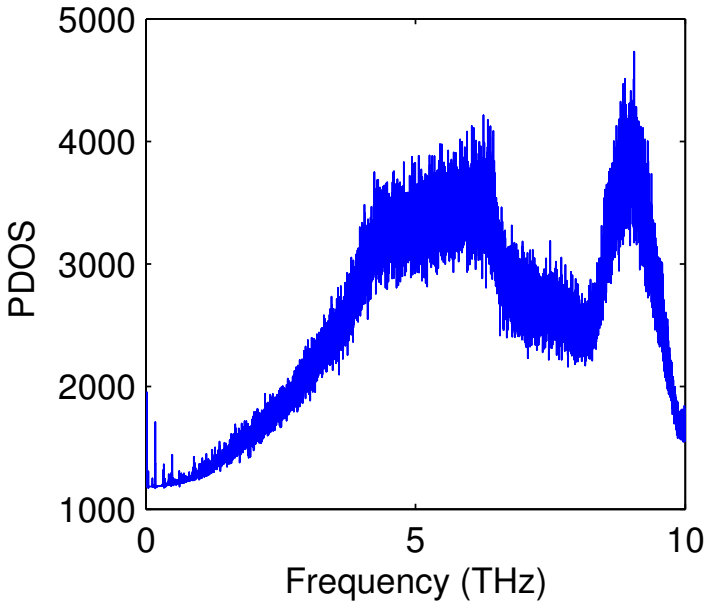

Figure 2.4: Phonon density of state for bulk Nickel.

The scaling of Q factor with ω was then studied for the finite sized case. A free surface boundary condition was imposed in the lateral direction. We considered three different cases, each of them having a length of 7.1 nm in the longitudinal direction, and with cross-sectional areas as 3.53×3.53 nm^2, 5.29×5.29 nm^2 and 7.07×7.07 nm^2. Figure 2.5(a-c) shows the plot of Q vs frequency for the three cases. For all the sizes the dissipation rate was found to increase with the increase in frequency. The plot also shows a $Q = A(\omega)^{-1}$ curve, with A obtained using the least square fit from the data points. For the case of cross-section area of 7.1×7.1 nm^2, the Q value closely follows the $A\omega^{-1}$ curve. For the smallest size, the MD data and the inverse relationship became slightly deviant.

The Q vs ω relation, as stated in Eqn 2.11, was derived by Bommel et al. [4] under the assumption that λ for a given phonon branch is independent of frequency and two phonon groups are present. This is applicable for a bulk structure for which only the longitudinal and transverse modes are present. In a low dimensional structure, such as a nanowire, the presence of a surface splits the phonon spectrum into sub-band[26, 69]. The assumptions used in deriving Eqn 2.11 are, therefore, not applicable for nanostructures.

Under the approximation $\omega\tau_{ph-ph} \leq 1$, Woodruf and Enrich [76] derived an expression for damping of elastic waves by solving the Boltzmann transport equation. An expression for the attenuation coefficient, α,

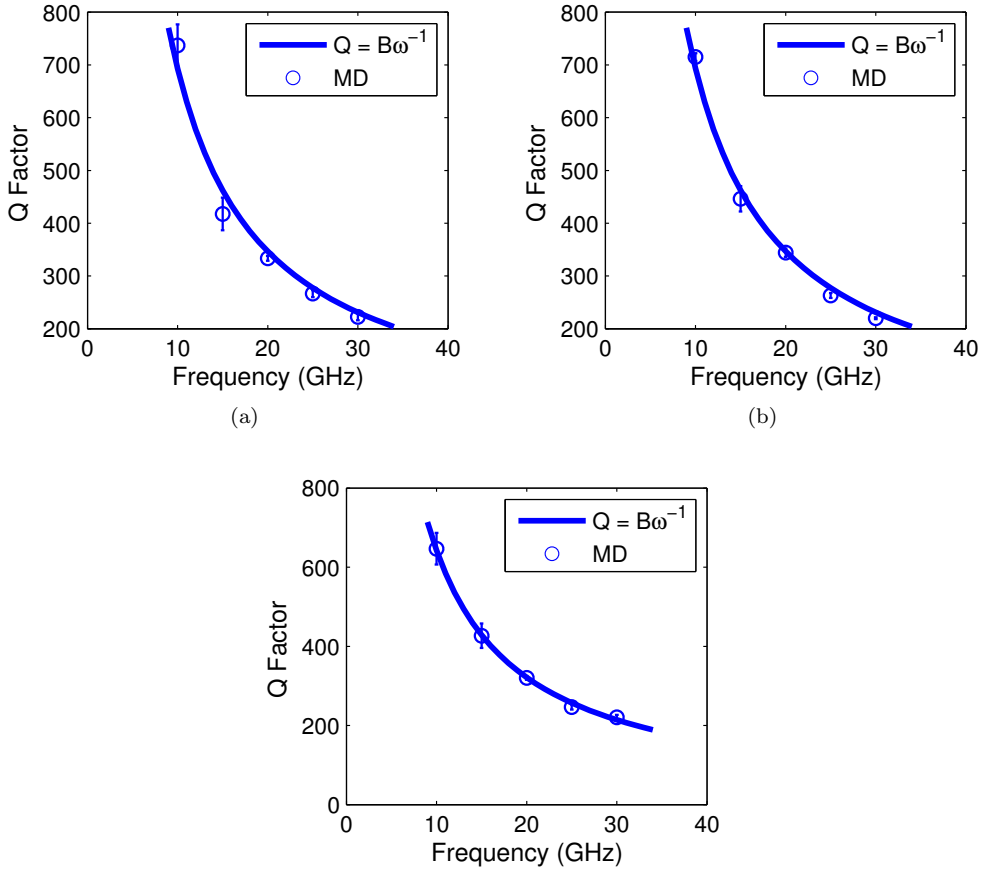

Figure 2.5: a) Q Factor vs. Frequency for nickel nano-structure with free surfaces.

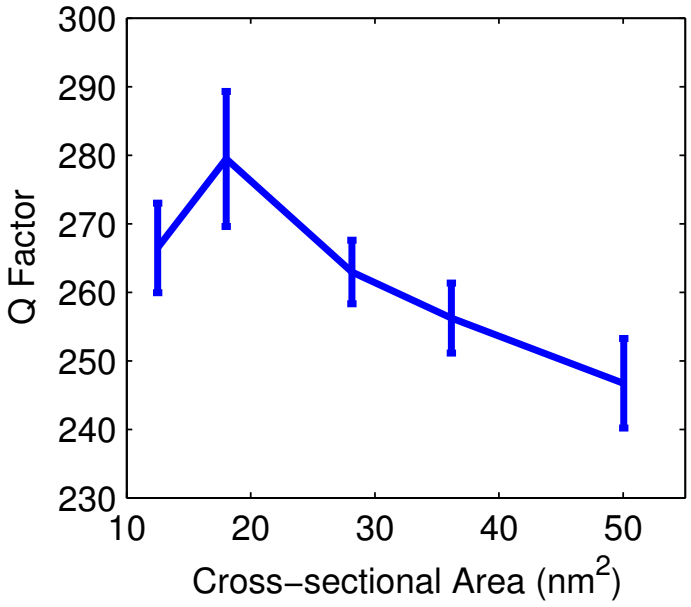

Figure 2.6: Q factor as a function of size.

was obtained as

$$\alpha = \beta \frac{\omega^2 T}{\rho {v_o}^2} \sum_{q,j} \tau(q,j) \lambda^2(q,j) C(q,j), \tag{2.16}$$

where β is a numerical coefficient, v is the sound velocity, $\tau(q,j)$, $\lambda(q,j)$ and $C(q,j)$ are the relaxation time, the Gruneisen parameter and specific heat capacity of the phonon branch labelled as q,j. Q is related to α as $Q = \frac{\omega}{2\alpha}$ and hence Eqn(2.16) shows that Q scales as ω^{-1}. This explains the trend as has been observed for the case of $7.1 \times 7.1\text{nm}^2$ cross-section area. The deviation in case of smaller sizes needs to explored further.

We studied the size dependence of Q factor for finite sized case for a fixed frequency of 25 GHz, The cross-section area was varied from 12.51 nm^2 to 50.41 nm^2. Figure 2.6 shows that the Q factor first shows an improvement with the decrease in size and then drops below some critical size. This trend in the variation of Q factor with size indicates the role of different competing factors.

The initial decrease in the dissipation rate with the decrease in size can be explained by the role of surface on the ensemble of thermal phonons. Akhiezer damping takes place as a result of the modulation of thermal phonons with the applied strain field. The strain field disturbs the equilibrium of the thermal phonons which then relax towards equilibrium with a finite relaxation time. Faster relaxation of phonons towards thermal equilibrium would decrease the lag between the stress and the strain and would result in a lower dissipation rate. A manifestation of this effect was observed by Harding and Wilks[23] who found that that the attenuation of sound in liquid helium decreased by the addition of small amount of ^{3}He impurity.

The presence of surfaces act as an additional scattering mechanism[68] and reduces the relaxation time of thermal phonons in nano-structures. Such an effect has been studied before and has been accounted for as a reason for the decrease in thermal conductivity of nano-wires [82].

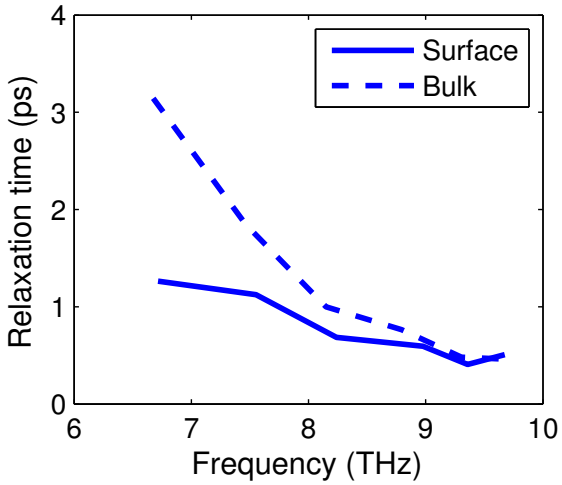

Figure 2.7: Relaxation time for longitudinal phonons in nickel nanowire and its comparison with bulk value.

The phonon relaxation time for a finite sized case was computed using the method described by McGauhney and Kaviany[50]. A nickel structure with $20 \times 12 \times 12$ unit cells was used. Periodic boundary condition was imposed in the direction of 20 unit cells while free surface boundary condition was used otherwise. Computing the phonon relaxation time in this case would entail using the eigen modes for the one-dimensional structure. The bulk mode shape was used instead. For large wave vectors the bulk modes corresponded to the eigen modes of the structure considered, this was evident from the correlation function of the mode potential or kinetic energy which showed a dominant single frequency. The relaxation time was computed only for large wave vectors for which the eigen modes are sufficiently given by the bulk mode shapes. Figure 2.7 shows the plot of relaxation time for longitudinal phonons obtained from the finite-sized case. The bulk values are also plotted for comparison. For the higher frequency values, both the finite structure and bulk have similar relaxation time. In this case, the relaxation is dominated by the Umklapp process. The relaxation time deviates with the decrease in frequency, with the finite-sized case having a lower value. The presence of surfaces therefore reduces the mean phonon relaxation time and hence the dissipation rate initially decreases with the decrease in size.

The autocorrelation function $S(t)$ of the heat current vector $q(t)$ can be used to estimate phonon mean relaxation times[51]. For a fcc crystal, $S(t)$ shows a two-stage decay. A biexponential fit of $S(t)$ gives two relaxation times[49]. The relaxation time with the smaller value is the mean lifetime of short-wavelength

phonons τ_{sp}. Physically, τ_{sp} corresponds to the time an atom takes to transfer energy to its neighboring atoms. The second relaxation time obtained from the biexponential fit is the long wavelength phonons mean lifetime τ_{lp}.

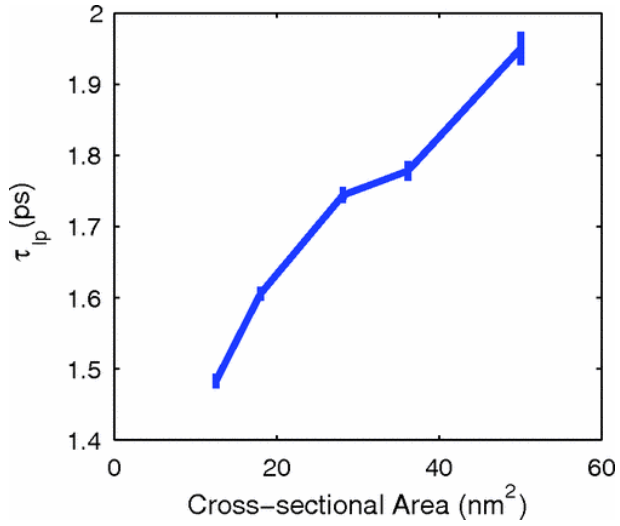

Figure 2.8: Variation of the long-wavelength phonons mean relaxation time τ_{lp} with size..

τ_{sp} and τ_{lp} values were estimated for nickel nanowires of varying cross-sectional area. The periodic boundary condition was used in the longitudinal direction, while the free surface boundary condition was used otherwise. $S(t)$ was computed by taking the autocorrelaton of the component of $q(t)$ in the longitudinal direction. A total simulation time of 6 ns was used to compute $S(t)$. The biexponential fitting was done on the values of $S(t)$ for a period of 5 ps. τ_{sp} was estimated to be of the order of a few femtoseconds. For the frequency range under consideration, this time scale is not of importance and hence was not considered for analysis. Figure 2.8 shows the τ_{lp} values for different cross-sectional areas. The plot shows that τ_{lp} decreases with the decrease in size. This decrease in τ_{lp} value with the decrease in size is expected to govern the Q factor variation for larger sizes. For the Akhiezer mechanism, dissipation rate and relaxation time have a direct relationship and, hence, the dissipation rate initially decreases with the decrease in size.

The surface atoms, because of lower coordination number, have intrinsic properties that are different from the bulk atoms. The increasing role of surface atoms, with the increase in surface to volume ratio, results in change in the properties of a nanostructure. The length scale at which such an effect becomes important is of the order of a few nanometers. The magnitude of this length scale depends on the material property of interest and the nature of the material itself. For example, the Youngs modulus of a silicon nanowire drops sharply below a cross-section area of 10 nm^2[72].

The physical origin of the Akhiezer damping mechanism lies in the flow of heat current between different

phonon modes. The flow of heat takes place due to the difference in $\lambda(q,j)$ values between different modes, with $\lambda(q,j)$ being a measure of the change in temperature of each mode when strained adiabatically. The higher the difference in the $\lambda(q,j)$ value for different modes, the higher will be the temperature difference. This effect on the dissipation rate is quantified by a nonlinearity parameter[76] D given as

$$D = 3\left[\frac{3\sum_{q,j}[\lambda^2(q,j)]}{n} - \frac{\lambda^2 C_v T}{E_0}\right] \tag{2.17}$$

where n is the number of the modes, E_0 is the total thermal energy, and λ is the volume Gruneisen constant. The attenuation due to the Akhiezer mechanism is related to D as $\alpha_t = \frac{D\omega^2 E_0 \tau_{ph-ph}}{6\rho v^3}$.

D by definition is therefore a metric of the variance in the $\lambda(q,j)$ value. In a bulk crystal, the main contribution to D comes from the difference in the $\lambda(q,j)$ value between the transverse and the longitudinal branches. The presence of surface leads to additional modes in a nanostructure. Some of these modes, called the surface modes, have displacement profiles in which the surface atoms share most of the amplitude. $\lambda(q,j)$ for such modes will therefore depend on the property of the surface atoms and will be different from that of the bulk-like modes. The presence of such modes will therefore contribute to an increase in the value of D and, hence, an increase in the dissipation rate. The fraction of such modes to the total number of modes depends on the ratio of the number of surface atoms to that of the bulk atoms and is expected to become significant only at very small dimension.

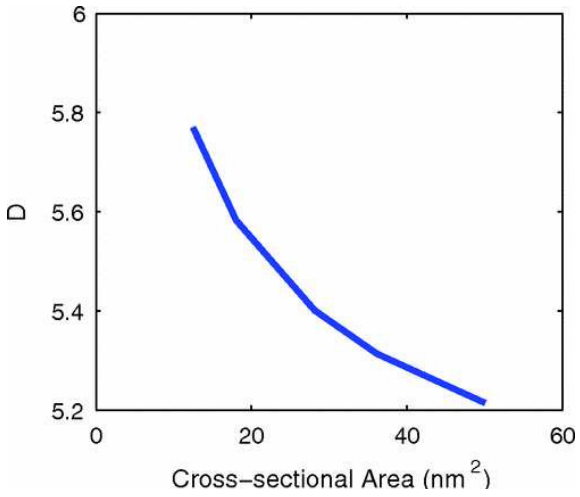

Figure 2.9: Variation of the nonlinearity parameter D with size as computed using the LQHM model..

The local quasiharmonic (LQHM) model[73] was used to estimate the D value for nickel nanobeams. In the LQHM model, the motion of each atom is decoupled from the rest. A local stiffness matrix $\Phi(\alpha)$ is obtained by taking the double derivative of the potential energy with respect to displacement vector of an

atom α. From the eigenvalues of $\Phi(\alpha)$, three vibrational frequencies $\omega_{\alpha i}(i = 1, 2, 3)$ are determined. The local Gruneisen parameter $\lambda_{\alpha i}$ is given as $\lambda_{\alpha i} = -\frac{V}{\omega_{\alpha i}} \frac{d\omega_{\alpha i}}{dV}$, where V is the volume of the crystal. We define $C_{\alpha i}$ as

$$C_{\alpha i} = \frac{k_b (\frac{\hbar \omega_{\alpha i}}{k_b T})^2 exp(\frac{\hbar \omega_{\alpha i}}{k_b T})}{[exp(\frac{\hbar \omega_{\alpha i}}{k_b T}) - 1]^2} \tag{2.18}$$

and $E_{\alpha i}$ as

$$E_{\alpha i} = \frac{\hbar \omega_{\alpha i}}{exp(\frac{\hbar \omega_{\alpha i}}{k_b T}) - 1}. \tag{2.19}$$

Here, k_b is the Boltzmann constant, $\hbar = \frac{h}{2\pi}$ and h is the Plancks constant. In the LQHM model, λ is obtained as

$$\lambda = \frac{\sum_{\alpha=1}^{nt} \sum_{i=1}^{3} C_{\alpha i} \lambda_{\alpha i}}{\sum_{\alpha=1}^{nt} \sum_{i=1}^{3} C_{\alpha i}}. \tag{2.20}$$

Here, nt is the total number of atoms in the structure, C_v and E_0 in the LQHM model are given as $C_v = \frac{1}{V} \sum_{\alpha=1}^{nt} \sum_{i=1}^{3} C_{\alpha i}$ and $E_0 = \frac{1}{V} \sum_{\alpha=1}^{nt} \sum_{i=1}^{3} E_{\alpha i}$.

Finite-sized nickel nanostructrues, as used in the MD simulations, were considered for LQHM analysis. $\lambda_{\alpha i}$ values were computed by imposing a uniaxial deformation on the structure. The values of $\lambda_{\alpha i}$, λ, C_v, and E_0 thus obtained using the LQHM model were substituted in Eq.(2.17) to get the value of D. Figure 2.9 shows the value of D for nickel nanobeams of different cross-sectional area. The plot shows that D increases with the decrease in size. For the smallest size considered, the increase in the value of D is expected to become significant and compensate for the decrease in the relaxation-time value. This effect of surface on the D value plausibly explains the observed nonmononotic scaling of the Q factor with size.

2.5 Conclusions

MD simulations have been used to investigate the dissipation in a nickel nanowire. A nearly uniform strain field was applied to eliminate TED. In such a case, we expect the dissipation to be dominated by the Akhiezer mechanism. From the scaling of the Q factor with ω for the bulk case, τ_{ph-ph} was estimated. The value was comparable with the estimate obtained from other methods. The finite-sized case showed an inverse scaling of Q factor with ω, and for the smallest size considered, a slight deviation was observed. The size dependence of the Q factor showed a positive role of the surface wherein the Q factor initially increased with the decrease in thickness. This was explained by the role of the surface as a scattering medium for the thermal phonons. For dimensions below some critical value, a drop in Q factor with size was observed, and this was attributed to the contribution of surface atoms to increase the variance in the D value.

Chapter 3

Dissipation - Flexure Mode

3.1 Methods

We use MD simulations to compute dissipation rate in nano-wires[38]. We consider two different modes of deformation, the bending and the stretching mode. The bending mode was excited using free vibration method. For stretching deformation we use the method of forced vibration. Since, dissipation rate strongly depends on the frequency of mechanical motion, a study on the effect of deformation mode on energy loss requires that both the modes have the same oscillation time period. Using the method of forced vibration, we could consider the same frequency of operation for stretching deformation as that for bending. Also, as discussed later, forced vibration results in a nearly uniform strain field, an essential characteristic for stretching motion. In the rest of the paper, we shall term free vibration method as method A and forced vibration as method B. We now provide a description of the two methodologies.

Different variants of method A have been used earlier [17, 30, 31] in the computation of Q factor. In this method, we perturb the desired mode of the structure. The perturbation can be provided by either increasing the mode velocity or by displacing the structure along the given mode. The structure is isolated from the environment (in-order to study intrinsic dissipation) and is left to evolve. The excess energy of the excited mode gets absorbed by the system and is converted into the internal energy. The modal amplitude, therefore, shows a sinusoidal decaying behavior. The modal frequency, f_m, and its relaxation time, τ_m, are determined from the sinusoidal decaying amplitude. Q factor is, then, computed as

$$Q = \pi f_m \tau_m. \tag{3.1}$$

We now provide the details of implementing method A for the fundamental bending mode of a fixed-fixed beam.

The structure is first equilibrated using the canonical ensemble (NVT). Nosé-Hoover thermostat was used for equilibrating the structure at desired temperature. A relaxation time of 0.5 ps was used for the thermostat. Subsequent to equilibration, a point is selected from phase space. The set of position and

velocity vector of all the atoms constitutes a point in the phase space. Alternatively, the phase space can also be described using the modal co-ordinates. The modal co-ordinates can be obtained from the atomic co-ordinates by projecting them on to the mode shapes. The relation between the two is described in the subsequent paragraph. Since the phase space point is selected from an equilibrated ensemble, the different modes satisfy equipartition principle. We disturb the equilibrium of the system by adding excess energy to one of the modes of interest, in our case this is the fundamental bending mode. We use the method of giving an initial velocity disturbance.

In-order to perturb the velocity of a given mode we need to know the corresponding modal vector. A modal vector describes the correlated motion between different degrees of freedom of a system. Let $\vec{m}_i$ denote the relative displacement of an atom i with respect to its mean position for the mode under consideration. The set of $\vec{m}_i$ for all the atoms forms the modal vector. Let $\vec{v}_i$ be the velocity of the ith atom in the phase space point that is selected from canonical ensemble. The modal velocity, v_m, for the given configuration is then obtained as

$$v_m = \frac{\sum_{i=1}^{natoms} \vec{v}_i.\vec{m}_i}{\sum_{i=1}^{natoms} \vec{m}_i.\vec{m}_i} \tag{3.2}$$

Here, *natoms* is the total number of atoms. We wish to perturb the mode velocity by an amount Δv_m. This can be done by changing the velocity vector of the ith atom by an amount $\Delta\vec{v}_i$ such that $\Delta\vec{v}_i = \frac{\Delta v_m \vec{m}_i}{\sum_{i=1}^{natoms} \vec{m}_i.\vec{m}_i}$.

The atomic velocities are, thus, changed to $\vec{v}_i + \Delta\vec{v}_i$ while keeping the space co-ordinates fixed. Subsequently, the structure is evolved as a micro-canonical (NVE) ensemble. Micro-canonical ensemble ensures that the total energy of the system, E, remains conserved. As the system evolves, the phase space point spreads itself on the constant energy sphere. In the process, excess energy of the excited mode is uniformly shared with the rest of the modes. This can be seen by either monitoring the modal amplitude, a_m, or its velocity, v_m.

We excited the fundamental bending mode of a fixed-fixed nano-beam using method A. Figure 3.1(a) shows a schematic of the simulation step-up. The bending mode in the y direction was excited and we term it as mode 1. Mode shape for mode 1 was obtained using continuum theory. Using beam theory for a fixed-fixed beam we get

$$\vec{m}_i = \vec{e}_2\big(cos(\beta x_i^m) - cosh(\beta x_i^m) - 0.9825(sin(\beta x_i^m) - sinh(\beta x_i^m))\big). \tag{3.3}$$

$\vec{m}_i$ denotes the modal displacement for atom i, x_i^m is the mean x co-ordinate, $\vec{e}_2$ is a unit vector in the y direction and β is a constant. For a beam of length L_0, $\beta = \frac{4.730}{L_0}$. The velocity increment was provided

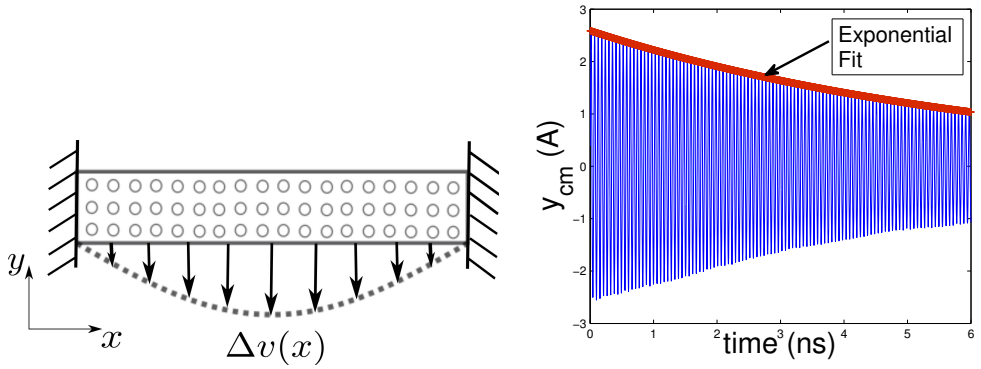

(a) (b)

Figure 3.1: a) A schematic of simulation set-up for computing the dissipation rate using method A. b) Time evolution of y_{cm} subsequent to mode 1 excitation.

such that the center of the beam had an initial maximum displacement of around 2.5 $\mathring{A}$. This corresponds to giving the center atoms a velocity increment Δv_c such that $\Delta v_c = 2.5\omega_f$. Here, ω_f is the angular frequency of mode 1. For providing the velocity increment an initial estimate of ω_f was made using beam theory. The velocity increment for the rest of the atoms was scaled in accordance with the mode shape given in Eqn.(3.3). The co-ordinates (either displacement or velocity) of mode 1 can be obtained in accordance with Eqn.(3.2) using $\vec{m}_i$ from Eqn.(3.3). Alternatively, one can also monitor y_{cm}, the y co-ordinate of the center-of-mass of the system. For a system with the rest of modes in equilibrium and with mode 1 exited, y_{cm} is a measure of mode 1 displacement (see appendix A.1 for more details). Figure 3.1(b) shows the time evolution of y_{cm} with mode 1 excited. A sinusoidal decaying behavior is observed. From the fit of data, f_m and τ_m were determined. Q factor was computed using the relation provided before.

For stretching deformation method B was used. Figure 3.2(a) shows a schematic of the simulation set-up for this method. In this method, the structure is isolated from the environment and subjected to a periodic deformation. For a dissipative system, periodic forcing of the system results in an increase in the internal energy. Thus, from the rate of increase of internal energy the dissipation rate, E_{disp}, can be computed. Let E_{stored} be the maximum elastic energy stored in the structure. Q factor, using method B, is determined as $Q = 2\pi \dfrac{E_{stored}}{E_{disp}}$. The details of implementing this method, for the case of stretching deformation, is now described .

The structure was first equilibrated at desired temperature using Nosé-Hoover thermostat. Subsequent to equilibration, the length of the structure was deformed periodically with an amplitude A and with an angular frequency ω_f. The structure was decoupled from thermostat during periodic forcing. Forcing the structure, at any finite rate, results in disturbance of thermal equilibrium. Since the system is driven out-

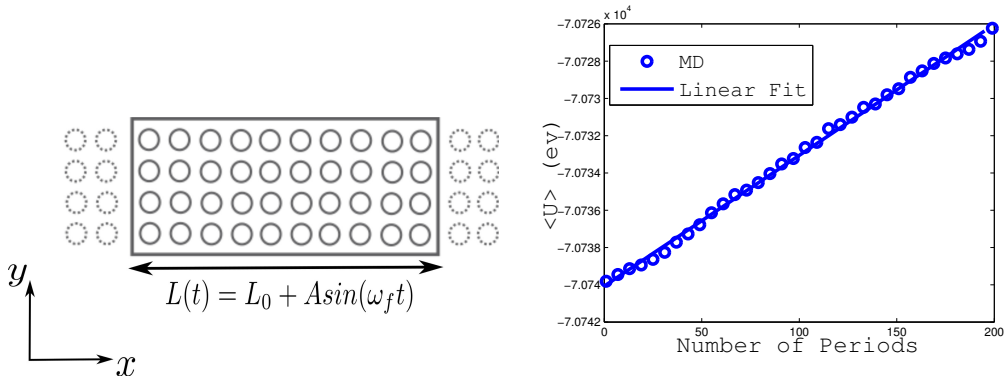

(a) (b)

Figure 3.2: a) A schematic of the simulation set-up for computing the dissipation rate using method B. The length of the structure in x direction is changed periodically with an amplitude A and angular frequency ω_f. The structure has periodic boundary condition in x direction, the dotted circles show the image atoms. b) Increase in internal energy of structure with number of oscillation periods.

of-equilibrium, energy will be dissipated and work done during one complete cycle (one period of sinusoidal motion) will be non-zero. The second law of thermodynamics states that the entropy of an isolated system never decreases. From the law it can be inferred that for a thermally isolated system, that exchanges work with the environment, no net work can be extracted during a cyclic loading. Further, for finite rate deformations (under which the system moves out of equilibrium) the average work done on the system will be positive. The average work done during a cyclic loading process is a measure of dissipation rate. Since the system is decoupled from thermostat during loading, the work done will result in an increase in its internal energy. Let ΔU be the increase in internal energy of system after n oscillation periods and W be the total work done. From the first law of thermodynamics, it follows that $W = \Delta U$. From the rate of increase of mean energy, $< U >$, per unit period, the energy dissipated, E_{disp}, can be determined. Figure 3.2(b) shows the plot of $< U >$ with the number of oscillations for one of the ensembles under forced excitation. $< U >$ increases nearly linearly, the slope of the curve gives E_{disp}.

Method B was used to excite the stretching mode and to generate a spatially homogenous strain field. It would be useful to deduce under what condition the resulting strain profile is nearly uniform. The equation for longitudinal motion (in the forced direction) with no body force is given as

$$E_{stretch}\frac{\partial^2 u(x,t)}{\partial x^2} = \rho\frac{\partial^2 u(x,t)}{\partial t^2} \tag{3.4}$$

Here, $E_{stretch}$ is the Young's modulus for stretching deformation, ρ is the density and $u(x,t)$ is the x displacement field. For the boundary conditions, we have $u(0,t) = 0$ and $u(L_0,t) = Asin(\omega_f t)$. L_0 is the

length of the structure considered. The steady state displacement profile with these boundary conditions is obtained as $u(x,t) = A\frac{sin(\omega_f\sqrt{\frac{E_{stretch}}{\rho}}x)}{sin(\omega_f\sqrt{\frac{E_{stretch}}{\rho}}L_0)}sin(\omega_f t)$. Further, under the condition that $\omega_f\sqrt{\frac{E_{stretch}}{\rho}}L_0 <= 1$, we have $u(x,t) \approx A\frac{x}{L_0}sin(\omega_f t)$. For a given value of ω_f, L_0 can be chosen such that a linear displacement profile (and hence uniform strain field) is obtained. For stretching motion, ω_f was taken to be the same as that of mode 1 for a nano-wire with same cross-sectional area. The value of L_0 was, then, considered such that a nearly linear displacement profile is obtained.

For stretching deformation, the maximum elastic energy stored, E_{stored}, is obtained as $E_{stored} = \frac{1}{2}VE_{stretch}\epsilon_0^2$. Here, V is the volume of structure and ϵ_0 is the strain amplitude. ϵ_0 is related to displacement amplitude as $\epsilon_0 = \frac{A}{L_0}$. For our simulations we considered the value of $\epsilon_0 = 0.002$. Q factor, using method B, is then obtained as $Q = \frac{2\pi E_{stored}}{E_{disp}}$. For our studies, we considered two different materials, nickel and copper. Embedded atomic method (EAM) potential [14] was used to model the force field for each of these materials. Q factor was computed for bending (method A) and stretching (method B) deformation for structures with different sizes. All MD simulations were performed using large-scale atomic/molecular massively parallel simulator [59].

3.2 Results and Discussion

3.2.1 Size Study

Q factor was computed using method A for structures with a fixed length of $100\,lc$. lc is the lattice constant, and has value of 3.5374 $\mathring{A}$ for nickel and a value of 3.615$\mathring{A}$ for copper. The cross-sectional area was varied from $10\,lc \times 10\,lc$ to $18\,lc \times 18\,lc$. Figures 3.3(a) and 3.3(b) show the plot of Q factor versus size (width) obtained under bending deformation for nickel and copper, respectively. The plot shows that the Q factor increases with the decrease in cross-sectional area for both the materials .

We next computed the Q factor using method B for stretching deformation. The length of the structure was taken to be $12lc$. The choice of this length resulted in a nearly uniform strain field. The cross-sectional area was, again, varied from $10\,lc \times 10\,lc$ to $18\,lc \times 18\,lc$. For a given cross-section area, the excitation frequency was taken to be the same as that for bending deformation in the previous case.

Figures 3.3(a) and 3.3(b) also show Q factor versus size, as obtained, using method B. Q factor increases with the decrease in size. Further, with the decrease in size the difference in Q factor between the two deformation modes increases. The structure, therefore, has lower dissipation in bending in comparison with stretching motion for smaller sizes.

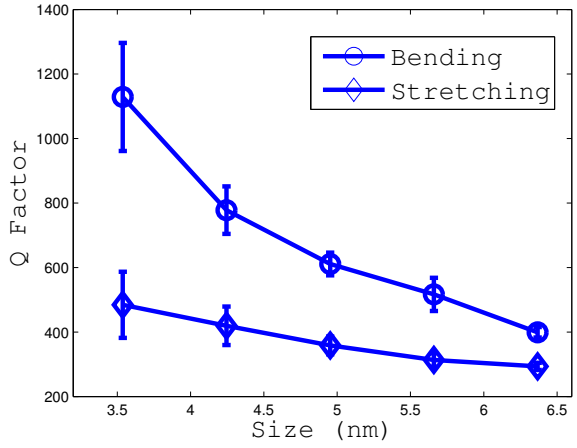

(a)

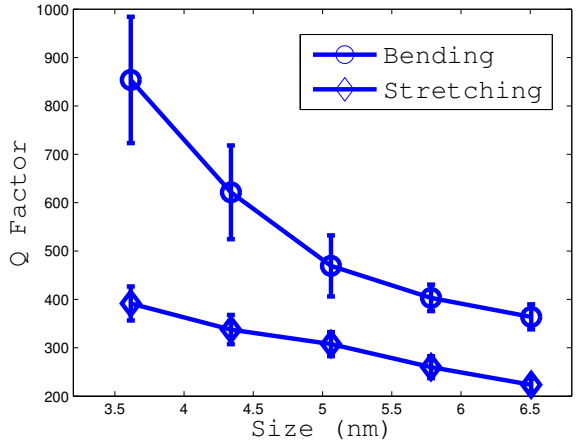

(b)

Figure 3.3: Variation of Q factor with size for bending and stretching deformation (a) Nickel and (b) Copper.

Using classical theory, dissipation is obtained by solving the coupled thermo-elastic equation. The equation for heat flow, in the presence of a strain field, is given as [45]

$$\frac{\partial \theta}{\partial t} = \chi \nabla^2 \theta - \frac{E\alpha T_0}{(1-2\sigma)C_v} \frac{\partial}{\partial t} \sum_j \epsilon_{jj} \tag{3.5}$$

Here, χ is the thermal diffusivity, θ is the change in temperature from initial value, E is Young's modulus, σ is Poisson's ratio, α is the linear thermal expansion coefficient, T_0 is the equilibrium (initial) temperature and ϵ_{jj} are the diagonal components of the strain tensor. For the case of uniform strain, the term $\sum_j \epsilon_{jj}$ in Eqn.(3.5) has no spatial dependence. For such a case, and with the initial condition $\theta(x,0) = 0$, the above equation admits a solution of the form $\theta(x,t) = \theta(t)$. The spatial uniformity of temperature field implies that there is no heat flow and, therefore, no entropy generation. Hence, the dissipation value is predicted to be zero for the case of uniform strain field. For the case of flexure, where the strain field is non-uniform, heat flow takes place and dissipation admits a finite positive value. Thus, from the classical theory we expect that dissipation will be more for the case of flexure. However, for the sizes studied, we observe that flexure deformation is less dissipative in comparison with the case of uniform strain field.

In-order to understand the observed trend in dissipation rate, we first elucidate the governing dissipation mechanism. For stretching deformation the resulting strain field is spatially uniform. For uniform strain field and in the frequency range studied, dissipation takes place due to Akhiezer mechanism [1]. We provide a brief description of Akhiezer damping.

Akhiezer mechanism

Akhiezer dissipation takes place due to the difference in the interaction of strain field with the vibrational modes of the structure. The internal vibrational modes of a structure constitute the thermal phonons. The underlying Akhiezer dynamics can be understood by considering a simplified case of two vibrational modes which have different interaction with the strain field. Figure 3.4 depicts the Akhiezer damping mechanism. The modes are represented as harmonic oscillators 1 and 2. The oscillators are initially in equilibrium, hence, each of them have a thermal energy of k_bT. Here, k_b is the Boltzmann constant and T is the temperature of system. Strain field modulates the potential energy curve and, hence, the frequency of oscillators. For the ith oscillator, frequency, ω_i, varies with strain, ϵ, as

$$\omega_i = \omega_i^0(1 - \epsilon\lambda_i). \tag{3.6}$$

Here, ω_i^0 is the frequency in reference configuration and λ_i is the Grüneisen parameter.

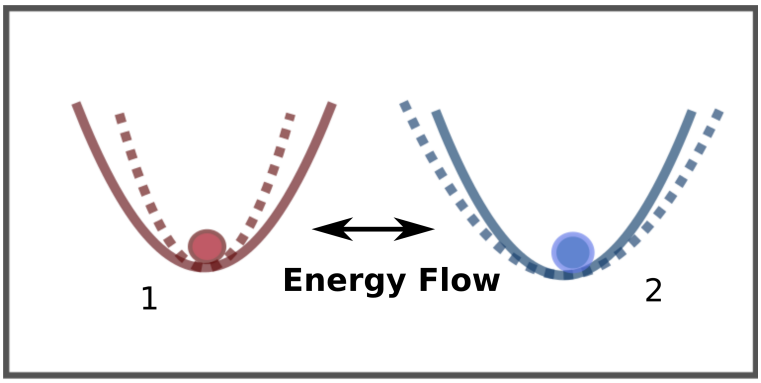

Figure 3.4: A schematic illustrating Akhiezer dynamics. The two oscillators, 1 and 2, are initially in equilibrium. Strain modulates the potential energy profile for the oscillators. The solid curve shows the potential energy profile in the reference configuration while the dashed ones correspond to strained configuration. For oscillator 1 strain increases the curvature while it decreases for 2.

Frequency modulation results in a change in modal energy. The change in energy due to the imposed strain can be obtained by using the concept of adiabatic invariant. When the curvature of an oscillator is modulated, such that the rate of modulation is slow in comparison with the frequency of the oscillator, the ratio of its energy to frequency remains conserved [34]. It then follows that $\frac{d\frac{E_i}{\omega_i}}{d\epsilon} = 0$. E_i is the energy of the ith oscillator. Expanding the differential operator we get $dE_i^\epsilon = -\frac{d\omega_i}{\omega_i}E_i$. dE_i^ϵ represents the differential change in energy for the ith oscillator due to the change in ϵ. Using the relation between ω_i and ϵ from Eqn.(3.6) we obtain

$$dE_i^\epsilon = -\lambda_i E_i d\epsilon \tag{3.7}$$

For the case, when the two oscillators have different values of λ_i, the applied strain will result in an energy difference between them. The modes will interact with each other and tend to restore energy equipartition. The differential energy change, dE_i^m, due to the inter-modal interaction can be described using the relaxation time approximation as $dE_i^m = \frac{(< E > -E_i)dt}{\tau}$. Here, $< E >$ is the mean energy of the system and τ is the relaxation time. The total energy change, dE_i, for the ith mode is then given as $dE_i = dE_i^\epsilon + dE_i^m$. For an oscillating strain field with strain amplitude ϵ_0 and oscillation frequency ω_ϵ we obtain

$$\frac{dE_i}{dt} = \frac{< E > -E_i}{\tau} - \lambda_i E_i \omega_f \epsilon_0 cos(\omega_f t) \tag{3.8}$$

The time rate of change of $< E >$ can be obtained by adding Eqn.(3.8) for different values of i and is

given as

$$\frac{d < E >}{dt} =< \lambda >< E > \omega_f \epsilon_0 cos(\omega_f t) + \Delta\lambda \Delta E \omega_f \epsilon_0 cos(\omega_f t) \tag{3.9}$$

Here, $< \lambda >= \frac{\lambda_1 + \lambda_2}{2}$, $\Delta\lambda = \frac{\lambda_1 - \lambda_2}{2}$ and $\Delta E = \frac{E_1 - E_2}{2}$. Integrating Eqn.(3.9) for the nth oscillation period and taking $< E >$ to be constant in the R.H.S we obtain

$$< E((n+1)T_p) > - < E(nT_p) >= \int_{nT_p}^{(n+1)T_p} \Delta\lambda \Delta E(t) \omega_f \epsilon_0 cos(\omega_f t) dt. \tag{3.10}$$

T_p is the oscillation time period and is related to ω_f as $T_p = \frac{2\pi}{\omega_f}$. Further, using Eqn.(3.8) we obtain

$$\frac{d\Delta E}{dt} + \frac{\Delta E}{\tau} = \Delta\lambda < E > \omega_f \epsilon_0 cos(\omega_f t). \tag{3.11}$$

Approximating $< E >= k_b T$, the above equation admits an analytical solution. Using the analytical solution for ΔE in Eqn.(3.10) we obtain

$$E_{disp} = \pi k_b T \Delta\lambda^2 \epsilon_0^2 \frac{\omega_f \tau}{1 + (\omega_f \tau)^2} \tag{3.12}$$

Here, $E_{disp} =< E((n+1)T_p) > - < E(nT_p) >$. Eqn.(3.12) represents the change in mean energy of thermal oscillators for one oscillation period. Clearly, for $\Delta\lambda \neq 0$, the mean energy of the oscillators increases with time. This increase in energy takes place at the expense of mechanical energy and is the case for Akhiezer damping.

For the case when $\omega_f \tau < 1$, Eqn.(3.12) gives $E_{disp} \propto \omega_f$. For stretching deformation ω_f was taken to be the same as that for bending. Using beam theory, ω_f for mode 1 is obtained as $\omega_f = w\sqrt{\frac{E_{bend}}{12\rho}}\left(\frac{4.730}{L_0}\right)^2$. In this expression, E_{bend} is the effective Young's modulus in bending, L_0 is the length and w is the width of the beam. From the expression for ω_f we observe that for structures with fixed L_0, ω_f decreases with the decrease in w. Hence, E_{disp} is expected to decrease with the decrease in w, assuming other parameters in Eqn.(3.12) have a weaker size dependence. This explains the increase in Q factor with the decrease in size as observed using MD simulation.

We now consider the phonon dynamics in an oscillating nano-wire with spatial flow of energy. We first consider the case of flexure deformation. The results for the flexure deformation are, then, compared with the case of uniform strain field.

Phonon Dynamics

In flexure deformation, the resulting strain field is no longer uniform. The strain field varies linearly along the lateral direction (see appendix A.2 for strain field calculation). Figure 3.5 shows the strain field variation

along the lateral (y) direction as obtained using MD simulation. A non-uniform strain field results in a spatial energy gradient. The flow of energy due to the imposed spatial gradient results in an additional dissipation known as the thermo elastic damping (TED).

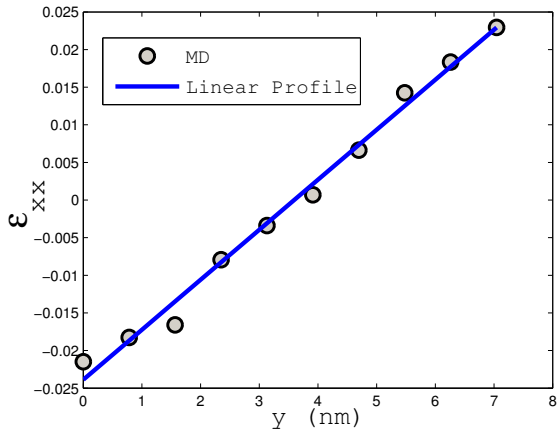

Figure 3.5: Variation of strain profile along the lateral direction.

In-order to understand the observed trend, we first develop equations governing the energy for thermal modes when the resulting strain field is non-uniform. We, again, consider a simple case where we have two different thermal modes 1 and 2. In-order to consider energy transport, the modes are now represented as traveling waves. We consider a one dimensional case with the flow of energy confined along the lateral direction(y) of the beam. Since, the strain gradient is maximum along the y direction for bending deformation, this is a valid approximation. For such a case, we can have the wave as either traveling upward or downward. Figure 3.6 depicts the thermal modes represented as upward and downward traveling waves along the lateral direction of an oscillating beam. Henceforth, the superscripts $+$ and $-$ refers to waves traveling along the positive and negative y axis, respectively.

Let $E_i^+(y)$ and $E_i^-(y)$ represent the energy density associated with the upward and downward traveling waves for thermal mode i. The change in the energy density due to strain and inter-modal interaction is described using the equations developed before for the case of Akhiezer damping. The strain, however, for the present case is a spatially varying field and needs to be taken into consideration. Further, we also need to account for the energy change due to the spatial flow. The energy change due to the spatial flow is given using the wave equation [68]. The equation governing the energy density for a thermal mode i is then obtained as

$$\frac{\partial E_i^{+,-}(y,t)}{\partial t} + v_g^{+,-}\frac{\partial E_i^{+,-}(y,t)}{\partial y} = \frac{< E(y,t) > -E_i^{+,-}(y,t)}{\tau} - \lambda_i E_i^{+,-}\frac{d\epsilon(y,t)}{dt} \tag{3.13}$$

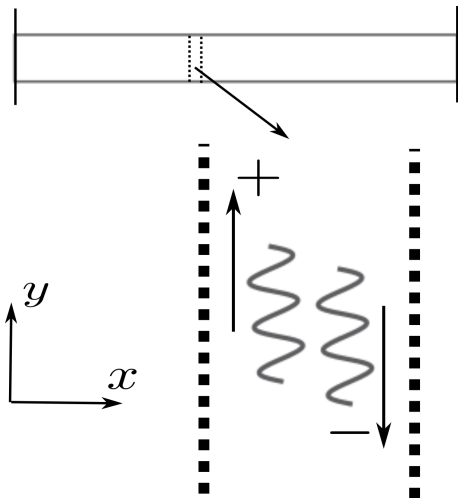

Figure 3.6: Thermal modes represented as upward and downward traveling waves for the case of flexure motion.

Here, $v_g^{+,-}$ represents the mode group velocity and satisfies the relation $v_g^+ = -v_g^- = |v_g|$. $< E(y,t) >$ is the mean energy density given as $< E(y,t) >= \frac{1}{4}\sum_{i=1}^{2} E_i^+(y,t) + E_i^-(y,t)$. Eqn.(3.13) is the phonon Boltzmann transport equation [68] represented in terms of modal energy. A source term, due to mechanical coupling, has been included in the transport equation. Further, we have considered a simplified case with wave velocity confined along one-dimension. Also, we have considered only two thermal modes, effectively representing the longitudinal and transverse modes. The value of $|v_g|$ was determined using the relation $|v_g| = \sqrt{\frac{C_{11}}{\rho}}$. Here, C_{11} is the elastic constant and ρ is the material density. For the one dimensional case, the effective group velocity needs to be scaled [52] by a factor of $\frac{1}{2}$ and was taken into consideration.

We consider $\epsilon(y,t) = -\kappa y sin(\omega_f t)$ as the strain field along the lateral direction for bending. κ is curvature of the deformed beam. For small strain in the elastic regime, the computed Q factor was found to be independent of κ and hence we set $\kappa = \frac{0.02}{w}$. Eqn.(3.13) needs to be supplemented with a proper boundary condition at the ends. Adiabatic boundary condition implies that the energy density for + and − waves for a given mode should be the same at $y = +\frac{w}{2}$ and $y = -\frac{w}{2}$. Eqn.(3.13) was solved numerically using the finite difference method. Adiabatic boundary condition was used. The case of nickel was considered. The same width size, as taken in MD simulations, was used. For a given size, oscillation frequency was also taken to be the same as that obtained using MD. The value of τ was considered as a function of size and was obtained from previous studies. We set $\lambda_1 = 1.8$ and $\lambda_2 = 0.60$. The dissipation rate, E_{disp}, was computed as the rate of increase of average internal energy, $< U >$, per unit period. $< U >$ for the n_{th} period is obtained as $< U >= \frac{1}{T_p}\int_{nT_p}^{(n+1)T_p}\int_{-w/2}^{w/2} < E(y,t) > dydt$. The energy stored, E_{stored}, was obtained using

the relation $E_{stored} = \int_{-w/2}^{w/2} \frac{1}{2} E_{bend}(\epsilon(y))^2 dy$. Q factor was then computed as $Q = 2\pi \frac{E_{stored}}{E_{disp}}$.

We also obtained the Q factor for stretching deformation using Eqn.(3.13). For stretching deformation we used $\epsilon(y,t) = \epsilon_0 sin(\omega_f t)$. For a given cross-sectional area, the oscillation frequency was taken to be the same as that for bending deformation. Figure 3.7 shows the plot of Q_r with size for the case of nickel as obtained using Eqn.(3.13). Q_r is defined as the ratio of Q factor for bending to that of stretching deformation. The plot also depicts the values of Q_r obtained from MD simulations. The results computed from phonon dynamics are in agreement with MD simulations with some deviations for smaller size.

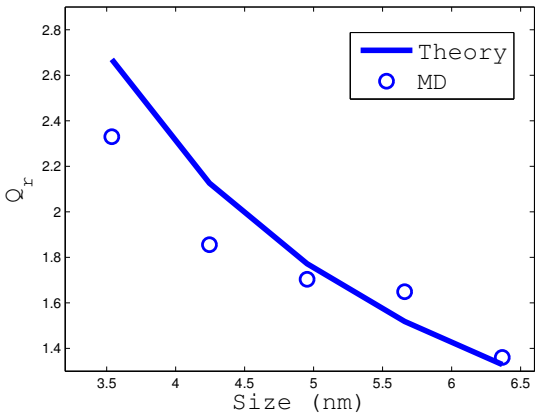

Figure 3.7: Variation of Q_r, the ratio of Q factor for bending to stretching deformation, with size as obtained using one-dimensional model.

From this simple model, we can infer why dissipation is lower for the case of flexure for smaller sizes. When the strain field is uniform, dissipation takes place due to difference in energy between the two thermal modes. In the case of flexure, energy difference between the two groups varies linearly along the lateral direction and attains a maximum value at the boundaries. A spatial flow of energy takes place due to the established energy gradient. Surface aids in establishing local equilibrium between the incoming and outgoing waves. This effectively reduces the time required for energy transfer between the two groups and thus helps in lowering dissipation.

It would, also, be useful to identify the important parameters that govern dissipation for the two deformation modes. For the case of stretching deformation, we established before that dissipation takes place due to difference in the energy between the two mode groups.The imposed strain results in an energy difference between the groups. An inter-modal current flow takes place leading to entropy generation. In the limit that $\lambda_1 = \lambda_2$, the two modes will always have the same energy value. In this limit, the stretching deformation will have no dissipation (using Eqn.(3.12)). For such a case, dissipation will be higher for the case of flexure

for all the sizes.

Since, there is no transport of energy between different regions for the case of stretching, Q factor does not depend on the wave velocity magnitude $|v_g|$. However, for the case of flexure $|v_g|$ plays an important role. A higher wave speed enhances the rate of energy transport. This results in lowering the equilibration time and hence reduces the dissipation rate. This was, indeed, confirmed by solving Eqn.(3.13) for different values of $|v_g|$. E_{disp} was found to decrease with the increase in $|v_g|$ and keeping other parameters constant.

3.2.2 Role of Tension

We also studied the role of tension on Q factor for a fixed-fixed nickel beam and under flexure deformation. The initial tension was provided by giving the structure a strain along the length direction and then keeping the ends fixed. Q factor was, then, computed using method A as described in the methods section. The structure with zero axial stress was taken as the reference configuration. The purpose of studying the role of tension on Q factor is two-fold. It has been shown that tensile stress can be used to enhance the Q factor for a nano-wire[74**?**]. It would, therefore, be useful to study the role of tension for the case of intrinsic damping. We develop scaling relations for the variation of Q factor with the initial tension using continuum theory. Also, the under co-ordinated surface atoms in a nano-structure have residual stress. This residual stress can be accounted for by considering an effective initial tension in the nano-beam. Thus, a study of the role of tension would also provide an understanding of the role of surface tension on damping in a nano-structure.

We computed Q factor for a nickel nano-beam with a cross-sectional area of 12.51 $\mathring{A}^2$ and with different values of initial strain (or tension). Figure 3.8 shows the plot of Q factor with strain in the structure, as obtained using MD simulation. Q factor shows a non-monotonic dependence on strain. It first increases with the increase in tensile strain and then decreases. A similar observation was also made in previous study[**?**]. In-order to understand the observed scaling of Q factor with strain, we first study the variation of resonant frequency with axial tension.

Let T_0 be the tension in nano-beam and E_{bend} be the effective Young's modulus in bending. The equation governing the free vibration of a beam is given as [55]

$$E_{bend} I \frac{\partial^4 u}{\partial x^4} - T_0 \frac{\partial^2 u}{\partial x^2} + \mu \frac{\partial^2 u}{\partial t^2} = 0 \tag{3.14}$$

Here, u is the displacement in the y direction, I is the moment of inertia and μ is the mass per-unit length. The mode shape, $\Phi(x)$, and the resonant frequency, ω_m, can be obtained by assuming a solution of the form $u(x,t) = \Phi(x) exp(i\omega_m t)$. Using this variable-separable solution in Eqn.(3.14), we get an eigen-value

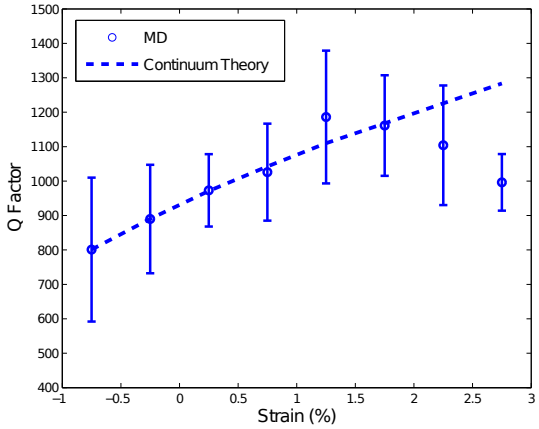

Figure 3.8: Variation of Q factor with axial strain for the case of nickel.

problem for $\Phi(x)$ and ω_m as

$$\left(E_{bend}I\frac{d^4}{dx^4} - T_0\frac{d^2}{dx^2}\right)\Phi(x) = \mu\omega_m^2\Phi(x) \tag{3.15}$$

The eigen-value problem was solved numerically using the finite element (FEM) to determine $\Phi(x)$ and ω_m. For a beam subjected to an axial strain, ϵ_s, the resultant tension, T_0, is given as $T_0 = AE_{stretch}\epsilon_s$. Here, A is the cross-sectional area and $E_{stretch}$ is the effective Young's modulus of the beam in stretching deformation. $E_{stretch}$ is, in general, different from E_{bend} for the case of a nano-wire. We provide a brief description of the method to obtain $E_{stretch}$ and E_{bend} using the quasi-harmonic theory in the Appendix.

Figure 3.9 shows the plot of ω_m versus strain as obtained using Eqn.(3.15). The plot, also, depicts the results obtained using MD simulation. A good agreement between the two results is obtained. The resonant properties of a nano-beam are, therefore, aptly captured using the beam theory.

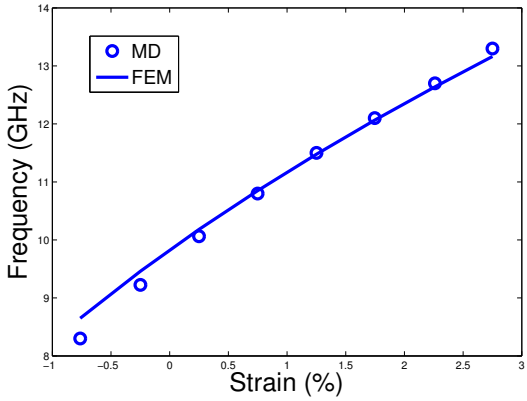

Figure 3.9: Variation of resonant frequency for the fundamental bending mode with axial strain.

The resonant properties of a nano-beam can, now, be used to study its dissipative behavior. In-order to describe dissipation using continuum theory, one needs to account for the viscous component, σ_v, of the stress. A constitutive relation governing the time evolution of σ_v is also required. We consider the phenomenological relation [40]

$$\sigma_v = E_{loss}\dot{\epsilon}. \tag{3.16}$$

Here, E_{loss} is the loss modulus and $\dot{\epsilon}$ is the strain rate. The value of E_{loss} was determined such that we get the same Q factor, as that obtained using MD, for the zero strain case. The energy dissipated per unit period, E_{disp}, is then obtained as

$$E_{disp} = \int_0^{\frac{2\pi}{\omega_m}} \int\int\int \sigma_v \dot{\epsilon}(x,y,z,t) dv dt \tag{3.17}$$

Here $\epsilon(x,y,z,t)$ is the strain field in the vibrating nano-beam. For a beam with a displacement profile, $u(x)$, the strain field, $\epsilon(x,y,z)$, is given as

$$\epsilon(x,y,z) = -y\frac{d^2u(x)}{dx^2} + \frac{1}{2}\Big(\frac{du(x)}{dx}\Big)^2 \tag{3.18}$$

The first term in the above expression corresponds to bending deformation and the second term corresponds to increase in length (or stretching) of the neutral axis of the beam. The stretching component is a non-linear term and can be neglected for small deformation. Thus, for an oscillating beam with mode shape $\Phi(x)$ and angular frequency ω_m we get $\epsilon(x,y,z,t) = -y\frac{d^2\Phi(x)}{dx^2}sin(\omega_m t)$. This expression for strain field was used in Eqn.(3.17) to determine E_{disp}. The value of E_{loss} was taken to match E_{disp} obtained from MD simulation for the case of no initial tension. For a structure under resonant motion, the maximum elastic energy is equal to the maximum kinetic energy. The maximum elastic energy stored, E_{stored}, was thus obtained as $E_{stored} = \int_0^L \frac{1}{2}\mu\Phi^2(x)\omega_m^2 dx$. From these values Q factor was determined. Figure 8 shows the plot of Q factor vs. strain, as obtained, using continuum theory. The initial increase in Q factor with applied strain is described using continuum relation. However, the theory fails to capture the decrease in Q factor observed for higher strains. For higher strain values, E_{loss} can no longer be assumed to be a constant as has been used in our model. The value of E_{loss} depends on the material properties such as the relaxation time, thermal conductivity, etc. These properties are expected to change for large strain values. Also, additional mechanisms, such as mode coupling, can become active for larger strains and hence modify the value of E_{loss}.

3.3 Conclusions

Dissipation in nano-wires under two different modes of deformation, stretching and bending, were studied. Q factor was found to be lower for the stretching motion in comparison with the bending mode. Further, with the decrease in cross-sectional area of the beam the difference in Q factor between the two modes increased. A simple model using phonon dynamics was developed to explain the observed scaling of Q factor with size. We also studied the effect of axial strain on dissipation rate in the flexure motion. A non-monotonic dependence for Q factor was observed. The initial increase in Q factor with the applied strain was explained using continuum theory.

Chapter 4

Multi-Scale Modeling

4.1 Introduction

Intrinsic dissipation takes place as a result of the coupling between the mechanical deformation and the internal thermal vibrations in a structure. An irreversible flow of energy takes place resulting in an increase in the entropy of the system. In the classical thermo-elasticity, the thermal vibrations are quantified in terms of the temperature field. Such a description invokes the condition of local equilibrium. The mean thermal energy or the temperature field, then, suffices as a complete description of the system. However, this approximation is not valid in the case of nano-resonators.

Nano-resonators have vibrational frequency in the order of few GHz. For such high frequencies of vibration, the time-scale of mechanical deformation becomes comparable to the phonon relaxation time. Deformation of a structure, at rates comparable to the phonon relaxation time, drives the phonon out of equilibrium. For such cases, the mean thermal energy or the temperature, is not an adequate description of the thermal field. Additional variables, that characterize the deviation from equilibrium, are required to describe the thermal field. The out of equilibrium phonon population, then, results in the absorption of energy from the mechanical deformation. Akhiezer mechanism [1] characterizes the damping due to this local disturbance of the phonon population. The dissipation rate due to the Akhiezer mechanism is, often, quantified using a reduced order two oscillator model [4]. In this work, we provide a detailed quasi-harmonic based multi-scale approach to model intrinsic dissipation due to perturbation of the local phonon distribution.

The thermal vibrations in a structure and its coupling with the mechanical field are, accurately, described using the QHM method[72, 80]. The existing QHM frame-work is, however, valid for quasi-static deformation. In this work we extend the QHM method to model the intrinsic dissipation in solids under the high frequency vibrations. We introduce a non-equilibrium component of the stress tensor, $\boldsymbol{\sigma}_{neqb}$. The stress tensor characterizes the deviation from local equilibrium and vanishes under quasi-static deformation. A constitutive relation, that governs the time evolution of $\boldsymbol{\sigma}_{neqb}$, is obtained. The time evolution for $\boldsymbol{\sigma}_{neqb}$ is described by a forcing and a relaxation term. The forcing rate is parametrized in terms of a dissipation

tensor $\mathbf{D}$ which is obtained using QHM. We, also, discuss a stochastic sampling method to obtain $\mathbf{D}$. The relaxation dynamics for $\boldsymbol{\sigma}_{neqb}$ is obtained using Langevin dynamics in the basis of normal modes. In this approach, each of the modes is modeled as a noisy harmonic oscillator. The proposed methodology is, then, used to study the effect of different parameters on the dissipation rate. Vibrations with frequency in the range of few GHz are considered. The results are compared with those obtained using non-equilibrium MD.

The chapter is organized as follows. In section 4.2 we obtain the constitutive relation for $\boldsymbol{\sigma}_{neqb}$ using QHM. Methods to obtain the dissipation tensor, $\mathbf{D}$, and the stress relaxation rates are, then, discussed. In section 4.3 we apply the method to compute the dissipation rate as a function of different parameters. The comparisons with the MD results are provided alongside. Finally, the conclusions are given in section 4.4.

4.2 Theory and Method

In the methods section we will first obtain an expression for the non-equilibrium stress using the QHM method. We will then, derive, a constitutive relation that governs the time evolution of the non-equilibrium stress. The constitutive relation, as obtained, shows two physical processes, a forcing term and a relaxation term. The forcing term will be characterized in terms of a dissipation tensor $\mathbf{D}$. An expression for $\mathbf{D}$, in terms of the material parameters, will be obtained. We will also discuss a non-equilibrium sampling method to parametrize $\mathbf{D}$. We will, then, describe the stress relaxation behavior. Lanegvin dynamics and Green Kubo forumation will be used in this regard.

4.2.1 Non-Equilibrium Stress

In this section we shall derive an expression for stress tensor under non-equilibrium condition. We consider the case of crystalline structure that is amenable to the quasi harmonic approximation. This implies that the atoms undergo small thermal vibrations about the mean positions. For a given mean position of atoms, the quasi-harmonic approximation, then, suffices to describe the thermal vibrations. We briefly describe the QHM method. For the details of QHM the reader is referred to [72, 80]. In essence, the QHM method considers a Taylor series expansion of the governing inter-atomic potential for a given mean position of the atoms. The potential energy is, then, approximated by retaining the second order terms in the expansion. The quadratic expression for the truncated Hamiltonian is decoupled using normal modes. These normal modes constitute a set of orthogonal directions in the configuration space. For the quadratic Hamiltonian, the motion along one direction is independent along the other.

Using QHM, the Hamiltonian, can, thus, be written in terms of the modal co-ordinates. Let a_i denote the mode displacement, ω_i denote the frequency and v_i be the velocity for a mode i. The Hamiltonian, H,

is, given as

$$H = \sum_{i=1}^{nmodes} \frac{1}{2} m\omega_i^2 a_i^2 + \frac{1}{2} m v_i^2. \tag{4.1}$$

Here, $nmodes$ is the number of modes and m is the atomic mass. $nmodes = 3 \times nat$, where nat is the number of atoms in the system.

The thermal state of the system is completely described by specifying the probability density function (PDF) for the mode co-ordinates. Under the equilibrium condition, characterized by temperature, T, the PDF for a_i is given as

$$P(a_i) = \frac{1}{Z} exp\left(-\frac{m\omega_i^2 a_i^2}{2k_b T}\right). \tag{4.2}$$

Here, k_b is the Boltzmann constant and Z is the partition function.

The PDF in Eq.(4.2) is only valid under the condition of local equilibrium. When this condition is violated, the modes no longer satisfy the energy equi-partition principle. Instead, each mode i is characterized by a non-equilibrium temperature T_i. The PDF, $P_{neqb}(a_i)$, for a_i for such a state is, then, given as

$$P_{neqb}(a_i) = \frac{1}{Z} exp\left(-\frac{m\omega_i^2 a_i^2}{2k_b T_i}\right). \tag{4.3}$$

This expression for $P_{neqb}(a_i)$ has been obtained using the principle of maximum entropy[29]. A derivation for this is provided in the appendix section B.1.

We, shall, now derive an expression for the stress tensor for the non-equilibrium state. Let $\boldsymbol{\sigma}$ denote the thermal stress tensor and let σ_{ij} denote its components. σ_{ij} is given as

$$\sigma_{ij} = \frac{1}{V} \frac{\partial < H >}{\partial \epsilon_{ij}}. \tag{4.4}$$

Here, and for all future purpose, the symbol $< ... >$ refers to the ensemble average. V is the volume and ϵ_{ij} are the components of the strain tensor, $\boldsymbol{\epsilon}$. Using the expression for H in Eq.(4.1) and the PDF in Eq.(4.3), we obtain

$$\sigma_{ij} = \frac{1}{V} \sum_{n=1}^{nmodes} \int \frac{1}{2} m \frac{\partial \omega_n^2}{\partial \epsilon_{ij}} a_n^2 P(a_n) da_n \tag{4.5}$$

We define λ_n^{ij} such that $\lambda_n^{ij} = \dfrac{-1}{\omega_n} \dfrac{\partial \omega_n}{\partial \epsilon_{ij}}$. Using the definition of λ_n^{ij} and further simplifying Eq.(4.5) we get

$$\sigma_{ij} = \frac{1}{V} \sum_{n=1}^{nmodes} \lambda_n^{ij} E_n. \tag{4.6}$$

Here, E_n is the mean energy for mode n and is related to T_n as $E_n = k_b T_n$. Using a little algebra, the

expression for σ_{ij} can be, further, re-casted as

$$\sigma_{ij} = \frac{nmodes}{V}\overline{\lambda^{ij}}\ \overline{E} + \frac{1}{V}\sum_{n=1}^{nmodes} \Delta\lambda_n^{ij}\Delta E_n. \tag{4.7}$$

Here, and for all future reference, the symbol $\overline{x}$ is defined as $\overline{x} = \dfrac{1}{nmodes}\displaystyle\sum_{n=1}^{nmodes} x_n$, where x_n is any mode variable for a mode n. Also, $\Delta E_n = E_n - \overline{E}$ and $\Delta\lambda_n^{ij} = \lambda_n^{ij} - \overline{\lambda^{ij}}$. We have, thus, decomposed the stress into two components. Under the condition of equilibrium, the modes satisfy the energy equi-partition principle and we have $\Delta E_n = 0$. The second term in Eq.(4.7), then, vanishes. We, thus, identify this term as the non-equilibrium component of the stress tensor, $\boldsymbol{\sigma}_{neqb}$. While the equilibrium stress is a state property, the non-equilibrium stress depends on the rate of deformation of the system. In the next section we will derive an Eq. that governs the time evolution of $\boldsymbol{\sigma}_{neqb}$. For all future purpose we shall, simply, refer to $\boldsymbol{\sigma}_{neqb}$ as $\boldsymbol{\sigma}$. The components of $\boldsymbol{\sigma}$ are, therefore, given as

$$\sigma_{ij} = \frac{1}{V}\sum_{n=1}^{nmodes} \Delta\lambda_n^{ij}\Delta E_n. \tag{4.8}$$

4.2.2 Constitutive Relation

In this section we will derive the constitutive relation that governs the time evolution of $\boldsymbol{\sigma}$. Using physical arguments we first state the result. We shall, then, provide a derivation for the different terms in the expression based on the QHM method. We will also present a non-equilibrium sampling approach to parametrize the constitutive relation in the next section.

The time evolution of $\boldsymbol{\sigma}$ is given as

$$\frac{d\boldsymbol{\sigma}}{dt} = \mathbf{D}\frac{\partial\boldsymbol{\epsilon}}{\partial t} + \left(\frac{\partial\boldsymbol{\sigma}}{\partial t}\right)_{relax}. \tag{4.9}$$

Here, $\mathbf{D}$ is a fourth order dissipation tensor, the second term on the R.H.S describes the relaxation of the stress tensor. An expression for $\mathbf{D}$ will be derived subsequently. Eq.(4.9) shows that the evolution of $\boldsymbol{\sigma}$ results from two competing factors. Deformation of the system at any finite rate drives it out of equilibrium. Under the linear approximation, the rate at which the system deviates from the equilibrium state is proportional to the driving rate. The first term in the above Eq. describes this phenomenon. Further, if left unperturbed, the system tends to relax towards the corresponding equilibrium state. $\boldsymbol{\sigma}$, which measures the deviation from the equilibrium state, correspondingly relaxes towards a zero value. This is described by the second term in Eq.(4.9).

In-order to derive the Eq. that governs the time evolution of σ_{neqb} we take the derivative of Eq.(4.8) with respect to time. We, then, obtain

$$\dot{\sigma}_{ij} = \frac{1}{V} \sum_{n=1}^{nmodes} \Delta\lambda_n^{ij} \Delta\dot{E}_n. \tag{4.10}$$

In the above Eq. we need to substitute the time derivative of ΔE_n. The energy of a mode changes due to two processes. The applied deformation field injects (or extracts) energy from each of the modes. Further, the modes interact with each other and an inter-modal flow of energy takes place. We shall first consider the energy change due to the applied strain. The rate of change of E_n due to the change in strain, ϵ_{ij}, is obtained as

$$\frac{\partial E_n}{\partial \epsilon_{ij}} = \int \frac{1}{2} m \frac{\partial \omega_n^2}{\partial \epsilon_{ij}} a_n^2 P_{neqb}(a_n) da_n. \tag{4.11}$$

Using the expression for $P_{neqb}(a_n)$ in Eq.(4.3) and carrying out the integration we obtain

$$\left(\frac{\partial E_n}{\partial t}\right)_{\epsilon_{ij}} = \lambda_n^{ij} E_n \frac{d\epsilon_{ij}}{dt}. \tag{4.12}$$

Here, $\left(\frac{\partial E_n}{\partial t}\right)_{\epsilon_{ij}}$ denotes the time rate of change of E_n due to the change in ϵ_{ij}.

Adding the above Eq. for all values of n we obtain

$$\left(\frac{\partial \overline{E}}{\partial t}\right)_{\epsilon_{ij}} = \overline{\lambda^{ij}}\ \overline{E} \frac{d\epsilon_{ij}}{dt} + \overline{\Delta\lambda^{ij} \Delta E} \frac{d\epsilon_{ij}}{dt}. \tag{4.13}$$

Here, $\left(\frac{\partial \overline{E}}{\partial t}\right)_{\epsilon_{ij}}$ denotes the time rate of change of $\overline{E}$ due to the change in ϵ_{ij}. For small deformations in the linear regime, the system shows a weak deviation from the equilibrium state. Under such a condition, the second term in the RHS of Eq.(4.13) is negligible in comparison with the first term. Using this approximation and taking the difference between Eq.(4.13) and Eq.(4.12) we get

$$\left(\frac{\partial \Delta E_n}{\partial t}\right)_{\epsilon_{ij}} = \Delta\lambda_n^{ij} k_b T \frac{d\epsilon_{ij}}{dt}. \tag{4.14}$$

Here, $\left(\frac{\partial \Delta E_n}{\partial t}\right)_{\epsilon_{ij}}$ denotes the time rate of change of ΔE_n due to the change in ϵ_{ij}. In deriving the above expression we have also used the approximation that $E_m \approx k_b T$. We have, thus, obtained an expression for the time rate of change of ΔE_m due to change in ϵ_{ij}. We will now discuss the case of inter-modal interaction.

Let $\left(\frac{\partial \Delta E_n}{\partial t}\right)_{coll}$ denote the time rate of change of ΔE_n due to inter modal interaction. Using a single relaxation time approximation this is, often, given as $\left(\frac{\partial \Delta E_n}{\partial t}\right)_{coll} = -\frac{\Delta E_n}{\tau}$. Here, τ denotes the single

relaxation time for all the modes. We will, however, not use the single relaxation time approximation. Instead, we shall resort to mode Langevin dynamics and obtain an effective relaxation rate for σ_{neqb}. In this approach, each mode n has its own characteristic relaxation time τ_n. The details of stress relaxation will be discussed in the later section. For the time being we shall just retain the expression $\left(\frac{\partial \Delta E_m}{\partial t}\right)_{coll}$ to denote the energy change due to collision.

The total rate of change of ΔE_n due to strain and the inter-modal interaction is, then, obtained as

$$\frac{d\Delta E_n}{dt} = \Delta\lambda_n^{ij}\frac{d\epsilon_{ij}}{dt} + \left(\frac{\partial \Delta E_n}{\partial t}\right)_{coll}. \tag{4.15}$$

Using this expression in Eq.(4.10) we obtain

$$\frac{d\sigma_{ij}}{dt} = \frac{1}{V}\left[\sum_{p=1,q=1}^{3,3}\sum_{n=1}^{nmodes}\Delta\lambda_n^{ij}\Delta\lambda_n^{pq}\frac{d\epsilon_{pq}}{dt} + \sum_{n=1}^{nmodes}\left(\frac{\partial \Delta\lambda_n^{ij}\Delta E_m}{\partial t}\right)_{coll}\right]. \tag{4.16}$$

In-order to write the above Eq. in a compact form we define the fourth order dissipation tensor $\mathbf{D}$. The components of $\mathbf{D}$ are given as

$$D_{ijkl} = \frac{3k_bT\rho}{m}\overline{\Delta\lambda_n^{ij}\Delta\lambda_n^{kl}}. \tag{4.17}$$

Here, ρ is density and m is the atomic mass. We realize that the second term in Eq.(4.16) denotes the relaxation of the non-equilibrium stress. Eq.(4.16) can, therefore, be re-casted as

$$\frac{d\boldsymbol{\sigma}}{dt} = \mathbf{D}\frac{\partial\boldsymbol{\epsilon}}{\partial t} + \left(\frac{\partial\boldsymbol{\sigma}}{\partial t}\right)_{relax}. \tag{4.18}$$

We, thus, obtain a constitutive relation that governs the time evolution of $\boldsymbol{\sigma}$. The dissipation tensor, $\mathbf{D}$, can be obtained from QHM using Eq.(4.17) . It, still, remains to parametrize the relaxation term in the governing Eq., this will be pursued in the latter section. Before discussing the relaxation dynamics we will discuss an alternative approach to parametrize $\mathbf{D}$. In this approach a stochastic method is used to sample the non-equilibrium states.

4.2.3 Non-Equilibrium Stochastic Sampling

In the previous section, the QHM approximation was used to obtain an expression for the non-equilibrium stress tensor, $\boldsymbol{\sigma}$. Subsequently, we derived an expression for the time evolution of $\boldsymbol{\sigma}$. We obtained a dissipation tensor, $\mathbf{D}$ that characterizes the time rate of change of $\boldsymbol{\sigma}$ due to the change in $\boldsymbol{\epsilon}$. We can, alternatively, obtain $\mathbf{D}$ by measuring the stress for a system as a function of its deviation from the equilibrium state. In this approach, we use virial stress tensor obtained using the inter-atomic potential. The QHM

approximation for the stress, as used in the previous section, is not invoked. In-order to motivate this approach we shall, first, provide a physical interpretation of $\mathbf{D}$.

We consider a system that is initially in thermal equilibrium and is subjected to a differential strain $d\epsilon_{ij}$. Let $d\sigma_{ij}^V$ denote the differential change in the virial component of stress and as measured instantaneously. The term instantaneous, here, implies time scales which are small compared with the time required for thermalization. $d\sigma_{ij}^V$, then, results from two processes. First, it results from the change in the mean position of the atoms and corresponds to the elastic contribution. Secondly, it results from the system being driven out of the equilibrium state and corresponds to the dissipative component. Let $d\sigma_{ij}^D$ denote the component of σ_{ij}^V that results from the second effect. The dissipation tensor $\mathbf{D}$ can, then, be obtained such that its components are given as

$$D_{ijkl} = \frac{\partial \sigma_{ij}^D}{\partial \epsilon_{kl}}. \tag{4.19}$$

We, will, use the above Eq. to compute D_{ijkl}. For this purpose, we need to extract the stress component that results from the deviation of the system from the equilibrium state. In-order to obtain this, we will generate atomic configurations in the non-equilibrium state and with same mean position of the atoms. The difference in the stress value of the non-equilibrium state from the equilibrium configurations, then, gives us σ_{ij}^D. Stochastic sampling approach will be used for this purpose. In essence, the stochastic sampling approach generates the micro-states according to a given PDF. For computing $\mathbf{D}$ we use a non-equilibrium PDF. Hence, the method is referred to as non-equilibrium stochastic sampling. We will briefly outline the approach here. The details of the algorithm, for performing the stochastic sampling, is discussed in the appendix section B.2.

For sampling a non-equilibrium state we, first, need to characterize it and construct the corresponding PDF. We construct the PDF in the basis of the mode co-ordinates. We consider a non-equilibrium state that results from applying an instantaneous strain ϵ_{kl} on the system. This results in different modes having different temperature. For a mode i, the temperature T_i is given as $T_i = T + \Delta\lambda_i^{kl}\epsilon_{kl}$. The different terms have the same representation as introduced before. The PDF for a_i is, then, obtained, as

$$P(a_i) = \frac{1}{Z} exp\left(-\frac{m\omega_i^2 a_i^2}{k_b T_i}\right). \tag{4.20}$$

For a given value of ϵ_{kl} we, first, determine the values of T_i for all the modes. The PDF for a_i is, then, constructed, using Eq.(4.20). We sample the values of a_i using the given PDF. The a_i values are used to determine the atomic displacement using the linear transformation. An atomic configuration is, thus, obtained. Different samples are generated in this manner. The sampled sets are, then, used to compute the

virial stress tensor. Let σ_{ij}^V denote the mean virial stress tensor for a given non-equilibrium state. We also determine σ_{ij}^V for the equilibrium configuration. The difference between the two values gives the dissipative stress σ_{ij}^D. From the slope of the linear fit of σ_{ij}^D vs ϵ_{kl}, D_{ijkl} is determined.

4.2.4 Stress Relaxation

The constitutive relation for the time evolution of $\boldsymbol{\sigma}$ in Eq.(4.9) has two governing terms. The first term on the R.H.S corresponds to the forcing term while the second one describes the relaxation towards equilibrium. The forcing term was characterized using $\mathbf{D}$. We have, already, discussed methods to obtain $\mathbf{D}$ in the previous sections. In this section we seek to characterize the relaxation behavior of the non-equilibrium stress component.

Microscopically, stress relaxation results from the interaction between the different modes. We, therefore, need to model the modal dynamics to characterize this behavior. We will use the Langevin frame-work to describe the dynamics of the modes. Further, we shall resort to the Green-Kubo formulation and obtain the stress relaxation. For the systems considered, the stress relaxation shows an exponentially decaying behavior. We will, therefore, eventually characterize the relaxation of $\boldsymbol{\sigma}$ using an effective relaxation rate, τ_{relax}, such that

$$\left(\frac{\partial \boldsymbol{\sigma}}{\partial t}\right)_{relax} = -\frac{\boldsymbol{\sigma}}{\tau_{relax}}. \tag{4.21}$$

The objective of this section is to provide an algorithm to determine τ_{relax} for different structures. It would be useful, here, to briefly outline the main steps in the algorithm. This will aid the reader in understanding the general flow of the section. We will use mode Langevin dynamics to determine τ_{relax}. The first step required for the Langevin simulation is the parametrization. Langevin simulation needs as an input the momentum relaxation time, τ_i^m, for mode i. We shall use a stochastic sampling approach to determine τ_i^m. For determining τ_i^m using the stochastic sampling approach, one needs an additional information of the noise relaxation time, τ_i^n. This closure is provided by performing a MD simulation of a reference bulk structure. The τ_i^m values are, then, used to perform the Langevin simulation and determine τ_{relax}.

The section is organized as follows. We will, first, state the governing Eq. for the mode Langevin dynamics and describe the different input parameters. We will, then, discuss the method to determine τ_i^n using MD for a bulk reference structure. Next, we shall discuss the stochastic sampling approach to determine the momentum relaxation time τ_i^m. This completes the discussion on parametrization step. Finally, the method to determine τ_{relax} using the mode Lagevin dynamics will be discussed.

Langevin Dynamics

The Eq. governing the dynamics of a mode i, using the Langevin approximation, is given as[15]

$$m\frac{d^2a_i}{dt^2} + \frac{2m}{\tau_i^m}v_i + m\omega_i^2 a_i = r_i(t). \tag{4.22}$$

Here, m is the effective mass, ω_i is the mode frequency and τ_i^m is the momentum relaxation time. r_i is the noise force with a correlation time τ_i^n such that $r_i(0)r_i(t) =< r_i^2 > exp(-t/\tau_i^n)$. For the cases considered, τ_i^n is of order of few fs. Hence, the Langevin approximation suffices for describing the mode dynamics. Further, τ_i^n, τ_i^m and r_i are related using the fluctuation dissipation theorem[15] as

$$< r_i^2 >= \frac{2mk_bT}{\tau_i^n\tau_i^m} \tag{4.23}$$

This relation will be used in the parametrization step. For evolving Eq.(4.22) we need to know the values of different terms. The mode frequency, ω_i, is obtained using the QHM method. We first use bulk MD as a parametrization step to determine τ_i^n.

We consider a bulk structure with a dimension of 8 unit cells in each direction. The structure is first equilibrated at a desired temperature using a Nosé-Hoover thermostat. It is, then, evolved as a micro-canonical ensemble. The generated trajectories are used to determine the time series data of the mode variables. We, thus, obtain the mode displacement, $a_i(t)$, the mode velocity, $v_i(t)$, and the mode force, $f_i(t)$ as a function of time.

We construct the velocity auto-correlation function (VACF), $C_{v_iv_i}(t)$, such that $C_{v_iv_i}(t) =< v_i(0)v_i(t) >$. VACF shows an oscillatory decaying behavior. From the decay rate, the momentum relaxation time, τ_i^m, is determined for the bulk structure. We need to determine the value of τ_i^n. For determining τ_i^n, we first equate the MD modal force with the mode force from the Langevin model. We, thus, obtain

$$f_i(t) = -m\omega_i^2 a_i(t) - \frac{2mv_i(t)}{\tau_i^m} + r_i(t). \tag{4.24}$$

Further, rearranging the above Eq. and taking the second moment of the L.H.S and the R.H.S we get

$$< (f_i + m\omega_i^2 a_i)^2 >=< \left(\frac{2mv_i}{\tau_i^m}\right)^2 > + < r_i^2 > . \tag{4.25}$$

In deriving this expression we used the condition that $< f_iv_i >= 0$. This indeed is true for the equilibrium

state. Further, using $< v_i^2 >= \frac{k_b T}{m}$ and the relation in Eq.(4.23) we obtain

$$< (f_i + m\omega_i^2 a_i)^2 >= \frac{4mk_bT}{(\tau_i^m)^2} + \frac{2mk_bT}{\tau_i^n \tau_i^m}. \tag{4.26}$$

The L.H.S of the above Eq. can be computed using the time series data of mode variables $f_i(t)$ and $a_i(t)$. These are obtained from the bulk MD simulation. τ_i^m was determined using the VACF and as discussed before. These values are, then, substituted in Eq.(4.26) to determine τ_i^n. We compute τ_i^n for different modes. A strong dependence of τ_i^n on ω_i was observed. We perform a polynomial fit of τ_i^n vs. ω_i using the data set obtained. The fitted function is the first step in the parametrization for Langevin simulation. This information will now be used to determine the τ_i^m values of any other structure of interest.

We consider the case of a structure with free surface. In-order to describe the mode dynamics for this structure, we need to estimate the values of τ_i^m. The values of τ_i^m for structures with free surface is, in general, different from the bulk case. The presence of surfaces modifies the phonon spectrum and its dynamics. The surface effect on the phonon dynamics is, often, described using a phenomenological relation for the surface scattering term. Here, we will use the underlying inter-atomic potential and a stochastic sampling approach to capture the surface effect on the phonon dynamics.

We shall use Eq.(4.26) to determine τ_i^m for the finite sized structure of interest. The unknowns in Eq.(4.26) are the terms on the L.H.S and the value of τ_i^n. We already parametrized τ_i^n as a function of ω_i using a reference bulk structure and, hence, is known. For estimating the term on the L.H.S of Eq.(4.26), we recognize that an ensemble averaging is required. We, therefore, need to generate ensembles of micro-states. For this purpose we will use a stochastic sampling approach. The details of the stochastic sampling approach will be discussed in the appendix section B.2. Here, we briefly outline the main steps.

In the stochastic method, we generate different samples of the mode variables a_i with a given PDF. The PDF for a_i is obtained using the QHM approximation and is given using Eq(4.2). Using this PDF, different instances of a_i are generated. The a_i values are, then, transformed to obtain the per-atom displacement. For each sampled set of a_i values, an atomic configuration is, thus, obtained. For the given atomic configuration the per atom forces are computed using the underlying inter-atomic potential. These are used to compute the mode force f_i. The L.H.S of Eq.(4.26) is, then, determined as

$$< (f_i + m\omega_i^2 a_i)^2 >= \frac{1}{nensb} \sum_{j=1}^{nensb} [(f_i + m\omega_i^2 a_i)^2]_j. \tag{4.27}$$

Here, *nensb* is the number of ensemble considered and $[...]_j$ is the value of the enclosed variable for the jth ensemble. Eq.(4.26) is, then, used to compute τ_i^m. This completes the parametrization step for the Langevin

simulation. We will, now, use the Langevin dynamics to study the stress relaxation behavior.

We integrate the Langevin Eq. for each of the mode. We get a time series data of $a_i(t)$ and $v_i(t)$. The energy, $E_i(t)$, for a mode i is estimated as

$$E_i(t) = \frac{1}{2}m\omega_i^2 a_i^2 + \frac{1}{2}mv_i^2. \tag{4.28}$$

The modes satisfy equipartition of energy, this implies that $< E_i >= k_bT$. Hence, $\Delta E_i(t) = E_i(t) - k_bT$. We, now, use the Green-Kubo forumation and determine the non-equilibrium stress relaxation rate from the auto-correlation of equilibrium fluctuations. The stress component, σ_{ij}, is computed as $\sigma_{ij} = \sum_{k=1}^{nmodes} \Delta E_k \Delta\lambda_k^{ij}$. We construct the stress auto correlation function, $C_{\sigma_{ij}\sigma_{ij}}(t)$, such that

$$C_{\sigma_{ij}\sigma_{ij}}(t) =< \sigma_{ij}(0)\sigma_{ij}(t) > . \tag{4.29}$$

$C_{\sigma_{ij}\sigma_{ij}}(t)$ shows a decaying exponential behavior. From the decay rate of $C_{\sigma_{ij}\sigma_{ij}}(t)$ the stress relaxation rate, τ_{relax} is determined.

4.3 Results and Discussion

We, first, consider the case of a bulk Ni structure and study the dissipation rate as a function of frequency under uni-axial deformation. Morse potential is used to model the force field. Frequency values in the GHz range are considered. The dissipation rate is computed using non-equilibrium MD for comparing the results obtained using the multi-scale method. Here, we provide a brief description of the MD simulation set-up. All MD simulations were performed using the open source software LAMMPS[59].

The structure is first equilibrated at a desired temperature of 300 K. It is, then, decoupled from the thermostat. The structure is periodically deformed along the x direction and is evolved as a micro-canonical ensemble. The work done on the system results in an increase in the internal energy. From the rate of increase of internal energy per-unit period, the dissipation rate, E_{disp}, is computed. We considered 5 ensembles for each frequency of operation. For each ensemble 100 oscillation periods were taken.

For estimating the dissipation rate using the multi-scale method we need to compute the different parameters in the constitutive relation. We, first, determine the components of the dissipation tensor, $\mathbf{D}$, for the bulk structure. For uni-axial deformation along the x direction, the only required value is the D_{1111}. We determined the value of D_{1111} using the QHM method. This requires computing λ_i^{11} for all the modes. Using the λ_i^{11} values in Eq.(4.17), D_{1111} is estimated to be 1.365 GPA at 300 K.

We also determined D_{1111} using the non-equilibrium stochastic sampling method. Using this method, the dissipative component of the stress tensor, σ_{ij}^D, is obtained for different values of ϵ_{11}. Figure 4.1 shows the variation of σ_{11}^D vs ϵ_{11}. The slope of this curve gives D_{1111} and is determined to be 1.37 GPA. This is agreement with the value of D_{1111} computed using the QHM method. Figure 4.1, also, shows the variation of σ_{22}^D vs ϵ_{11}. The negative slope of this curve corresponds to a negative value of D_{1122}. The value of D_{1122} will be used, later, in computing the dissipation for the case of bi-axial deformation.

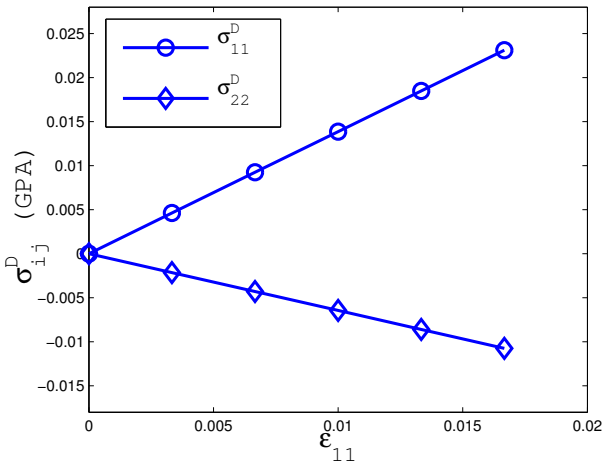

Figure 4.1: The dissipative component of the stress, σ_{ij}^D, as a function of ϵ_{11}, obtained using the non-equilibrium stochastic sampling approach.

We, also, need to estimate the stress relaxation rate, τ_{relax}. For this purpose, we obtain the mode relaxation time, τ_i^m, using MD. The mode frequencies, ω_i, are determined using the QHM method. Using these values as input, mode Langevin dynamics is performed. The stress auto-correlation function, $C_{\sigma_{11}\sigma_{11}}(t)$ is computed using Eq.(4.29). From the decay of $C_{\sigma_{11}\sigma_{11}}(t)$, τ_{relax} is estimated to be 2.07 ps.

These parameters are, then, used to determine the time evolution of σ_{11}. We consider a spatially uniform strain field that varies sinusoidally in time such that $\epsilon_{11}(x,t) = \epsilon_0 sin(\omega_f t)$. Here, ϵ_0 is the strain amplitude and ω_f is the forcing frequency. The time evolution of σ_{11} is obtained using Eq.(4.9). The dissipation rate, E_{disp}, per unit period is, then, computed as

$$E_{disp} = \int \int_0^{\frac{2\pi}{\omega_f}} \boldsymbol{\sigma} : \dot{\boldsymbol{\epsilon}} dt dV. \tag{4.30}$$

Figure 4.2(a) shows the plot of E_{disp} vs ω_f obtained using the multi-scale approach. The figure also shows the MD results. The two results are in good agreement with each other. The multi-scale approach, therefore, aptly describes the intrinsic dissipation in bulk solids.

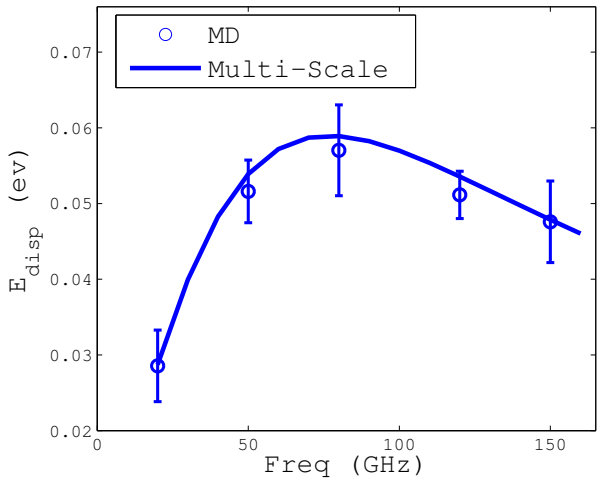

(a)

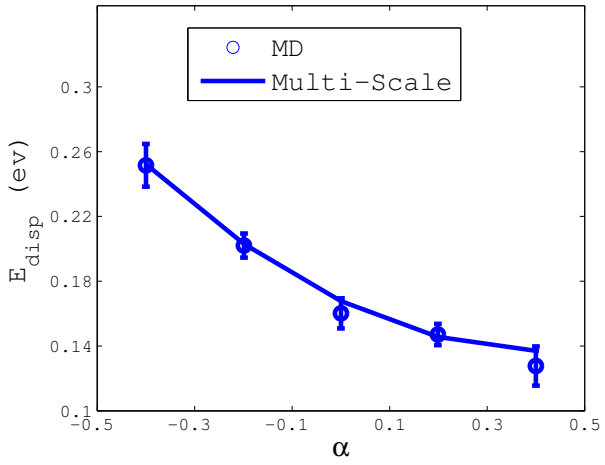

(b)

Figure 4.2: (a) E_{disp} as a function of the oscillation frequency, ω_f, for the case of bulk nickel structure. (b) E_{loss} as a function of α for the bulk nickel structure forced under an oscillation frequency of 40 GHz.

We next consider the case of bi-axial deformation. The strain field for the bi-axial deformation is given as $\epsilon_{ij}(x,t) = \epsilon_0(\delta_{1i}\delta_{1j} + \alpha\delta_{2i}\delta_{2j})sin(\omega_f t)$. Here, α is the ratio of the strain in the y direction to that in the x direction. We consider different values of α for a fixed vibrational frequency of 40 GHz. Figure 4.2(b) shows the plot of E_{disp} obtained for different values of α. We observe that E_{disp} increases for negative values of α. This is because D_{1122} is negative. Further, there exists an optimum value of α for which E_{disp} becomes minimum. Thus, by operating the resonator under such a desired strain state, the dissipation can be minimized. The negative sign of D_{1122} also suggests that it would be efficient to vibrate the structure under a dilation strain field. It would, also, be interesting to further explore the class of materials for which D_{1122} is positive. For such a material, an increase in dissipation with the increase in α value will be observed.

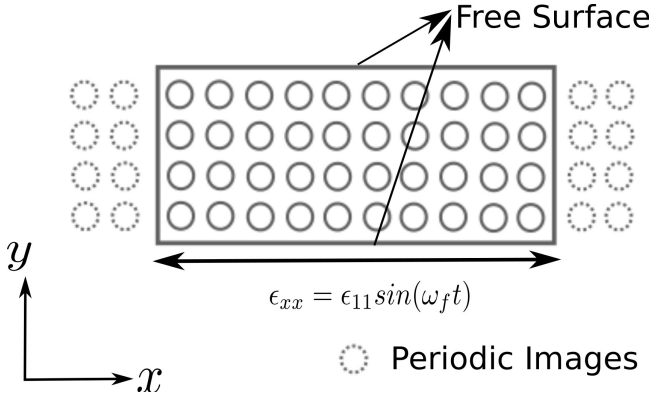

Figure 4.3: A schematic of the simulation set-up to study dissipation in structure with free surface. Periodic boundary condition is used in x and z direction (out-of-plane).

We, now, consider the case of structure with free surfaces. Figure 4.3 shows a schematic of the simulation set-up. The structure has free surfaces along the y direction while it is periodic in the other two directions. A sinusoidal strain, $\epsilon_{11}(x,t) = \epsilon_0 sin(\omega_f t)$, is applied along the x direction. Here, ϵ_0 is the strain amplitude and ω_f is the oscillation frequency. Since the structure has free surfaces along the y direction, the applied strain also results in motion along the y direction. Using elasticity theory we shall, first, obtain the displacement field along the y direction. The strain field, thus, obtained will be used an input to compute the dissipation rate.

Let $v(y,t)$ denote the displacement field along the y direction. For a linear elastic solid with cubic symmetry, the stress component, $\sigma_{22}(y)$, is given as

$$\sigma_{22}(y) = C_{11}\frac{\partial v}{\partial y} + C_{12}\epsilon_0 sin(\omega_f t). \tag{4.31}$$

Here, C_{11} and C_{22} are the elastic constants. Using the expression for σ_{22} in the momentum balance Eq.

we obtain

$$\frac{\partial^2 v}{\partial t^2} = C_{11}\frac{\partial^2 v}{\partial y^2}. \tag{4.32}$$

Further, we also have the boundary conditions as $\sigma_{22}(0) = \sigma_{22}(L) = 0$, where L is the transverse length of the structure. The above Eq. admits a solution of the form $v(y,t) = (Asin(ky) + Bcos(ky))sin(\omega_f t)$ where $k = \omega_f\sqrt{\frac{\rho}{C_{11}}}$. The constants A and B are obtained using the boundary condition. The displacement field, $v(y,t)$, is, then, given as

$$v(y,t) = -\frac{C_{11}}{C_{22}}\frac{\epsilon_0}{k}\left(sin(ky) + \frac{cos(kl)-1}{sin(kl)}cos(ky)\right)sin(\omega_f t). \tag{4.33}$$

Here, k is the wave number. For the frequency range and the dimensions of the structure considered, the strain field in Eq.(4.33) is nearly uniform. The average strain, $\epsilon_{22}(t)$, in the y direction is, then, obtained as $\epsilon_{22}(t) = \frac{v(L,t)-v(0,t)}{L}$. Using the expression for $v(y,t)$ we get

$$\epsilon_{22}(t) = -\frac{C_{12}}{C_{11}}\frac{tan(kl/2)}{kl/2}\epsilon_{11}(t). \tag{4.34}$$

The value of ϵ_{22} will be used to compute dissipation for structures with free surfaces.

We consider a structure with a dimension of $10lc \times 8lc \times 10lc$ and with free surfaces along the y direction. Here, lc is the lattice constant and has a value of $3.5322\,\mathring{A}$ for nickel. The strain field is a bi-axial strain field given as $\epsilon_{ij}(t) = (\delta_{i1}\delta_{j1}\epsilon_{11} + \delta_{i2}\delta_{j2}\epsilon_{22})sin(\omega_f t)$. Here, ϵ_{22} is related to ϵ_{11} using Eq.(4.34). Figure 4.4(a) shows the plot of the ratio $\epsilon_{22}/\epsilon_{11}$ as a function of ω_f for this structure. The plot shows, that, the ratio increases with the increase in ω_f. The values are in good agreement with MD. We, shall, now use these strain values to compute dissipation using the multi-scale method.

For performing the multi-scale analysis for this structure, different parameters are determined. The value of τ_{relax} is estimated to be 1.45 ps. The strain field is plugged in the constitutive relation in Eq.(4.9) to obtain $\boldsymbol{\sigma}(t)$. E_{disp} is, then, computed using Eq(4.30). Figure 4.4(b) shows the plot of E_{disp} vs. ω_f. A non-monotonic behavior is observed. We also observed a non-monotonic behavior for the bulk structure. However, the frequency value corresponding to the maximum value of E_{disp} shifts to a higher value for the free surface case. This is because the stress relaxation time decreases because of the surface scattering. This, effectively, increases the value of ω_f corresponding to the maximum value of E_{disp}.

We, next, studied the scaling of E_{disp} with size. For this purpose, the length along the free surface (y) direction was varied, the other dimensions were kept constant. For each of the size D_{1111} and D_{1122} were obtained using the non-equilibrium sampling method. Figure 4.5 shows the plot of D_{1111} and D_{1122} as function of size.

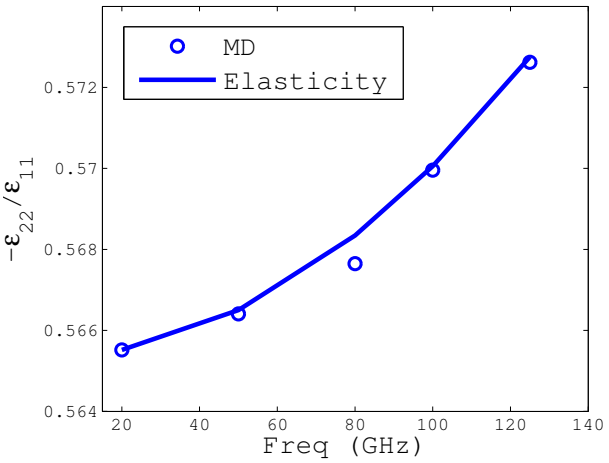

(a)

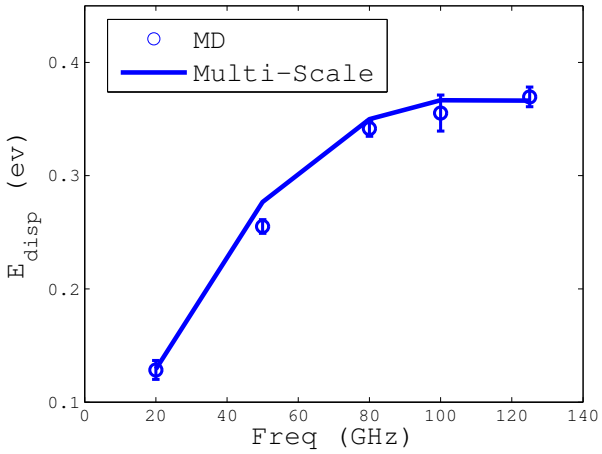

(b)

Figure 4.4: (a)The ratio $-\epsilon_{22}/\epsilon_{11}$ as a function of ω_f for a Ni structure with free surface. The structure has dimensions of $10lc \times 8lc \times 10lc$. Here, lc is the lattice unit. (b) E_{disp} as a function of ω_f for the same structure.

We, then, computed τ_{relax} as a function of size. The τ_{relax} value for a structure with a lateral dimension L is given as

$$\frac{1}{\tau_{relax}} = \frac{1}{\tau_b} + \frac{L_0}{L\tau_s}. \tag{4.35}$$

Here, τ_b is stress relaxation rate for the bulk structure and τ_s is the surface scattering rate for reference structure with a lateral dimension L_0. τ_b was obtained for the case of bulk structure. We, also, determined τ_{relax} for a structure with free surface using the mode Langevin dynamics. The value of τ_{relax} is used to parametrize τ_s. We, then, use Eq.(4.35) to determine τ_{relax} for a structure with any given lateral dimension L.

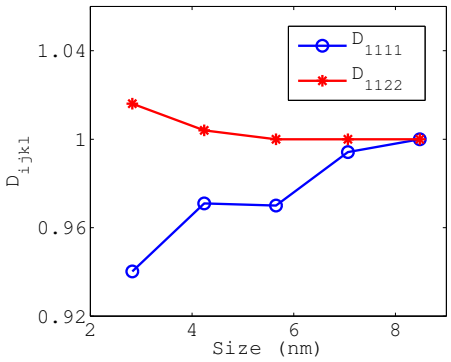

Figure 4.5: The components of the dissipation tensor, **D**, as a function of size. The values have been normalized with respect to the bulk value.

The different parameters, thus, obtained are used to compute E_{disp} as a function of size. Figure 4.6 shows the plot E_{disp} as a function of L and as obtained using the multi-scale theory. The MD values are also plotted alongside. The plot shows that E_{disp} decreases with the decrease in size. This can be understood, predominantly, from the effect of surface on τ_{relax}. The surface scattering of phonon reduces τ_{relax}. The faster relaxation of the non-equilibrium stress implies weaker deviation from the equilibrium condition. Dissipation is governed by the deviation from the equilibrium path. Hence, E_{disp}, decreases with the decrease in τ_{relax}.

4.4 Conclusions

A multi-scale approach to model intrinsic dissipation under high frequency vibrations in solid was developed. A non-equilibrium stress, that characterizes the deviation of the phonon distribution from the equilibrium state, was obtained. A constitutive Eq. that governs the time evolution of the stress tensor was derived. The different parameters in the model were characterized using the QHM method and a stochastic sampling

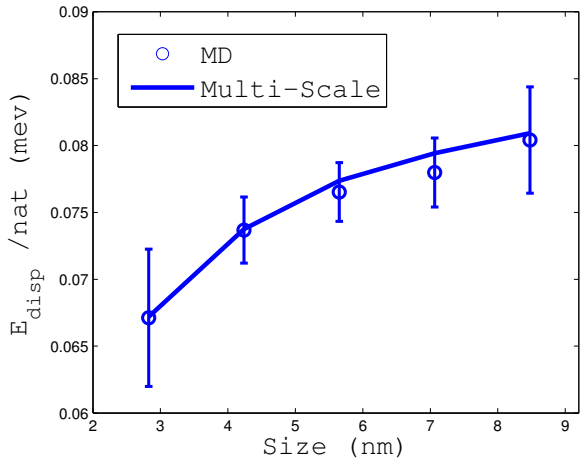

Figure 4.6: E_{disp} as a function of size for structures with free surface. The size denotes the lateral dimension, L, of the structure along the free surface direction. The dimension in the other two (periodic) directions are kept constant.

approach. Langevin dynamics in the mode space was used to obtain the stress relaxation. We studied dissipation in the frequency range of few GHz. Using the proposed formulation, the dissipation rate was computed for different cases. The results were compared with those obtained using non-equilibrium MD.

Chapter 5

Thermo-elastic Dissipation

5.1 Introduction

Thermo-elastic dissipation (TED) takes place in the presence of a non-uniform strain field. The strain field sets up a temperature gradient. This results in heat flow and entropy generation leading to dissipation. Classically, heat flow is described using the Fourier law. Zener derived an expression for the Q factor in a beam considering the Fourier law[78]. The solution for the temperature field was expanded in terms of the eigen-functions of the heat equation. For cases, when the first eigen-mode has the predominant contribution an expression for the Q factor was obtained as

$$Q^{-1} = C\frac{\omega\tau_m}{1+(\omega\tau_m)^2}. \tag{5.1}$$

Here, C is the coupling strength and τ_m is the thermal relaxation time. The theory of TED has been extended and improved for the case of micro-resonators[10, 45]. A more accurate analytical solution of the coupled thermo-elasticity Eq. was obtained in these studies. Also, the case of complicated geometries and higher order modes have been considered[21, 22, 43, 60]. These theories correctly describe the damping for the case of micro-resonators. For such structures, the mean free path is much smaller than the characteristic dimension. Also, the time-scale of the mechanical oscillation is larger in comparison with the phonon relaxation time.

However, for the case of nano-resonators the frequency of vibration becomes comparable to the phonon relaxation time. For such fast oscillations, the finite relaxation time of the heat-flux is expected to play an important role. The ballistic nature of the heat flow, also, becomes important at length scales which are comparable to the phonon mean free path. The classical expression for the TED are, therefore, expected to break down at such length and time-scales. Phenomenological theories, that describe micro/nano-scale heat transfer, have been proposed[47]. These non-classical theories have been used to model TED[19, 67, 71]. These models describe the correct physics under certain cases. However, these theories may fail to capture the essential phonon dynamics under other conditions. The motion of the phonon quasi-particles is analogous to that of dilute gases and is aptly described using the phonon Boltzmann transport Eq.(BTE)[68].

In this work, we consider the BTE for the heat flow and coupled with the elastic strain field. Using numerical solution for the coupled BTE elasticity frame-work, we investigate TED for the longitudinal modes. Frequencies in the range of few GHz are considered. Deviations from classical theories are observed. We provide corrections to the classical expression for the Q factor. The corrected formula takes into consideration the finite relaxation of the phonons and is derived using BTE. The effect of the ballistic nature of the heat flow on the Q factor is, also, discussed.

5.2 Theory

We consider the BTE in terms of the mode energies. Dissipation involves the transfer of energy from the elastic field to the thermal motion. Recasting BTE in terms of the energy variables, thus, offers a practical advantage to study dissipation. We, also, use the gray approximation. The approximation reduces the computational cost considerably. The essential physics is, however, retained for most of the cases. Also, the simplified form of BTE is more amenable to analytical investigation. Under the gray approximation, the phonon dynamics is described in terms of the energy density averaged over the frequency space. Figure 5.1 shows the set-up for phonon dynamics under an oscillating displacement field. For the one dimensional case, the BTE for the phonon transport is given in terms of the energy density, $E(x,\theta,t)$, as

$$\frac{\partial E(x,\theta,t)}{\partial t} + v_g cos(\theta)\frac{\partial E(x,\theta,t)}{\partial x} = -\frac{E(x,\theta,t) - E_{eqb}(x,\theta,t)}{\tau}. \tag{5.2}$$

Here, $E(x,\theta,t)$ is the mean energy density of the phonons with wave vector $\vec{k}$ inclined at an angle θ with the x axis. Further, v_g is the group velocity, E_{eqb} is the equilibrium value of the energy density and τ is the phonon relaxation time. Introducing a variable μ such that $\mu = cos(\theta)$ the above Eq. can be written as

$$\frac{\partial E(x,\mu,t)}{\partial t} + v_g \mu \frac{\partial E(x,\mu,t)}{\partial x} = -\frac{E(x,\mu,t) - \overline{E}(x,t)}{\tau}. \tag{5.3}$$

Here, $\overline{E}$ is the mean energy and is given as $\overline{E} = \frac{1}{2}\int_{-1}^{1} E(\mu)d\mu$. We consider the case of the phonon sub-system coupled with an elastic strain field, $\epsilon(x,t)$. The coupling results in the change of the thermal energy density of each mode and is characterized in terms of a material Grüneisen parameter, λ. For the case of TED, the λ value is taken to isotropic. The Eq. for the phonon dynamics is, then, obtained as

$$\frac{\partial E(x,\mu,t)}{\partial t} + v_g \mu \frac{\partial E(x,\mu,t)}{\partial x} = -\frac{E(x,\mu,t) - \overline{E}(x,t)}{\tau} + \lambda \dot{\epsilon}(x,t) E(x,\mu,t). \tag{5.4}$$

We consider the time evolution of the above Eq. under an oscillating strain field. Due to dissipation, and

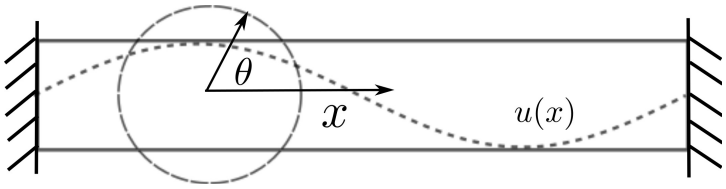

Figure 5.1: A schematic illustrating the phonon dynamics under an oscillating strain field.

in the presence of adiabatic boundaries, the energy of the phonons will increase with time. The dissipation rate is, then, estimated from the rate of increase of the thermal energy. Let E_{tot} represent the total energy of the phonon and is given as

$$E_{tot}(t) = \int_0^L \int_{-1}^1 E(x, \mu, t) d\mu dx. \tag{5.5}$$

Here, L is the length of the structure. The average value of E_{tot} shows a nearly linear increase with time. The dissipation rate, E_{disp}, per unit-period is, then, computed as

$$E_{disp} = < E_{tot} >_{(n+1)\tau_p} - < E_{tot} >_{n\tau_p} . \tag{5.6}$$

Here, $<>_{n\tau_p}$ refers to the average value of E_{tot} for the nth period and τ_p is the time-period of the oscillating strain field. The maximum elastic energy stored, E_{stored}, in the structure is obtained as

$$E_{stored} = \int_0^L \frac{1}{2} E_{mod} \epsilon_0^2(x) A dx. \tag{5.7}$$

Here, E_{mod} is the Young's modulus, $\epsilon_0(x)$ is the strain amplitude, A is the cross-sectional area and L is the length. The Q factor is, then, estimated as $Q = 2\pi \frac{E_{stored}}{E_{disp}}$.

Eq.(5.4) was evolved in time. The unknowns in the coupled elastic BTE are the displacement field, $u(x,t)$, and the phonon energy density $E(x,t)$. The BTE, in essence, is an Eq. that describes the energy conservation. The closure to Eq.(5.4) is provided by the momentum balance Eq. and is obtained using the elasticity theory. The two Eqs. need to be solved consistently. However, we shall follow an alternative approach here. For the under-damped case, one can obtain the displacement field without considering the dissipation. The displacement field, thus, obtained is substituted in the energy balance Eq. and is used to compute the dissipation rate. For the cases considered, $Q >> 1$. Hence, the above approximation is valid and is used for our analysis.

We obtain the strain field using the elasticity theory and without considering dissipation. The strain field is, then, used as an input in the coupled BTE. For solving the BTE, finite difference method was employed. Backward difference scheme was used for $\mu > 0$, forward difference scheme was used otherwise.

We considered the case of diffuse boundary such that $E(\mu,0,t) = \overline{E}(0,t)$ and $E(\mu,L,t) = \overline{E}(L,t)$. The diffuse boundary scattering results in an isotropic distribution of the phonons at the boundaries. From the rate of increase of E_{tot} and the elastic energy stored, E_{stord}, the Q factor was estimated as $Q = \frac{2\pi E_{stored}}{E_{disp}}$.

We, next, seek to obtain a closed from expression for the Q factor for the case of the longitudinal modes. For this purpose we consider an approximate solution of the coupled elastic BTE. In the results section we shall illustrate the condition under which the approximation is valid.

The unknowns in the coupled elastic BTE are the displacement filed, $u(x,t)$ and the phonon energy density $E(x,t)$ For computing the displacement field we, first consider the solution of the momentum balance eqn. The strain field, obtained, is taken as an input in the coupled elasticity BTE frame-work. Such an approximation holds good for an under-damped vibration. This, indeed, is true for the cases considered. The strain field for the fundamental longitudinal mode, and with clamped boundaries, is given as

$$\epsilon(x,t) = \epsilon_0 cos(\frac{2\pi x}{L}) sin(\omega_f t). \tag{5.8}$$

This strain field will be used as an input in Eq.(5.4).

For solving the PDE, we consider a Taylor series expansion for $E(x,\mu,t)$ such that

$$E(x,\mu,t) = E_0(x,t) + \mu E_1(x,t). \tag{5.9}$$

Here, E_0 and E_1 are the expansion variables. Substituting the expression for $E(x,\mu,t)$ in Eq.(5.4), we obtain

$$\dot{E}_0(x,t) + \mu\dot{E}_1(x,t) + v_g\mu(E_0'(x,t) + \mu E_1'(x,t)) = -\frac{E_1(x,t)\mu}{\tau} + \lambda\dot{\epsilon}(x,t)(E_0(x,t) + E_1(x,t)\mu). \tag{5.10}$$

Here, $'$ denotes partial derivative with respect to space. Integrating the L.H.S and R.H.S of the above Eq. with respect to $d\mu$ gives

$$\dot{E}_0 + \frac{v_g E'}{3} = \lambda\dot{\epsilon}(x,t)E_0(x). \tag{5.11}$$

For obtaining the second eqn. for the time evolution of $E_1(x,t)$ we multiply each side w.r.t μ and then perform the integration. This yields

$$\dot{E}_1 + v_g E_0'(x) + \frac{E_1}{\tau} = \lambda\dot{\epsilon}(x,t)E_1(x). \tag{5.12}$$

We, thus, obtain a coupled PDE for the variables E_0 and E_1. We, further, wish to reduce the PDE into a set of ODEs. For this we express the spatial dependence as $E_0(x,t) = E_0^0(t) + E_0^1(t)cos(\frac{2\pi x}{L})$ and

$E_1(x,t) = E_1^0(t)sin(\frac{2\pi x}{L})$. The expansion is motivated by the spatial nature of the strain field and the boundary conditions. For example, the boundary condition dictates that $E_1(0,t) = E_1(L,t) = 0$. The considered functional form, indeed, satisfies this condition. Using the series solution and the orthogonality of the expansion functions, we obtain ODE for the different expansion terms E_i^j. We get

$$\dot{E}_0^0 = \frac{1}{2}\lambda\epsilon_0\omega_f cos(\omega_f t)E_0^1, \tag{5.13}$$

$$\dot{E}_0^1 + \frac{2\pi v_g}{3L}E_1^1 = \lambda\epsilon_0\omega_f cos(\omega_f t)E_0^0 \tag{5.14}$$

and

$$\dot{E}_1^1 - \frac{2\pi v_g}{L}E_0^1 + \frac{E_1^1}{\tau} = \lambda\epsilon_0\omega_f cos(\omega_f t)E_1^1. \tag{5.15}$$

In the above set of Eqs., the explicit dependence of E_i^j on time is implied.

We, thus, have a set of coupled ODE. These are, further, decoupled using algebra and some approximations. We, then, obtain an Eq. for E_0^1 as

$$\ddot{E}_0^1 + \left(\frac{2\pi v_g}{\sqrt{3}L}\right)^2 E_0^1 + \frac{\dot{E}_0^1}{\tau} = \lambda\epsilon_0 E_0^0\omega_f(\frac{cos(\omega_f t)}{\tau} - \omega_f sin(\omega_f t)). \tag{5.16}$$

The Eq. for E_0^1 resembles that of a damped harmonic oscillator. Consider E_0^0 as a constant in the R.H.S the above Eq. admits an analytical solution as

$$E_0^1(t) = Re(\frac{A}{B}exp(i\omega_f t)). \tag{5.17}$$

Here, A and B are complex numbers given as $A = \lambda\epsilon_0 E_0^0\omega_f(\frac{1}{\tau} + i\omega_f)$ and $B = -(\omega_f^2 + (\frac{2\pi v_g}{\sqrt{3}L})^2) + i\frac{\omega_f}{\tau}$. The expression of $E_0^1(t)$ is used to compute the energy dissipated per unit period. E_{disp} is obtained as

$$E_{disp} = E_0^0 L\pi\lambda^2\epsilon_0^2\frac{1+(\omega\tau_m)^2}{(1-\omega^2\tau\tau_m)^2+(\omega\tau_m)^2}\frac{\omega\tau_m}{1+(\omega\tau_m)^2}. \tag{5.18}$$

Here, τ_m is the relaxation time for temperature field and is given as $\tau_m = \left(\frac{L}{v_g^2\tau_{hf}2n\pi}\right)^2$. E_0^0 is thermal energy density per unit length per unit value of μ and is obtained as $E_0^0 = \frac{3k_bT\rho}{2m_{at}}$. ρ is the mass per unit length and m_{at} is the atomic mass. Using the expression for E_{stored} and E_{disp} the Q factor is derived as

$$Q^{-1} = \frac{C_v T_0\lambda^2}{E_{mod}}\frac{1+(\omega\tau_m)^2}{(1-\omega^2\tau\tau_m)^2+(\omega\tau_m)^2}\frac{\omega\tau_m}{1+(\omega\tau_m)^2}. \tag{5.19}$$

Here, C_v is the specific heat capacity per unit volume and T_0 is the reference temperature. We recognize that the classical expression for Q factor is given as $Q^{-1}_{classcl} = \frac{C_v T_0 \lambda^2}{E_{mod}} \frac{\omega\tau_m}{1+(\omega\tau_m)^2}$. The derived expression for Q can, thus, be re-casted as

$$Q^{-1} = \frac{1+(\omega\tau_m)^2}{(1-\omega^2\tau\tau_m)^2+(\omega\tau_m)^2} Q^{-1}{}_{\cdot classcl}. \tag{5.20}$$

The prefactor provides a correction for the classical expression and becomes important for high frequency values. We will use this expression to compare the Q factor obtained using the coupled BTE.

5.3 Results and Discussion

We, first, study the effect of frequency on the Q factor. The phonon relaxation time is of the order of few ps for most materials. The finite relaxation time of the phonons is expected to become important in the frequency range of few GHz. We consider the case of nickel crystal and with the longitudinal direction along the [1 0 0] direction. For the BTE in the gray approximation, we need to provide a single value of the relaxation time. We take $\tau = 1.2$ ps and $v_g = 30\,\mathring{A}\,ps^{-1}$. The average Grüneisen parameter is estimated to be 1.00 and the elastic constant $E_{mod} = 200$ GPa.

For the fundamental longitudinal mode, the angular frequency ω_f is given as

$$\omega_f = \frac{2\pi}{L}\sqrt{\frac{C_{11}}{\rho}}. \tag{5.21}$$

Here, ρ is the density. In-order to study the effect of ω_f we consider structures with different values of L. For a given L, ω_f is estimated using the above eqn. The oscillating strain field is, then, used an input in the BTE. The Q factor is determined using the method discussed. Figure 5.2 shows the plot of Q factor vs ω_f. The other parameters were kept constant for this study. The plot, also, shows the Q factor obtained using Eq.(5.20) and the prediction from the classical theory. The results show that the classical prediction deviates with the increase in the frequency. The corrected formula, however, takes the finite relaxation effect into consideration and is in good agreement with the BTE result.

It would, also, be useful to comment on the Knudsen number, Λ, for this analysis. The Λ value for the structure with the smallest dimension (or highest frequency) considered is estimated to be 0.1. Deviation from the classical theory is observed for even a small value of $\Lambda = 0.1$. This results, predominantly, from the high frequency of oscillation in these structures.

We, next, study the effect of Λ value on the Q factor and keeping ω_f constant. The Λ value can be

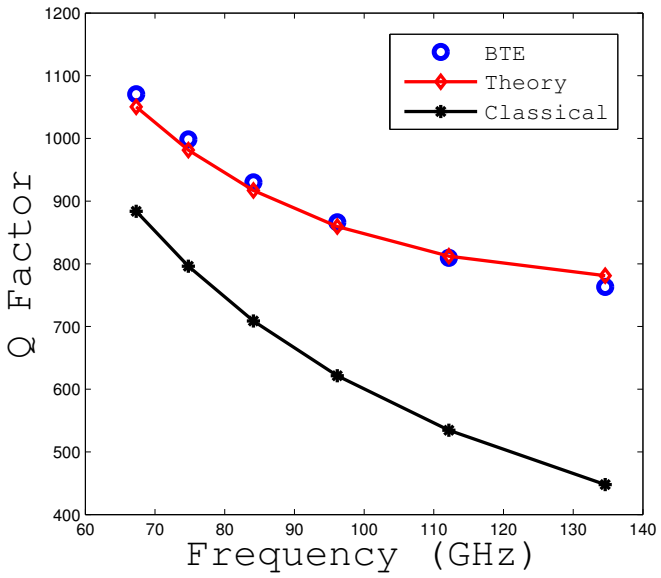

Figure 5.2: Q factor for the longitudinal modes as a function of the oscillation frequency.

changed by changing different parameters. For a structure with a given dimension L, the mean free path, γ is given as $\gamma = \frac{v_g \tau}{L}$. We consider varying the phonon relaxation rate τ. For a given structure, τ can be easily tuned by changing its temperature. v_g, however, has a weak temperature dependence and is difficult to vary.

We consider different values of τ and keeping the other parameter constant. The dissipation rate and the Q factor is estimated for each of the cases. Figure 5.3 shows the variation of Q with Λ and as obtained using the BTE. A non-monotonic dependence is observed. The classical theory fails to predict the observed non-monotonic behavior. Further, the Q factor obtained using the classical formula is lower in comparison with the simulation results.

In predicting the dissipation using Eq.(5.20) we provide an additional correction in this analysis. With the increase in Λ values, the surface scattering of phonons becomes important. This needs to be accounted for in the expression for the Q factor. The total relaxation rate, τ_T, for the diffuse scattering is given as

$$\frac{1}{\tau_T} = \frac{1}{\tau} + \frac{L}{v_g}. \tag{5.22}$$

For small value of Λ, $\tau_T \approx \tau$. However, with the increase in Λ, τ_T decreases because of the surface scattering. We considered this effect in Eq.(5.20). Figure 5.3 shows the Q factor estimated. The results are in good agreement with those obtained using BTE. The plot, also, shows the results obtained without taking surface scattering into consideration. The predicted Q value is higher for such cases.

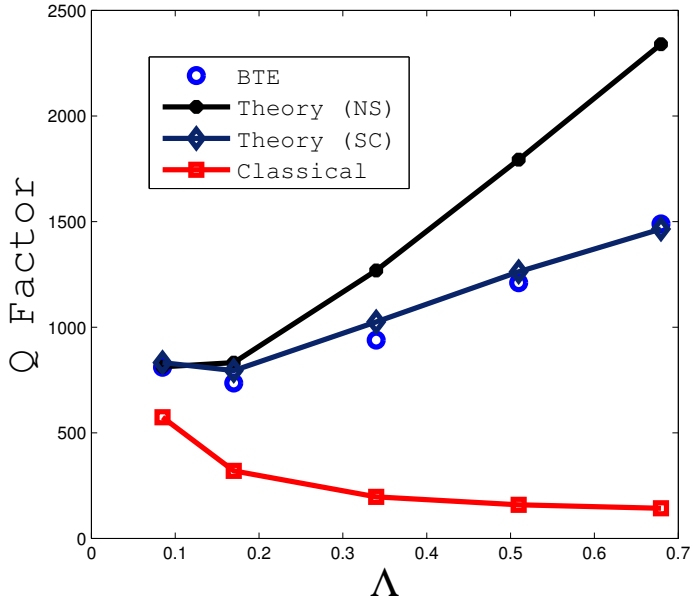

Figure 5.3: Q factor as a function of the Knudsen number, Λ. For varying Λ, the phonon relaxation rate, τ, was changed. All other parameters were kept fixed. NS refers to the case when the surface scattering is not taken into consideration. SC denotes the case when this effect is accounted for.

Before concluding, it would be useful to analyze the spectral distribution of the phonons obtained using BTE. Figure 5.4 shows the phonon energy density as a function of μ and x. We consider two representative regions, the bulk and the surface. The surface region corresponds to the left end of the beam. Figure 5.4(a) shows the spectral distribution for the bulk region. A nearly linear dependence of E with μ is observed. This shows that it is accurate to consider a first order expansion of E in μ. In deriving the analytical expression for Q, we indeed considered a first order expansion in μ. Figure 5.4(b) shows the distribution of E near the surface. For $\mu > 1$, the distribution is nearly flat. A jump is observed at $\mu = 0$. The nature of the phonon energy distribution can be understood from the diffuse surface scattering. The diffuse scattering ensures that the distribution is isotropic at the boundaries. For the right moving phonons, this information is carried along due to the ballistic motion. Hence, we observe a near flat distribution for some region near the boundary. In our theory, this effect was considered by changing the effective relaxation time for the phonons. The discontinuous nature of the distribution at the boundaries may have important implications for the case when λ is not isotropic.

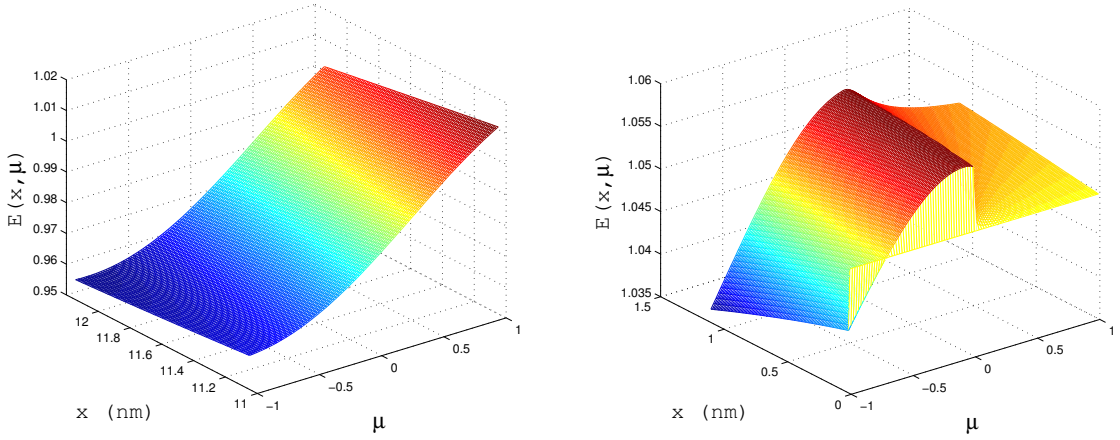

(a) (b)

Figure 5.4: Spectral distribution of energy in an oscillating beam. (a) The distribution for the the bulk region. (b) The distribution near the left end of the beam.

5.4 Conclusions

We used BTE coupled with the elastic strain field to study TED in nano-resonators. We observed that the finite relaxation rate of the heat flux becomes important at high frequency values. We provided correction to the classical expression for Q factor and for the case of longitudinal modes. The surface scattering of phonon plays an important role for high Knudsen number. An effective relaxation time, that takes boundary effects into consideration, was used in the corrected expression for the Q factor.

Chapter 6

Dissipation in Graphene

6.1 Introduction

Intrinsic dissipation involves transfer of energy from the excited mode to internal thermal vibrations or phonons. The inherent non-linearity of the molecular forces couples the different vibrational modes and this leads to an irreversible transfer of energy from the slow mechanical modes to the thermal phonons. The classical mechanisms of intrinsic dissipation, namely the thermo-elastic dissipation, Akhiezer damping and Landau-Rumer coupling, are fundamentally the result of material non-linearity. In the case of nano-systems, nonlinearities can emerge due to the geometric effect [61]. For example, the transverse deformation of a nano-beam is coupled with the stretching motion. These geometric non-linearities therefore introduce new channels for the flow of energy between different vibrational modes and hence may lead to novel mechanisms of dissipation. The relation between damping and the underlying dynamics however remains elusive for most nano-systems. In this work we identify the mechanism of dissipation in graphene under in-plane motion.

Graphene, a one atom thick sheet of carbon atoms, is known for its remarkable thermal, electrical [54] and mechanical properties [41]. It is the limiting case of a nano-electromechanical system in terms of the thickness. Experimental study has demonstrated the use of graphene sheet as a potential nano-resonator [6]. Different studies have been carried out to understand the dissipation mechanism in a graphene resonator [8, 11, 31, 65, 77] under flexure deformation, and the edge atoms were identified to be an important source of dissipation under such mode. While attempts have been made to understand the different dissipation mechanisms operative in the flexure mode, the dynamic behavior of graphene under longitudinal in-plane motion remains largely unexplored. A rich and exciting physics can be expected in the study of attenuation of longitudinal waves in a sheet which is an atomic layer thick. The anharmonic coupling between the bending and stretching mode is known to stabilize a two dimensional membrane [13]. Such a coupling can also lead to an irreversible transfer of energy from one to the other.

In this work[36], using MD simulations, we show that an irreversible transfer of energy indeed takes place from the in-plane longitudinal motion to the out-of-plane vibrations. We identify this to be the dominant

loss mechanism for the in-plane motion under the frequency range studied (20 - 100 GHz). The irreversible energy transfer is shown to take place due to hysteresis behavior in the fundamental out-of-plane mode in the loading direction. The dissipation rate, measured as Q factor, shows a non-monotonic scaling with frequency, becoming maximum at some value. The maximum in the dissipation rate is shown to correspond to a maximum hysteresis in the fundamental out-of-plane mode amplitude. We propose that the hysteresis takes place due to periodic modulation of the potential energy profile for the out-of-plane mode.

6.2 Simulation Details

Graphene was initially relaxed using NPT simulation at 300 K with periodic boundary condition in the in-plane (x-y) directions. We consider two different relaxed configurations which are identified as structure A and structure B. The dimensions of structure A are 96.66 $\mathring{A}$ $\times$100.45 $\mathring{A}$ and dimensions of structure B are 96.66 $\mathring{A}$ $\times$133.87 $\mathring{A}$. The relaxed structures were further equilibrated at 300 K using NVT ensemble for 2 ns. After equilibration, the structure was given a periodic in-plane deformation. Figure 6.1 shows a schematic of the simulation set-up. The in-plane excitation was given by periodically changing the box dimension in the y direction. The length in the y direction, l_{yd}, was varied as $l_{yd} = l_y + asin(\omega t)$. Here l_y is the undeformed length, a is the amplitude of deformation, ω is the angular frequency of excitation and t is the elapsed time. The amplitude of deformation was taken to correspond to a strain amplitude of 0.18% in the y direction. Frequency values in the range of 20 GHz to 100 GHz were considered. For each frequency value 10 different ensembles were taken and for each ensemble 200 oscillation periods were considered for computing the dissipation rate.

During the loading process no thermostating was performed. This implies that $dQ = 0$, where dQ is the differential heat exchanged with the environment. Let dW be the differential work done on the system and dE be the differential increment in its internal energy. From the first law of thermodynamics it then follows that $dW = dE$. For an equilibrium process, net work done during a cyclic deformation is zero. For non-equilibrium process, such as loading at finite rate, net work is done on the system during cyclic loading. The average work done per unit period is a measure of the dissipation rate. For an isolated system, the work done will result in an increase in the internal energy and hence the temperature of the system.

Let ΔW_{avg} be the average work done per unit period and ΔE be the change in internal energy after n periods. From the relation $dW = dE$ it follows that $\Delta E = n\Delta W_{avg}$. Thus, from the rate of increase of internal energy per unit period ΔW_{avg} can be determined. Figure 6.2 shows the plot of average internal energy, E_{avg}, with the number of oscillation periods for one of the ensemble excited at 40 GHz. The plot shows that E_{avg} increases linearly with the number of periods. The slope of E_{avg} vs. the number of period

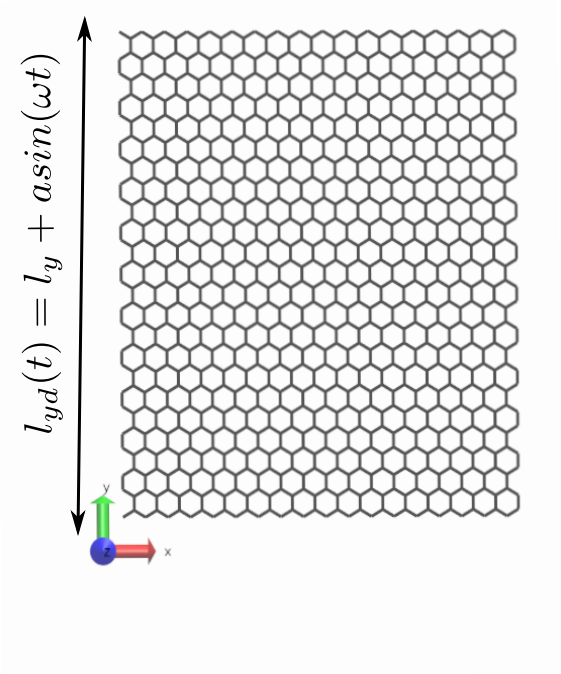

Figure 6.1: A schematic of the simulation set-up to study dissipation in graphene under in-plane motion. Periodic boundary condition is used in x and y direction. The box length in the y direction is changed harmonically with an amplitude a and frequency ω.

of oscillation gives the energy dissipated per unit period, E_{disp}. For forced vibration E_{disp} is a measure of the rate of energy input required to sustain the motion (in our case the in-plane vibration). In the absence of such energy input the motion will die down. Also, E_{disp} corresponds to the rate at which the excited mode looses its energy to other degrees of freedom.

Dissipation is often measured in terms of dimensionless Q factor which is defined as the ratio of maximum elastic energy stored in the structure to the average energy lost per unit oscillation period. It should be pointed out that the energy lost here refers to the loss of energy from the excited deformation (in our case the in-plane motion). The mechanical energy stored, E_{str}, in uni-axial deformation is obtained as $E_{str} = \frac{1}{2}\frac{E}{1-\nu^2}V\epsilon_y^2$. E is the Young's modulus, V is the volume of the structure, ν is the Poisson's ratio and ϵ_y is the strain amplitude. The Q factor is then computed as $Q = 2\pi\frac{E_{str}}{E_{disp}}$. The material properties of graphene, required for computing E_{str}, were taken from previous studies [79].

MD simulations were performed using large-scale atomic/molecular massively parallel simulator(LAMMPS) [59] and adaptive intermolecular reactive empirical bond order (AIREBO) potential [70] was used to model the force field for carbon atoms. A time step of 0.5 fs was used with the velocity Verlet integration scheme. During the equilibration process, the thermostating was performed using Nosé-Hoover thermostat.

Intrinsic dissipation is mediated by the interaction between the different vibrational modes present in

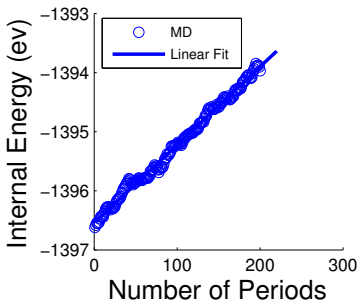

Figure 6.2: The increase in the average internal energy with the number of periods for an ensemble excited at 40 GHz.

a structure. The mechanism of dissipation can be understood by computing the amplitude and velocity for different modes. We have used modal analysis to resolve the dissipation mechanism for graphene under stretching deformation. A section on modal analysis follows. The methodology discussed in this section shall be used in the later section to identify the mechanism of dissipation.

6.3 Modal analysis

The mode amplitude and velocity can be computed by projecting the positions and velocities obtained from molecular dynamics simulations on to the mode shapes. In particular, we are interested in the out-of-plane modes for graphene sheet. In a two dimensional structure, such as graphene, the in-plane motion is strongly coupled to out-of-plane vibrations. We therefore expect the out-of-plane modes to be dominant modes responsible for dissipation under stretching deformation.

The mode shapes, required for computing the modal co-ordinates, can be obtained by different methods. We use the results from continuum theory to compute the out-of-plane mode shapes. Using linearized plate theory the mode shapes, $\phi(\vec{x})$, are obtained as $\phi(\vec{x}) = \vec{P}exp(i\vec{k}.\vec{x})$. $\vec{P}$ is the polarization vector, $\vec{k}$ is the wave vector and $\vec{x}$ is the mean position vector of the atom. For periodic boundary condition in the in-plane directions (x and y) $\vec{k}$ is given as $\vec{k} = \frac{2n\pi}{l_x}\vec{i} + \frac{2m\pi}{l_y}\vec{j}$. Here n, m refers to the mode number and can take positive integral values. l_x and l_y are the length in x and y direction, respectively. We consider the fundamental out-of-plane mode in the y direction ($n = 0, m = 1$) which is identified as mode 1. Mode 1 spatially depends only on the y coordinate. The mode shape, $\phi(y_{mj})$, for mode 1 can be expressed as

$$\phi(y_{mj}) = cos\left(\frac{2\pi y_{mj}}{l_y}\right) + isin\left(\frac{2\pi y_{mj}}{l_y}\right). \tag{6.1}$$

Here y_{mj} is the mean y coordinate of the atom labeled j.

Let z_j and v_{zj} denote the z displacement and velocity for the jth atom. The mode amplitude, A_m, and the mode velocity, V_m, for mode 1 are obtained as

$$A_m = \left| \frac{1}{N_f} \sum_{j=1}^{nat} z_j \phi(y_{mj}) \right| \tag{6.2}$$

and

$$V_m = \left| \frac{1}{N_f} \sum_{j=1}^{nat} v_{zj} \phi(y_{mj}) \right|. \tag{6.3}$$

Here nat is the total number of atoms in the structure and N_f is the normalization factor obtained as

$$N_f = \sum_{j=1}^{nat} \left(cos\left(\frac{2\pi y_{mj}}{ly} \right) \right)^2 = \sum_{j=1}^{nat} \left(sin\left(\frac{2\pi y_{mj}}{ly} \right) \right)^2 = \frac{nat}{2}. \tag{6.4}$$

Let V_r and V_c be defined as

$$V_r = \frac{1}{N_f} \sum_{j=1}^{nat} cos\left(\frac{2\pi y_{mj}}{ly} \right) v_{zj} \tag{6.5}$$

and

$$V_c = \frac{1}{N_f} \sum_{j=1}^{nat} sin\left(\frac{2\pi y_{mj}}{ly} \right) v_{zj}. \tag{6.6}$$

The kinetic energy of an atom j, Ke_j, for mode 1 is given as

$$Ke_j = \frac{1}{2} m \left(V_r cos\left(\frac{2\pi y_{mj}}{ly} \right) + V_c sin\left(\frac{2\pi y_{mj}}{ly} \right) \right)^2, \tag{6.7}$$

where m is the mass of each atom. The total kinetic energy for mode 1, Ke_m, is then obtained as

$$Ke_m = \sum_{j=1}^{nat} Ke_j. \tag{6.8}$$

V_m, V_c and V_r are related as $V_m^2 = V_r^2 + V_c^2$. Using this and the orthogonality properties of the sin and cos functions in eqn(8) we get $Ke_m = \frac{1}{2} nat \times m \frac{V_m^2}{2}$.

6.4 Results and Discussion

We studied the scaling of dissipation rate with frequency for two different graphene structures, A and B. The structures were given a periodic in-plane motion using the method described and the dissipation rate was computed for different frequency values. Figure 6.3(a) shows the plot of Q factor vs. frequency for the

two different structures at 300 K. A non-monotonic trend in the dissipation rate is observed. The Q factor becomes minimum, and hence the dissipation rate maximum, at 80 GHz for structure A and at 60 GHz for structure B. In order to study the thermal effects on the dissipation rate, we computed the Q factor vs frequency dependence at a very low temperature of 0.1 K. The structures with the same bond length, as used for studies at room temperature, were considered for analysis at 0.1 K. This was done to isolate the effect of temperature from strain effects. The inset of fig. 6.3(a) shows the plot of Q factor vs. frequency at 0.1 K. The results show a similar non-monotonic trend as observed for the case of 300 K. The frequency value at which the maximum dissipation occurs, however, shifts to a lower value. The minimum Q factor for both the structures at 0.1 K roughly remains the same as that obtained at room temperature. This shows that the mechanism of dissipation is athermal in origin, and the thermal effects only change the frequency value at which maximum dissipation occurs.

We investigated the role of out-of-plane motion on the dissipation rate using constrained MD simulations. Structure A was equilibrated at 300 K but with the motion constrained in the x-y plane (no out-of-plane motion). This was achieved by setting the out-of-plane component of the force on each atom to be zero. The Q factor vs frequency dependence was then computed using the method discussed before. Figure 6.3(b) shows the plot of Q factor vs. frequency obtained for the case of constrained in-plane motion. An enhancement of Q factor by almost two orders of magnitude is observed in this case. The results point out that the out-of-plane motion is an important medium for extracting energy from the in-plane motion.

We then studied dissipation in graphene subjected to an initial tensile strain. Figure 6.3(b) shows the plot of Q factor vs. frequency obtained for structure A with an initial tension of 1.7% in the x and y direction. The Q factor remains constant with frequency. A drop in the dissipation rate by almost an order of magnitude, in comparison with the case of zero initial strain, is observed. Application of tension to a thin sheet, such as graphene, has the effect of increasing the stiffness of the out-of-plane modes. Large deformation plate theory predicts that the out-of-plane stiffness, k_{stiff}, scales as $k_{stiff} \propto (s + \frac{s^2}{2})$, here s is the in-plane strain. These results indicate that increasing the stiffness of out-of-plane modes has the effect of decreasing the dissipation for the in-plane motion.

6.4.1 Out-of-plane Mode Dynamics

The results of simulations indicate that the out-of-plane modes are an important channel for absorbing energy from the in-plane motion. We therefore study the out-of-plane mode dynamics for graphene structure under in-plane excitation. The MD trajectories for the case of zero initial strain (unless mentioned otherwise) and with no constrain on the out-of-plane motion are considered for this analysis. We only present the results

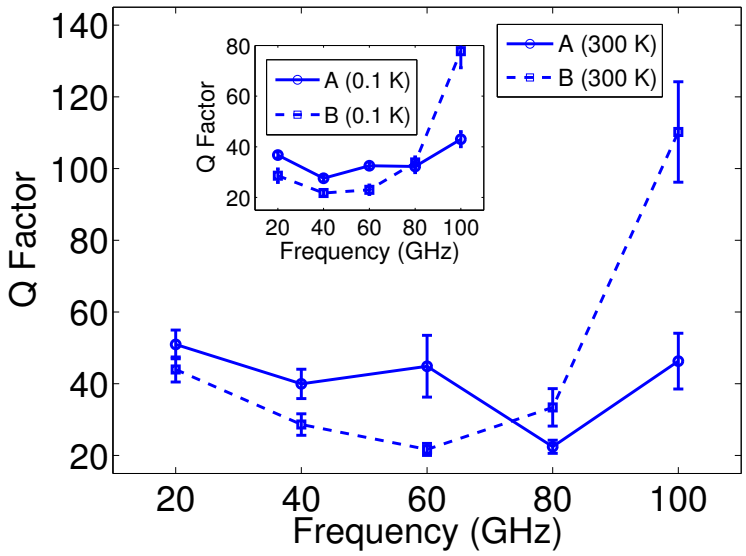

(a)

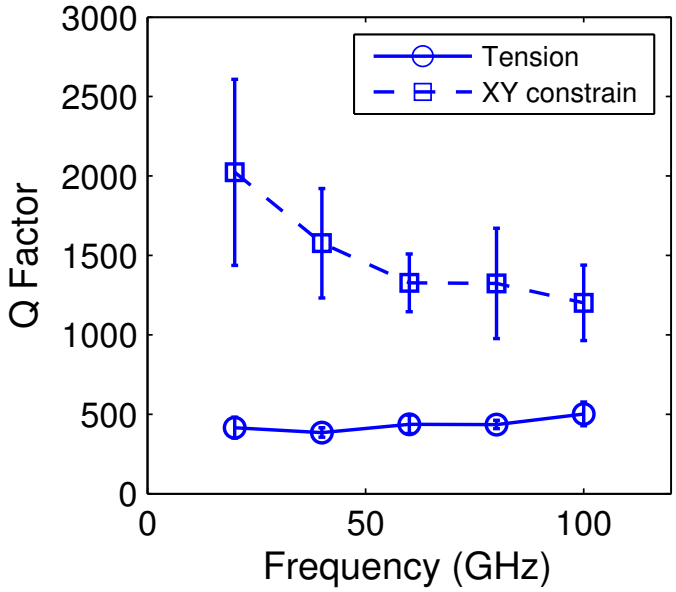

(b)

Figure 6.3: (a) Q factor vs. frequency for structures A and B at 300 K. The inset of the plot shows the Q factor vs. frequency at 0.1 K. (b) Q factor vs. frequency for structure A with an initial tensile strain of 1.7% in x and y direction. Also shown are the results for the case with motion constrained in the x-y plane (no out-of-plane motion).

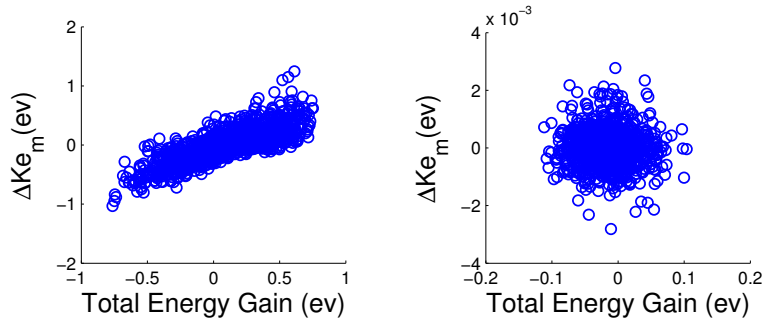

(a) (b)

Figure 6.4: (a) The kinetic energy gained by mode 1 vs. the total energy gained (per unit period) by structure A under in-plane excitation at 80 GHz and at 300 K. (b) The kinetic energy gained by mode 1 vs. the total energy gained (per unit period) by structure A under in-plane excitation at 80 GHz with an initial tensile strain.

obtained from analysis of structure A. For structure B similar results were obtained and are therefore not presented.

Before studying the out-of-plane mode dynamics from MD data, it would be useful to analyze the role of in-plane strain on the out-of-plane modes using continuum theory. The continuum theory has been accurate in predicting dynamical properties, such as vibrational frequency of the out-of-plane modes, for graphene[2]. The potential energy, PE, associated with out-of-plane motion, $w(x,y)$, for a graphene sheet with an in-plane strain, ϵ_y, in the y direction is given as

$$PE = \iint \frac{1}{2} K_b \left(\frac{\partial^2 w}{\partial x^2} + \frac{\partial^2 w}{\partial y^2} \right)^2 dxdy + \iint \frac{Eh}{2(1-\nu^2)} \epsilon_y \left(\left(\frac{\partial w}{\partial y} \right)^2 + \nu \left(\frac{\partial w}{\partial x} \right)^2 \right) dxdy. \tag{6.9}$$

Here K_b is the bending modulus and h is the thickness of graphene sheet. The potential energy expression in eqn(6.9) is a leading order approximation for the total energy. We consider the energy associated with different out-of-plane modes. Let $w_{n,m}(x,y)$ be the out-of-plane displacement for a mode labeled n,m and is given as $w_{n,m}(x,y) = A_{n,m} cos(\frac{2n\pi x}{l_x}) cos(\frac{2m\pi y}{l_y})$. $A_{n,m}$ is the mode displacement for a mode labeled n,m. For such displacement profile the potential energy, $PE_{n,m}$, is obtained as

$$PE_{n,m} = \frac{K_b l_x l_y}{C} A_{n,m}^2 \left(\left(\frac{2m\pi}{l_y} \right)^2 + \left(\frac{2n\pi}{l_x} \right)^2 \right)^2 + \frac{Ehl_x l_y}{C(1-\nu^2)} A_{n,n}^2 \epsilon_y \left(\left(\frac{2m\pi}{l_y} \right)^2 + \nu \left(\frac{2n\pi}{l_x} \right)^2 \right). \tag{6.10}$$

Here C is a constant which has a value of 8 if $n \neq 0, m \neq 0$ and is equal to 4 otherwise. For instability we must

have $\frac{d^2 P_{n,m}}{dA_{n,m}^2} < 0$. This implies that

$$\epsilon_y <= -\frac{K_b\left(\left(\frac{2m\pi}{l_y}\right)^2 + \left(\frac{2n\pi}{l_x}\right)^2\right)^2}{\frac{Eh}{(1-\nu^2)}\left(\left(\frac{2m\pi}{l_y}\right)^2 + \nu\left(\frac{2n\pi}{l_x}\right)^2\right)}. \tag{6.11}$$

Analysis of this expression shows that the minimum negative strain for instability corresponds to $n = 0$ and $m = 1$. This is mode 1 as referred to in the section on modal analysis. We therefore expect mode 1 to be the first mode to become unstable when graphene sheet is given a compressive strain. The potential energy profile for mode 1 (discussed in later section) indeed shows that it becomes unstable. Mode 1 is therefore expected to dominantly govern the dynamics and is the one considered for further analysis.

We computed the kinetic energy gained by mode 1 during each period of oscillation. The difference in the Ke_m values between the beginning and end of each period gives the kinetic energy gained by mode 1, ΔKe_m, during each period of oscillation. The difference in the internal energy between the beginning and end of each period gives total energy gained by the structure, ΔE, during each period of oscillation. Figure 6.4(a) shows the plot of ΔKe_m vs ΔE for structure A under periodic in-plane excitation at 80 GHz. From the plot it is evident that a strong correlation exists between ΔE and ΔKe_m. For positive values of ΔE, ΔKe_m is of similar magnitudes to that of ΔE. This shows that the structure absorbs energy dominantly through mode 1. For zero or negative values of ΔE, ΔKe_m is negative with a larger absolute value as compared to ΔE. These periods of oscillations correspond to the transfer of energy from mode 1 to other vibrational modes in the structure. In the process either total energy of the structure remains constant ($\Delta E = 0$) or is partly transferred back to the forcing medium ($\Delta E < 0$). Mode 1 therefore extracts energy from the in-plane motion and dissipates it into the other vibrational modes. We also computed ΔKe_m vs ΔE for structure A with an initial tension. The result of this analysis is depicted in Fig. 6.4(b). No such correlation between the two quantities is observed. Furthermore, ΔKe_m values are roughly two orders of magnitude smaller than ΔE. This shows that the role of mode 1 in the process of dissipation decreases with the application of tensile strain.

In order to elucidate the role of mode 1 as a channel for energy dissipation, mode 1 amplitude, A_m, values were computed for graphene under in-plane excitation. Because of periodic deformation, A_m is expected to be a function of time. For each period of oscillation, time instances separated by an interval $\Delta t = 5$ fs were considered and A_m values were computed at these instants of time. Let t_{ij} denote the time $j\Delta t$ from the beginning of the ith oscillation period. Let A_{ij} denote the value of A_m at t_{ij} and s_j the in-plain strain value at that instant. A_{ij} was then averaged over a number of oscillation periods to get A_j such that

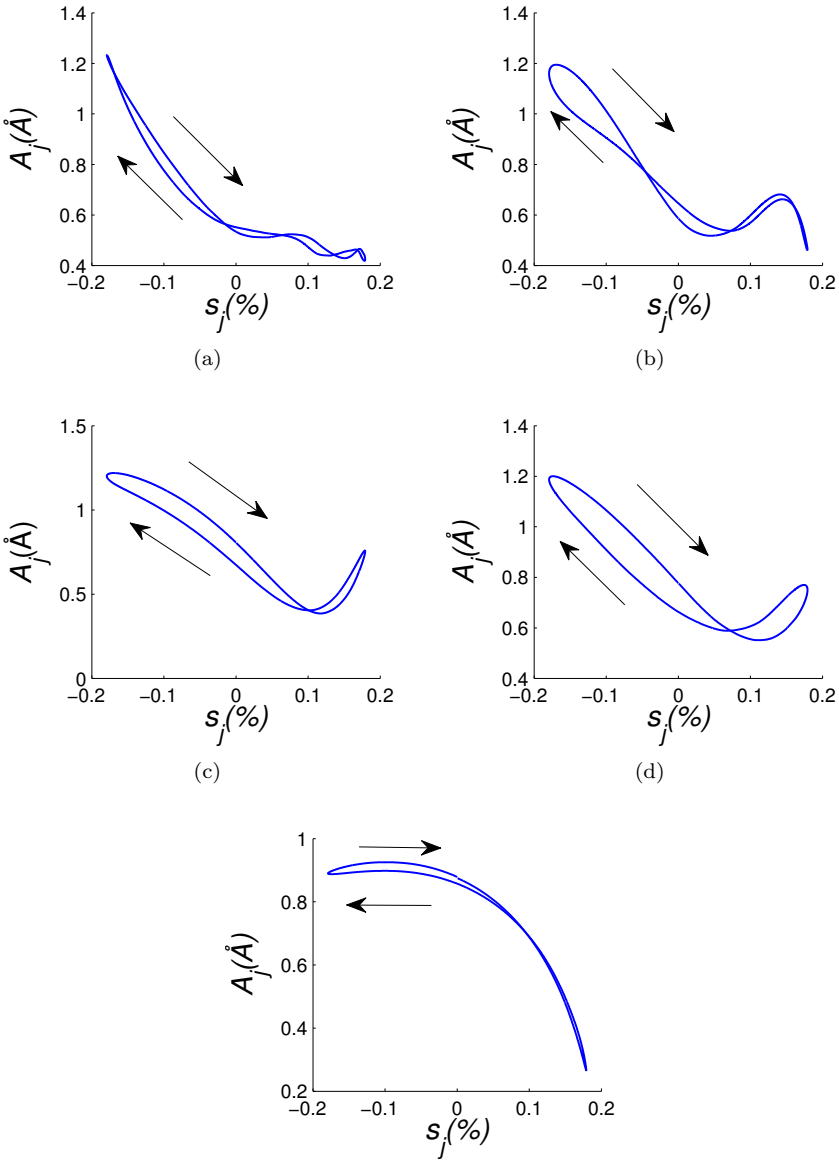

Figure 6.5: (a-e) The response curve for the mean out of plane amplitude (A_j) vs. the in-plane strain (s_j). Plots a, b, c, d and e correspond to the frequency values 20, 40, 60, 80 and 100 GHz, respectively. The arrows in the figure show the loading direction.

$A_j = \frac{1}{nprds} \sum_{i=1}^{nprds} A_{ij}$, here $nprds$ is the total number of oscillation periods. Figure 6.5(a-e) shows the plot of A_j vs. s_j for structure A under in-plane excitation. The plots correspond to different frequency values in the range of 20 to 100 GHz. We see that there is a hysteresis in the response of A_j such that for each value of s_j two different A_j values are obtained.

6.4.2 Dynamic Hysteresis - Analysis

We now ascertain the physical cause for mode 1 hysteresis observed during cyclic in-plane loading. The in-plane strain is an input which results in mode 1 hysteresis. It would therefore be useful to study the potential energy of graphene sheet as a function of these two deformations. Using AIREBO potential, the total potential energy for graphene was obtained as a function of A_m for different in-plane strain values. In order to obtain the potential energy profile for mode 1, the flat sheet was first given an in-plane strain. This was done by scaling the y coordinates corresponding to the strain value, s_j. The atoms were then moved in the z direction such that atom i had a z displacement, z_i, given as

$$z_i = A_m sin\left(\frac{2\pi y_{mi}}{l_j}\right). \tag{6.12}$$

Here l_j is the deformed length in the y direction and is related to s_j as $l_j = l_y(1 + s_j)$. The A_m value was varied from $-3.5\,\mathring{A}$ to $3.5\,\mathring{A}$ with an increment of $3.5{\times}10^{-2}\,\mathring{A}$. For each value of A_m the total potential energy was computed using the AIREBO potential to get $U(A_m, l_j)$. It should be pointed out that the atoms were given the specified motion only for computing the potential energy. This was done separately from the simulations used for computing the dissipation rate, in which case the atoms were free to move in accord with the Newtons law of motion.

Figure 6.6(a) shows the potential energy as a function of A_m for structure A with 0.18% tensile strain and with a compressive strain of 0.18% in the y direction. These values correspond to the strain amplitude used for computing the dissipation rate. Under tensile strain the minimum in the potential energy is at $|A_m| = 0.26\,\mathring{A}$ while under compressive strain the minimum shifts to $|A_m| = 1.428\,\mathring{A}$. Further, the potential energy is maximum at $A_m = 0$ for the compressive case thereby showing that $A_m = 0$ is an unstable point. An out-of-plane deformation corresponding to mode 1 is therefore an unstable one for the flat graphene sheet. If the sheet is perturbed with such a deformation it would not tend to return back to the flat configuration.

The shift in the minimum potential energy point for mode 1 was further validated using equilibrium MD simulation. Structure A was equilibrated at 300 K with initial compressive and tensile strains of 0.18% in the y direction. The A_m values were then computed for the two cases. Figure 6.6(b) shows the probability

density function (pdf) obtained for A_m. Under the tension case the pdf is centered around 0.25 $\mathring{A}$ while for the compressive case it is centered around 1.4 $\mathring{A}$. This shows that the minimum energy point for mode 1 depends on the in-plane strain.

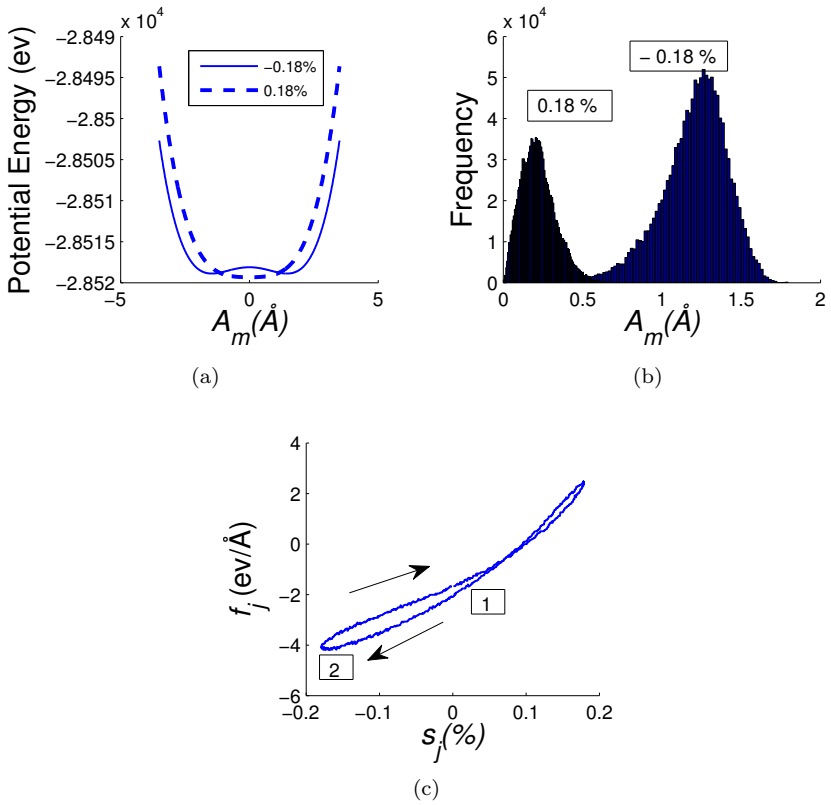

Figure 6.6: (a) The potential energy profile as a function of A_m obtained using AIREBO potential. The results are for structure A under 0.18% compressive and tensile strain in the y direction. (b) The probability density function for A_m obtained using equilibrium MD simulations. The results are for structure A under 0.18% compressive and tensile strain in the y direction. (c) The f_j vs. s_j curve obtained for structure A under periodic excitation at 80 GHz.

A periodic in-plane strain would therefore keep on modulating the position of the minimum potential energy point for mode 1. The structure would require a finite amount of time to relax to the new minimum energy point. This would result in a phase lag between the response (A_j) and the input (s_j). The nature of response curve would depend on the complex potential energy surface traversed by the structure. A simple estimate of the hysteresis time scale can be made by considering the act of quenching the structure A from a tensile strain of 0.18% to a compressive strain of 0.18%. When the structure is quenched from tensile to compressive state, the buckling time is the time required for the structure to move from $A_m = 0.266\,\mathring{A}$ to $A_m = 1.428\,\mathring{A}$. For computing the buckling time, mode 1 dynamics was studied. Dynamics of mode 1 can be described as the motion of a single particle in the potential energy curve $U(A_m, l_j)$. The equation of motion

for mode 1 is given as

$$\frac{nat}{2}\times m\ddot{A}_m = -\frac{\partial U(A_m, l_j)}{\partial A_m}. \tag{6.13}$$

The equation describes the motion for mode 1 assuming other modes to be absent. The initial velocity for mode 1 was taken from the equilibrium distribution in the tensile state. The time required to reach $A_m = 1.428\,\mathring{A}$ was computed for different initial velocity. The mean relaxation time, τ_r, was then determined by taking an average over the initial conditions. τ_r for structure 1 at 300 K was estimated to be 2.42 ps. For dissipation mechanisms due to relaxation, the angular frequency corresponding to maximum dissipation, ω_m, satisfies $\omega_m\tau_d = 1$, where τ_d is the relaxation time specific to the mechanism of dissipation. Assuming similar behavior for the relaxation of mode 1, the frequency for maximum dissipation, f_m, is obtained as $f_m = \dfrac{1}{2\pi\tau_r} = 65.582$ GHz for structure A. This is smaller than 80 GHz, the frequency value corresponding to the maximum dissipation for structure A at 300 K. A more accurate estimate would require considering the noise and the dissipative forces, which have been neglected in our analysis.

Further, we expect a hysteresis in the response of mode 1 only when the time period of in-plane excitation is comparable to the buckling time. For time periods much larger than the relaxation time no hysteresis in A_m is expected. We validated this by studying the response of mode 1 for structure A with an in-plane loading of time period 2 ns. For such deformation, mode 1 gets ample time to relax to the modulated potential energy curve. The response is then expected to follow the input. Figure 6.7(a) shows the plot of A_m as a function of time for one oscillation period with a time period of 2 ns (frequency of 0.5 GHz). The input strain (scaled) value has also been plotted alongside. During the tensile half of the cycle A_m is negligibly small. This is expected as the minimum energy point for mode 1 during tension is around zero. During the compressive half of the cycle the minimum energy point shifts. A_m becomes large and symmetrically follows the input strain. Thus, no hysteresis in the response is observed for this case. The case for excitation at 80 GHz (time period of 12.50 ps) is then considered for comparative analysis. Figure 6.7(b) shows the plot of A_m vs. time for this case. A lag in the response is observed. A_m reaches a maximum value nearly at the end of the oscillation period for the input strain. The mechanism of dissipation due to out-of-plane hysteresis is therefore important only for time scales comparable to the relaxation time. For excitations with much longer time period other dissipation mechanisms may become dominant.

6.4.3 Dissipation Mechanism

We now explain the mechanism of loss of energy from the in-plane vibration in view of the observed hysteresis in the out-of-plane mode amplitude. The loss of energy from the in-plane motion can be ascertained from the response curve of A_j. We consider the A_j vs s_j curve for the loading of structure A at 80 GHz (fig. 6.5(d))

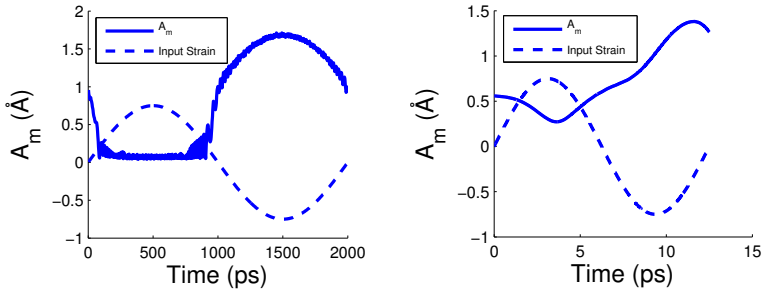

(a) (b)

Figure 6.7: (a-b) The out-of-plane amplitude as a function of time for one oscillation period. Plots a and b correspond to excitation with time periods of 2 ns and 12.5 ps, respectively.

and compute the force, f_j, using the relation $f_j = \dfrac{\partial U(A_j, l_j)}{\partial l_j}$. f_j was computed numerically using a local linear fit of $U(A_m, l_j)$ vs. l_j. The slope of the linear fit gives the value of f_j. The Hamiltonian for mode 1, H is given as $H = U(A_m, l_j) + \dfrac{1}{2} nat \times m \dfrac{V_m^2}{2}$. H is therefore a function of l_j which itself is a function of time. For such time varying Hamiltonian, the differential work done on the system, dW, is given as $dW = \dfrac{\partial H}{\partial l_j} dl_j$. The total work done during a cyclic deformation is then obtained as $W = \oint dW = \oint f_j dl$. A hysteresis in f_j would therefore lead to a net non-zero work on the system.

Figure 6.6(c) shows the plot of f_j vs s_j. The direction of arrows shown in the figure correspond to the loading direction. For the compressive half of the cycle, we see that the magnitude of force required for loading from 1 to 2 is more than that required for unloading from 2 to 1. Thus the effective in-plane stiffness of the structure is higher during loading and decreases during the return path. A similar conclusion can also be drawn using the continuum theory. The stress in the y direction, σ_{yy}, is given as $\sigma_{yy}(\epsilon_y) = \dfrac{1}{V} \dfrac{\partial U}{\partial \epsilon_y}$. Using the continuum expression of potential energy in eqn (6.9) for the out-of-plane motion and elastic energy contribution from the in-plane strain, we obtain

$$\sigma_{yy}(\epsilon_y) = \frac{E}{1-\nu^2}\epsilon_y + \frac{1}{V}\iint \frac{Eh}{2(1-\nu^2)} \left(\left(\frac{\partial w(x,y)}{\partial y} \right)^2 + \nu \left(\frac{\partial w(x,y)}{\partial x} \right)^2 \right) dxdy. \tag{6.14}$$

Further, assuming that the out-of-plane deformation is dominantly described by mode 1, we get

$$\sigma_{yy}(\epsilon_y) = \frac{E}{1-\nu^2}\epsilon_y + \frac{E\pi^2 A_m^2}{(1-\nu^2) l_y^2}. \tag{6.15}$$

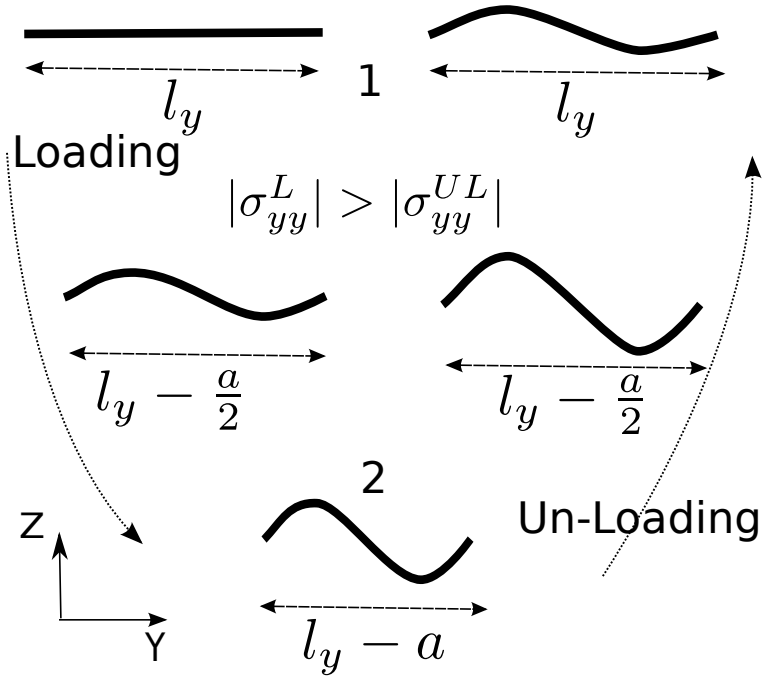

Figure 6.8: A schematic summarizing the dissipation mechanism. The schematic shows a side view of graphene sheet which is given a deformation in the y direction. The compressive half of the cycle has been illustrated here. The structure is loaded from state 1 to state 2 and then un-loaded back to state 1. For the same value of in-plane strain (identified by the length in the y direction) we see that the out-of-plane amplitude is higher during un-loading. The effective in-plane modulus of a thin sheet is lower for higher value of out-of-plane amplitude. The magnitude of in-plane stress during loading, $|\sigma^L_{yy}|$, is therefore higher than the un-loading value, $|\sigma^{UL}_{yy}|$. As a result the structure absorbs energy and heats up.

We define an effective modulus, E_{eff}, as $E_{eff} = \frac{\sigma_{yy}(\epsilon_y)}{\epsilon_y}$. Using eqn(15) we get

$$E_{eff} = \frac{E}{1-\nu^2} + \frac{E\pi^2 A_m^2}{\epsilon_y(1-\nu^2)l_y^2}. \tag{6.16}$$

For negative values of ϵ_y, eqn(6.16) shows that higher is the value of A_m lower is the value of E_{eff}. The higher value of A_m during the return path shows that the effective modulus decreases during the return path.

The elastic softening during the return path would mean that the energy stored during loading is not released completely during unloading. This would result in a loss of energy from the in-plane motion. The schematic illustrated in Fig. 6.8 summarizes the mechanism of dissipation. We expect the loss to be maximum when the difference in the stiffness (and hence A_m) between the forward and the return path is maximum. From Fig. 6.5(a-e) we can see that the difference in the A_m values, between the loading and unloading path during compression, becomes maximum at 80 GHz. The Q factor therefore becomes minimum at this frequency value.

The weak dependence of Q factor on temperature observed for the case of in-plane vibration can also be understood from this mechanism. The minimum potential energy point for the out-of-plane mode depends on the in-plane strain. The periodic in-plane strain would result in similar modulation of potential energy profile for mode 1 at low temperature (for low temperature study the same lattice constant as that of room temperature was considered). The out-of-plane mode hysteresis is, therefore, observed even at low temperature. The dissipation rate depends on this hysteresis behavior. Hence, the observed Q factor shows a weak dependence on temperature. This is in contrast with phonon mediated damping which involves the high frequency thermal phonons. The energy absorbed by thermal phonons depends on the phonon occupation number. The phonon occupation number is given by the Bose-Einstein statistics and is a strong function of temperature. Hence, for phonon mediated damping the Q factor strongly depends on temperature. We expect this to be the case for the flexure mode. As reported in the previous studies [8, 31, 77], for the flexure mode the inverse Q factor shows a T^n dependence where n is in the range of $0.3 - 3$.

Chapter 7

Dissipation in a Nanoribbon

7.1 Introduction

A one-dimensional structure is the limiting case of a nano-resonator and is expected to be an ideal choice for various applications. However, reduced dimensionality may introduce additional mechanisms of dissipation and degrade its performance. An understanding of damping mechanism in one-dimensional structures is therefore of great importance to realize the limiting performance of nano-resonators. With this motivation in mind, in this work, we study the damping mechanism in graphene nanoribbon(GNR), a quasi one-dimensional structure. The high in-plane stiffness [79] of this graphene based structure makes it an ideal choice for string resonator.

In this work[37], we have studied the intrinsic dissipation in GNR under stretching deformation. The case of stretching deformation was considered to generate a nearly homogeneous strain field. This reduces the complexity associated with a spatially varying strain field and helps in better analyzing the dissipation mechanism. Also, it has been shown that it is advantageous to use longitudinal vibration mode for NEMS operating in viscous environment[75] because of relatively lower fluid damping in comparison with the flexural mode. Understanding the internal dynamics of longitudinal mode is important for these applications.

Using MD simulation, we first study the frequency scaling of Q factor. In-order to understand the observed scaling, we investigate the coupling between the out-of-plane modes and in-plane stretching. A Langevin dynamics framework is developed to describe the motion of out-of-plane modes under in-plane stretching. Using this formulation we compute the dissipation rate associated with different out-of-plane modes. From this analysis, we identify two group of modes which show opposite scaling of dissipation rate with frequency. A novel bi-relaxation time model is developed from this analysis. The characteristic relaxation times for the model are obtained from the mean relaxation time of the two mode groups. The two time scales associated with phonon damping is a characteristic feature of this structure. For a regular three dimensional crystalline solid under uniform strain, dissipation is governed by a single relaxation time.

We then studied the size scaling of Q factor. The observed drop in Q factor with decrease in size

is explained to be the result of elastic softening of GNR. The temperature variation of Q factor shows, approximately, an inverse temperature dependence.

7.2 Simulation Method

We utilize classical MD simulation to study the loss mechanism in GNR. Figure 7.1 shows a schematic of the simulation set-up. The edges of GNR have been terminated with hydrogen atoms. This was done to prevent the warping and buckling of the structure. The structure was given an initial tensile strain of about 1.4% for similar reason. Rebo potential [5] was used to model the force field for carbon as well as hydrogen atoms. MD simulations were performed using large-scale atomic/molecular massively parallel simulator (LAMMPS)[59].

GNR was first equilibrated using Nosé-Hoover thermostat at desired temperature with both ends fixed. Subsequent to equilibration, one of the ends was given a displacement controlled periodic motion in the in-plane (x) direction. The amplitude of oscillation was taken to correspond to a strain amplitude of approximately 1%. Frequency values in the range of 5 to 80 GHz were considered. During loading process the thermostat was switched off, thus, there was no heat exchanged with the environment.

From the first law of thermodynamics it follows that $dU = dW$, where dU is the differential increase in internal energy and dW is the differential work done on the system. For a reversible process (quasi-static), the average work done during a cyclic deformation is zero. However, deformations at any finite rate drive the system out of equilibrium. For such cases, energy is dissipated and the average work done during each deformation cycle is positive. The average positive work is guaranteed from the second law of thermodynamics. The dissipative work done will result in an increase in internal energy of the system (if the system is not thermally coupled with the environment). From the rate of increase of internal energy the average work done per unit period, W_{avg}, can be inferred. W_{avg} is a measure of the dissipation rate.

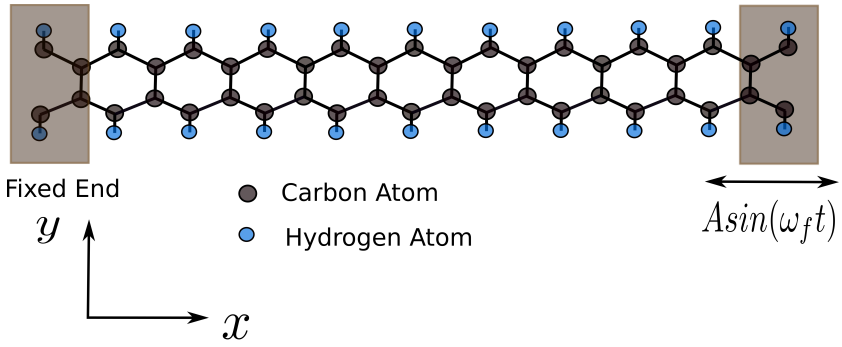

Figure 7.1: A schematic of the simulation set-up.

Dissipation is measured in terms of the dimensionless Q factor which is defined as $Q = 2\pi \frac{E_{stored}}{E_{disp}}$. E_{disp}

is the energy dissipated per unit period and is equal to W_{avg}. E_{stored} is the maximum elastic energy stored in the structure. Under uni-axial loading the maximum elastic energy stored is given as

$$E_{stored} = \frac{1}{2}kA^2 + P_0A. \tag{7.1}$$

k is effective stiffness of the structure, A is amplitude of motion and P_0 is tensile force in the reference configuration.

Independent equilibrium simulations were performed to compute k and P_0 for GNR. With one end fixed the other end of GNR was given an incremental displacement of 0.1 $\mathring{A}$. After an incremental displacement, the ends were held fixed and the structure was equilibrated for a time period of 1 ns. For the next time span of 1 ns the average force on the end atoms was computed. 8 incremental displacements were given to the structure. Thus, we obtain a force displacement curve. The slope of the curve gives k while the intercept provides the value of P_0. The values of k and P_0 for GNR with different width are provided in Table I.

Table 7.1: The values of k and P_0 for GNR

Width (nm)	$k\left(\frac{\text{ev}}{\mathring{\text{A}}^2}\right)$	$P_0\left(\frac{\text{ev}}{\mathring{\text{A}}}\right)$
0.68	0.748	1.575
1.11	1.531	3.206
1.54	2.303	4.849
1.96	3.141	6.513
2.38	3.911	8.172
2.81	4.701	9.861
3.67	6.290	13.256

7.3 Results and Discussion

7.3.1 Frequency Scaling

We first studied the scaling of Q factor with frequency for a GNR with length 10 nm and width 0.68 nm. Periodic motion with forcing frequency, ω_f, values in the range of 5 to 80 GHz were considered. The value of A was taken to be 1 $\mathring{\text{A}}$ for all the frequencies. For each frequency value 10 different equilibrated ensembles were taken. The rate of increase of internal energy was computed by monitoring the average internal energy over 200 oscillation periods for each of the ensemble. Q factor was then computed using the method described before. Figure 7.2 shows the variation of Q factor with frequency obtained from MD. A non-monotonic dependence of Q factor on frequency is observed. The Q factor attains a maximum value at around 40 GHz, hence, dissipation becomes minimum at this frequency value. The plot also shows the Q factor obtained

using the bi-relaxation time model discussed later. In order to understand the observed scaling of Q factor with frequency, we now analyze the dissipation mechanism. From the analysis the bi-relaxation time model follows.

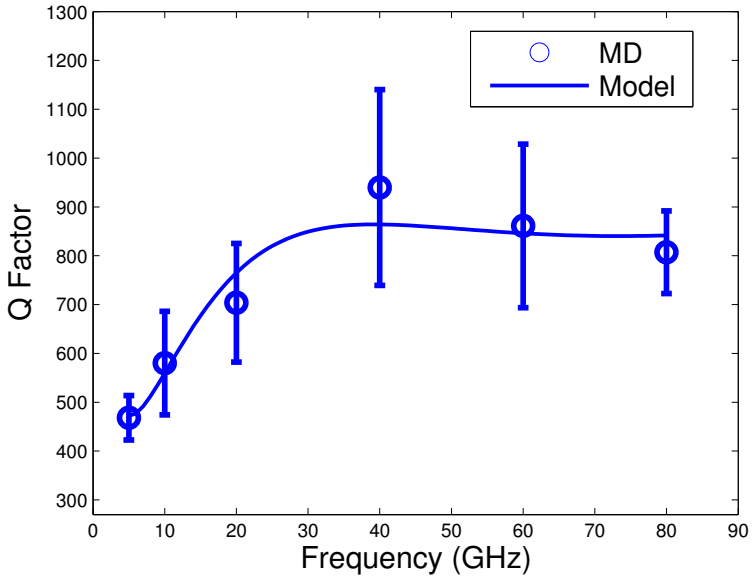

Figure 7.2: Variation of Q factor with frequency for GNR. The open circles correspond to the result obtained from MD simulation. The solid lines are the result obtained using the bi-relaxation time model.

7.3.2 Dissipation Mechanism

The mechanism of dissipation can be understood in terms of the strong coupling that exists between out-of-plane vibrations and in-plane strain for thin structures such as a membrane or a string. For example, the frequency of vibration of a string can be tuned by changing the tension (which results from change in in-plane strain). Dynamic loading in in-plane direction would therefore result in an energy exchange with out-of-plane vibrations. The energy gained by the out-of-plane modes are then irreversibly transformed into thermal energy of the structure. Using continuum theory for strings we first study the coupling between in-plane strain and out-of-plane vibrations. The equation governing the motion of out-of-plane modes for a periodically stretched string is first obtained. The contribution of different modes to dissipation and their scaling with frequency is then estimated.

String Dynamics

We consider a string with bending stiffness K_b and tension P . The string has an out-of-plane deformation $w(x)$. The potential energy, PE, associated with the out-of-plane motion is given as

$$PE = \int_0^L \frac{1}{2} K_b \left(\frac{\partial^2 w}{\partial x^2}\right)^2 dx + \int_0^L \frac{1}{2} P \left(\frac{\partial w}{\partial x}\right)^2 dx. \tag{7.2}$$

L is length of the string. The boundary conditions are $w = 0$ at $x = 0, L$. The nth mode shape, $w_n(x)$, satisfying the given boundary condition is obtained as $w_n(x) = A_n sin\left(\frac{n\pi x}{L}\right)$, where A_n is the amplitude. Let ω_n be the angular frequency for the nth out-of-plane mode. The time dependent displacement, $w_n(x,t)$, associated with nth out-of-plane mode is given as $w_n(x,t) = w_n(x)exp(i\omega_n t)$. Here, we have considered the case of free vibration with no dissipation.

The angular frequency can be estimated by equating the maximum potential energy with the maximum kinetic energy for such case. The maximum kinetic energy, Ke_n, associated with vibration of nth mode is obtained as $Ke_n = \frac{1}{2}\rho A_n^2 \omega_n^2 \frac{L}{2}$. ρ is the mass per unit length. Using eqn(7.2) and the expression for mode shapes, the maximum potential energy, Pe_n, for the nth out-of-plane mode is derived as

$$Pe_n = \frac{1}{2} K_b \left(\frac{n\pi}{L}\right)^4 A_n^2 \frac{L}{2} + \frac{1}{2} P \left(\frac{n\pi}{L}\right)^2 A_n^2 \frac{L}{2}. \tag{7.3}$$

Equating Ke_n and Pe_n, we get

$$\omega_n = \sqrt{\frac{K_b \left(\frac{n\pi}{L}\right)^4 + P \left(\frac{n\pi}{L}\right)^2}{\rho}}. \tag{7.4}$$

ω_n is a thus a function of P which depends on in-plane strain. Let P_0 be the tension and ω_n^0 be the angular frequency for nth mode in undeformed configuration of the string. Using eqn(7.4) we obtain $\omega_n^0 = \sqrt{\frac{K_b \left(\frac{n\pi}{L}\right)^4 + P_0 \left(\frac{n\pi}{L}\right)^2}{\rho}}$. The string is subjected to an in-plane strain, ϵ_s, which changes the tension in the string as $P = P_0 + K_s\epsilon_s$. Here, K_s is the stretching stiffness of the string. This changes the angular frequency as $\omega_n = \sqrt{(\omega_n^0)^2 + \frac{K_s\epsilon_s}{\rho}\left(\frac{n\pi}{L}\right)^2}$. Further, for $\epsilon_s << 1$ this can be approximated as

$$\omega_n = \omega_n^0(1 + \lambda_n \epsilon_s). \tag{7.5}$$

λ_n is a variable given as

$$\lambda_n = \frac{K_s \left(\frac{n\pi}{L}\right)^2}{2P_0 \left(\frac{n\pi}{L}\right)^2 + 2K_b \left(\frac{n\pi}{L}\right)^4}. \tag{7.6}$$

The sensitivity of ω_n on ϵ_s thus depends on λ_n. The dependence of frequency on strain is often measured

in terms of Grüneisen parameter, λ_n^g, defined as $\lambda_n^g = -\frac{dlog(\omega_n(\epsilon_s))}{dlog(vol)}$. Here vol is volume of the structure. It would be useful to derive a correspondence between λ_n and λ_n^g. For uni-axial deformation $vol = vol_0(1+\epsilon_s)$, where vol_0 is the reference volume. For such deformation, we get $\omega_n(\epsilon_s) = \omega_n^0(1+\epsilon_s)^{-\lambda_g^n}$. Further, for $\epsilon_s << 1$ we obtain $\omega_n(\epsilon_s) = \omega_n^0(1-\lambda_g^n\epsilon_s)$. Comparing this with eqn(7.5) we see that λ_n is the negative Grüneisen parameter for the nth out-of-plane mode.

Physically, λ_n^g is a measure of the change in the temperature of nth mode when the structure is loaded under adiabatic condition.This can be understood by considering the case for a harmonic oscillator whose frequency is changed quasi-statically. For such an oscillator, the ratio of energy, E, and frequency, ω_n, is an adiabatic invariant[34]. It then follows that

$$\frac{E^0}{\omega_n^0} = \frac{E^0 + \Delta E}{\omega_n^0(1-\lambda_g^n\epsilon_s)}. \tag{7.7}$$

Here, E^0 is the energy of the oscillator in reference configuration and ΔE is the change in energy of the oscillator resulting from change in frequency (which in-turn results from in-plane strain). Further simplification of eqn(7.7) gives $\Delta E = -E^0\lambda_n^g\epsilon_s$. Thus, modes with high values of λ_n^g, and hence λ_n, will undergo higher change in temperature with the loading of structure. Such modes are therefore driven out-of-equilibrium, for in equilibrium all modes have the same average temperature. These modes will then interact with the rest and tend to relax towards equilibrium. The inter modal interaction results in an irreversible flow of energy. This in essence is the mechanism of dissipation at work.

We now make an estimate of λ_n for different out-of-plane modes using MD and compare it with the continuum theory. In-order to estimate λ_n, out-of-plane mode frequency values were determined for different values of in-plane strain. GNR was given an in-plane strain by scaling the x co-ordinate. The ends of GNR were kept fixed and the structure equilibrated at room temperature (300 K). The out-of-plane(z) co-ordinates were projected on to the mode shapes to get the modal co-ordinates. Let z_i be the z co-ordinate for the ith atom and $natom$ be the total number of atoms in the structure. Let x_i^m be the mean x co-ordinate for the ith atom. The modal co-ordinate, a_n, for the nth mode is then obtained as

$$a_n(t) = \frac{\sum_{i=1}^{natoms} z_i(t) sin\left(\frac{n\pi x_i^m}{L}\right)}{\sum_{i=1}^{natoms}\left(sin\left(\frac{n\pi x_i^m}{L}\right)\right)^2}. \tag{7.8}$$

The auto-correlation of a_n shows a sinusoidal decaying behavior. The fft of the sinusoidal data gives ω_n. An exponential fit of the decaying amplitude gives the relaxation time, τ_n, for the nth mode. ω_n is thus obtained for different in-plane strain. A linear fit between ω_n and in-plane strain gives λ_n in accordance with eqn(7.5).

Figure 7.3(a) shows the plot of λ_n with mode number. A fit using the continuum expression of eqn(7.6), for the parameters K_b and K_s, has also been provided. The plot shows that λ_n decreases with the increase in mode number. This can be understood by considering the ratio, r, of bending energy to stretching energy as a function of n. From the expression of mode potential energy in eqn(7.3), we obtain $r = \frac{K_b \left(\frac{n\pi}{L}\right)^2}{P}$. r increases with n and, hence, for larger n, deformation becomes bending dominated. A bending dominated deformation is relatively less sensitive to in-plane strain. Hence, λ_n decreases with increasing n values.

The analysis shows that the low frequency out-of-plane modes are most strongly coupled to in-plane motion. The energy transfer between such modes and stretching deformation is therefore expected to be higher in-comparison with the high frequency modes. While λ_n gives the coupling strength for the mode, dissipation also depends on another important parameter, τ_n. Figure 7.3(b) shows the plot of τ_n vs n for GNR. For low n values, the modes have higher relaxation time with a wide variation. For higher n values the modes have relaxation time of around 3 ps (see inset of figure 7.3(b)).

τ_n is a measure of how fast the modes relax towards equilibrium. Modes with very low value of τ_n would always be in equilibrium and hence would result in lower dissipation. Modes with very high value of τ_n take considerably longer time to transfer energy to other modes. This corresponds to an adiabatic situation, the energy gained by these modes during loading is reversibly transferred back during un-loading. Such modes also lead to low dissipation. Dissipation is maximum for some intermediate value of τ_n. The high and low referred here are relative terms and depend on the forcing time period. The dissipation associated with each mode is therefore an interplay of coupling strength and relaxation time. In-order to assess the relative modal contribution to dissipation we now develop an equation for the out-of-plane modes of a string subjected to in-plane stretching. The values of ω_n, λ_n and τ_n obtained from this analysis will be used in these equations to estimate the dissipation rate associated with different out-of-plane modes.

Out-of-plane Langevin Dynamics

The equation of motion for the *nth* mode of a string with fixed length and for the case of no dissipation is given as $m_{eff}\ddot{a_n} + m_{eff}\omega_n^2 a_n = 0$. Here, a_n is the modal displacement and m_{eff} is the effective mass which is given as $m_{eff} = \frac{\rho L}{2}$. For a string at any finite temperature, the modes are subjected to additional noise and dissipative force. The noise and dissipative force result either from coupling with other internal modes or because of external coupling with the environment. In our formulation, the noise and dissipative force describe the coupling with other internal modes. The equation of motion, taking these forces into consideration, is then given as

$$m_{eff}\ddot{a_n} + m_{eff}\omega_n^2 a_n + c_n\dot{a_n} = \chi_n(t). \tag{7.9}$$

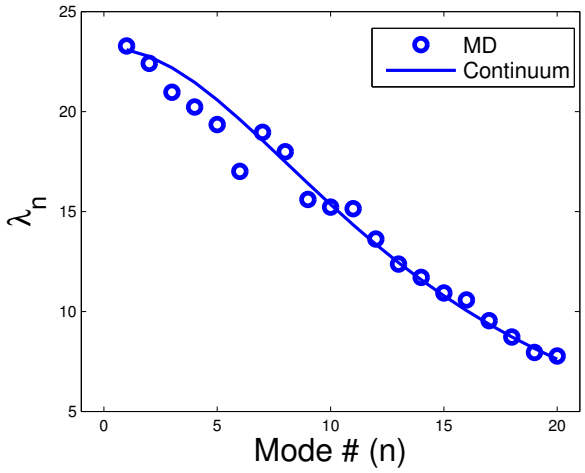

(a)

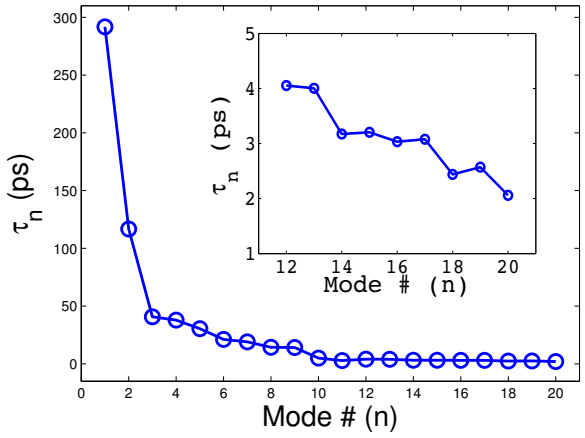

(b)

Figure 7.3: (a) Variation of λ_n with mode number n as obtained using MD simulations. A fit using the continuum relation expressed in eqn(7.6) has also been provided. (b) Variation of τ_n with n. The values correspond to GNR in the reference configuration. The inset shows the relaxation time for modes with high n values.

Here c_n is the damping constant and $\chi_n(t)$ is the noise force. c_n is related to τ_n as $c_n = \frac{2m_{eff}}{\tau_n}$. The relation between c_n and τ_n can be established by considering the solution for a damped harmonic oscillator[15]. $\chi_n(t)$ is a delta correlated white noise with zero mean and satisfies the fluctuation-dissipation theorem[15] as $< \chi_n(t)\chi_n(t_0) >= \frac{\tau_n k_b T}{m_{eff}}\delta(t - t_0)$. T is temperature of the system and k_b is the Boltzmann constant.

We now consider the case when the string is subjected to an in-plane motion with strain amplitude ϵ_0 and forcing frequency ω_f. The in-plane motion will modulate the frequency of out-of-plane modes in accordance with eqn(7.5). Figure 7.4 illustrates the mode dynamics. The equation of motion for the case of parametrically modulated out-of-plane mode is then given as

$$m_{eff}\ddot{a_n} + m_{eff}(\omega_n^o(1 + \lambda_n\epsilon_0 sin(\omega_f t))^2 a_n + c_n\dot{a_n} = \chi_n(t). \tag{7.10}$$

The above equation describes the dynamics of a noisy oscillator under parametric excitation. The continuous excitation of the system ensures that the system is always out of equilibrium. For such a system, useful work extracted from parametric loading will be converted into thermal energy. The dissipation rate can be measured by estimating the average work done per period.

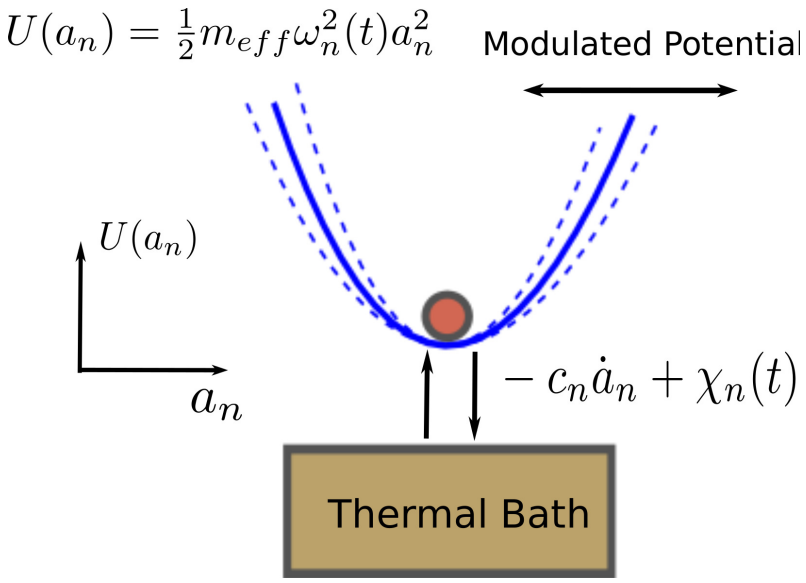

Figure 7.4: A schematic describing the basic ideas of Langevin simulation. A particle is moving in a harmonic potential which is modulated in time. The dotted lines show the potential profile at different time instants. The particle is connected to a thermal bath (which represents the rest of modes). An effective noise and a dissipative force acts on the particle as a result of this interaction.

The in-plane loading modulates the frequency and hence the potential energy of the oscillator. The differential work done is equal to the differential change in potential energy (which results from the change

in frequency). The differential work, dW, done on the oscillator due to loading is then given as

$$dW = \frac{1}{2} m_{eff} d(\omega_n^2) a_n^2. \tag{7.11}$$

Further, using the dependence of ω_n on ϵ_s from eqn(7.5) we get

$$dW = m_{eff} \omega_n \omega_n^0 \lambda_n \epsilon_0 \omega_f cos(\omega_f t) dt. \tag{7.12}$$

The average work done per unit period is a measure of dissipation rate, E^n_{disp}, for the nth mode and is obtained as

$$E^n_{disp} = \left\langle \int_0^{\frac{2\pi}{\omega_f}} m_{eff} \omega_n \omega_n^0 \lambda_n \epsilon_0 \omega_f cos(\omega_f t) dt \right\rangle. \tag{7.13}$$

The average here refers to the ensemble average.

Eqn(7.10) was solved numerically using the velocity Verlet integration scheme. ω_n^0, λ_n and τ_n required as inputs to the equation were estimated from MD simulation (as discussed before). The value of ϵ_0 was taken to be 1%, this corresponds to the strain amplitude used in the forced vibration analysis of MD simulations. The initial condition for eqn(7.10) was obtained by evolving eqn(7.9) for an equilibration time of 320 ps. τ_n is maximum for mode 1 with a value of around 290 ps. An equilibration time of 320 ps therefore ensures that all modes are equilibrated prior to loading. A time step of 0.5 fs was used. 8000 ensembles were taken and for each ensemble 10 oscillation periods were considered for computing E^n_{disp}. Forcing frequency values from 5 to 80 GHz (same as used in MD simulations) were considered.

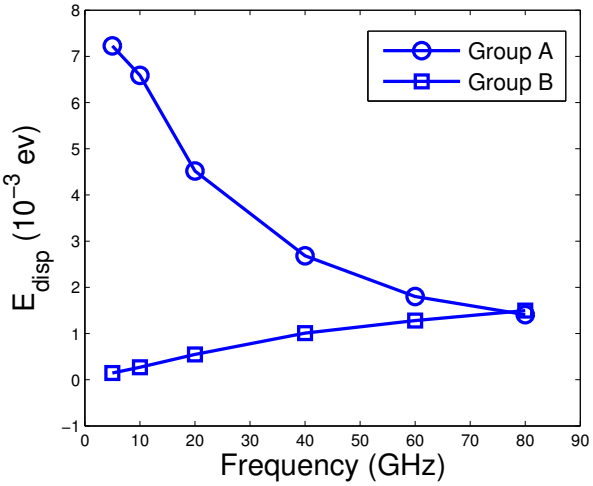

Figure 7.5: Variation of dissipation rate (E_{disp}) with frequency for the two mode groups obtained using Langevin simulations.

Rather than analyzing all the modes, we choose some representative modes for studying the scaling of dissipation rate with forcing frequency. We select 5 modes which have τ_n in the range of 300 - 10 ps and another 5 modes with $\tau_n < 10$ ps. The former set is identified as group A and the latter as group B. The total dissipation due to A and B was then computed for different frequency values in the range of 5 to 80 GHz. Figure 7.5 shows the variation of dissipation rate with frequency for A and B. The plot shows that for set A dissipation rate decreases with the increase in frequency while for B the rate increases with the increase in frequency. Further, the dissipation rate for B is lower in comparison with that of A. The set B comprises of modes with high n value. For such modes λ_n is smaller and hence the dissipation rate for set B is lower.

It would appear from this analysis that group A (for which E_{disp} is higher) would dominate and govern the scaling of Q factor with frequency. However, the number of modes with larger n values (that show set B like behavior) is higher in comparison with the modes with low n values. Though we have computed (see figure 3) λ_n and τ_n for $1 <= n <= 20$, n can take higher values. $\frac{L}{n}$ is a measure of half wavelength associated with a given mode. For a lattice structure, wavelength is bounded below by the dimension of its unit-cell. For GNR considered the unit cell has a dimension of 2.4595 $\mathring{\text{A}}$. This implies that $n \leq 75$. The number of modes which show the characteristics of set B would be higher. The collective behavior of such modes is expected to become comparable to that of group A and govern the dissipation rate in high frequency range.

Bi-relaxation Time Model

From the discussion in the previous section, we note that GNR has two group of modes which show opposite scaling of dissipation rate with frequency. For lower frequency values, group A dominates and hence Q factor increases with the increase in frequency. For higher frequency values, the frequency dependence is governed by the behavior of group B. A non-monotonic dependence of Q factor with frequency is therefore observed. For dissipation governed by relaxation spectra with different time scales, Q factor is given as [68]

$$Q^{-1} = \sum_{i=1}^{m} C_i \frac{\omega_f \tau_i^e}{1 + (\omega_f \tau_i^e)^2}. \tag{7.14}$$

Here C_i is the coupling strength for the given relaxation mechanism, τ_i^e is the corresponding relaxation time and m is the total number of relaxation spectra. It should be pointed out that τ_i^e refers to the time associated with energy relaxation for the given mechanism.

Recognizing that for the case of GNR, dissipation is governed by two mode groups, we consider a bi-relaxation time model. We take τ_1^e as $\tau_1^e =< \frac{\tau_n}{2} >$, where the average is taken over n such that $\tau_n > 10$ ps. The factor of $\frac{1}{2}$ is used because τ_n is a measure of time associated with amplitude relaxation. Energy

relaxation time is one-half of the amplitude relaxation time. Similarly, τ_2^e was determined as τ_2^e as $\tau_2^e =< \frac{\tau_n}{2} >$, where n satisfies the condition that $\tau_n < 10$ ps. Using the relaxation times obtained from MD simulation (figure 3(b)), τ_1^e and τ_2^e were estimated to be 32.57406 ps and 1.61393 ps, respectively. With these values of τ_i^e the Q factor obtained from MD simulations were fitted in accord with eqn(7.14) to obtain C_1 and C_2. Figure 7.2 shows the results obtained from the model and a good agreement with the MD data is observed.

The expression in eqn(7.14) is amenable to further analysis. Taking the derivative of Q^{-1} with respect to ω_f we obtain

$$\frac{dQ^{-1}}{d\omega_f} = \sum_{i=1}^{2} \frac{C_i \tau_i^e (1 - (\omega_f \tau_i^e)^2)}{(1 + (\omega_f \tau_i^e)^2)^2}. \tag{7.15}$$

From the expression we see that for $\omega_f \tau_1^e < 1$ (and hence for $\omega_f \tau_2^e < 1$, since $\tau_2^e < \tau_1^e$), $\frac{dQ^{-1}}{d\omega_f} > 0$. Hence for this region, Q factor decreases with the increase in frequency. For $\omega_f \tau_2^e > 1$ (and hence for $\omega_f \tau_1^e > 1$, since $\tau_1^e > \tau_2^e$), $\frac{dQ^{-1}}{d\omega_f} < 0$. For this regime, Q factor increases with the increase in frequency. We haven't explored these regions using MD simulations. These regions correspond to forcing with frequency value less than 4.88 GHz (for $\omega_f \tau_1^e < 1$) and with frequency value greater than 98.2863 GHz (for $\omega_f \tau_2^e > 1$). The exploration of former case is limited by the computational cost. It would require very long simulation time to capture sufficient number of periods in the low frequency regime. Further, we expect the model to hold good in the low frequency region rather than for high frequency cases. For high frequency case, dissipation mechanism such as the Landau-Rumer coupling will take over. The relaxation time approximation is not adequate to describe such a case. We need to consider a more detailed description of phonon collision to model these cases.

7.3.3 Size Scaling

We next studied the scaling of Q factor with width of GNR. The length of GNR was kept fixed while the width was varied from 0.68 nm to 3.65 nm. The structure was excited with a forcing frequency of 40 GHz. Using the method discussed in the section on simulation details, Q factor was computed for GNR with different sizes. 10 different ensembles were considered for each size and for each ensemble 200 oscillation periods were considered. Independent equilibrium simulations were performed for computing P_0 and k for each size.

Figure 7.6 shows the plot of Q factor vs. size for GNR excited at 40 GHz. The plot shows that Q factor decreases with the decrease in size. This may be attributed to an increase in dissipation with decrease in size. However, Q factor is a ratio of energy stored to energy dissipated per unit period. The decrease in Q

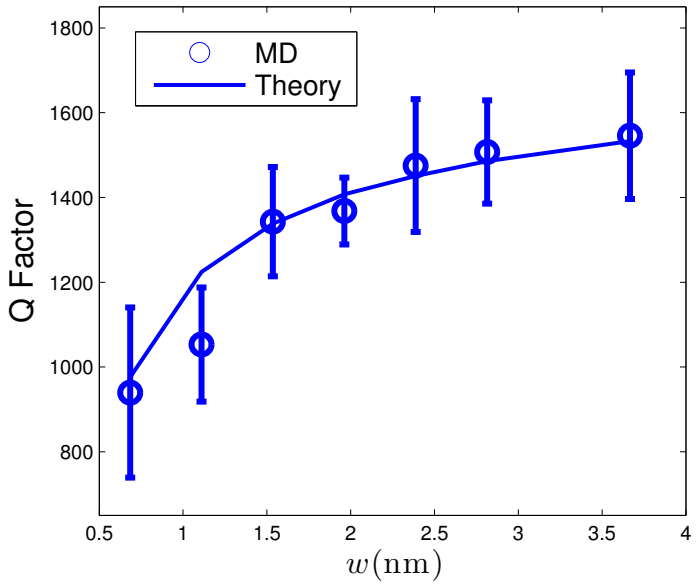

Figure 7.6: Variation of Q factor with width for GNR. The open circles correspond to the result obtained from MD simulation. The solid lines are the result obtained using continuum analysis.

factor may then also be a result of decrease in energy stored. The hydrogen terminated edge atoms of GNR store relatively less energy in comparison with the bulk atoms. In-order to investigate this we computed the quantity $\frac{k}{w}$ for a GNR with width w. For a classical elastic strip with Young's modulus E, stress, σ_{xx}, and strain, ϵ_{xx}, are related as $\sigma_{xx} = E\epsilon_{xx}$. The total force, F, applied at the end is related to σ_{xx} as $F = \sigma_{xx}hw$, where h is thickness and w is width of the strip. The change in length, δ, is related to ϵ_{xx} as $\frac{\delta}{L} = \epsilon_{xx}$, where L is un-deformed length of the strip. k for the strip is given as $k = \frac{F}{\delta}$. Using the relations mentioned before, we obtain

$$\frac{k}{w} = \frac{Eh}{L}. \tag{7.16}$$

$\frac{k}{w}$ for such structure is therefore independent of w (becasue E is a constant for a classical continuum structure). Figure 7.7 shows the plot of $\frac{k}{w}$ vs. w for the case of GNR. The plot shows that $\frac{k}{w}$ decreases with the decrease in size. The structure therefore becomes softer with the increasing contribution of edge atoms.

We develop a continuum expression based on the assumption that the decrease in Q factor with size is primarily due to elastic softening. GNR is represented as an elastic strip. The dissipation rate per unit width, E_w, for a given strain amplitude is assumed to be a constant. E_w is determined by taking the ratio of E_{disp} and w for GNR with maximum width ($w = 3.67$nm). We use E_{disp} for GNR with $w = 3.67$ nm obtained using MD simulation to compute E_w. The value of E_w for $A = 1.0\,\text{Å}$ was estimated to be 1.424 $\frac{\text{ev}}{\text{nm}}$. For a GNR with width w, E_{disp} is then determined as $E_{disp} = wE_w$. Further, using the expression for

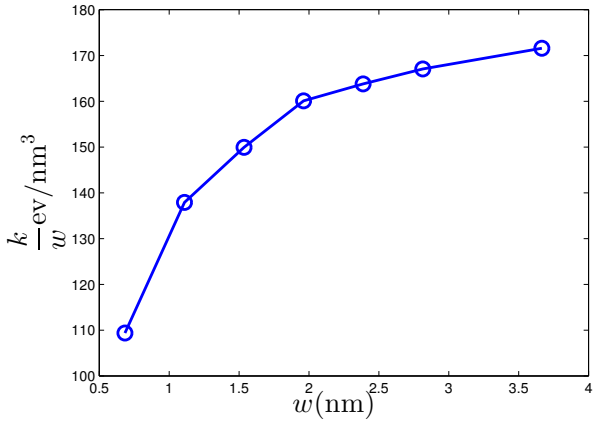

Figure 7.7: Stiffness per unit width as a function of the width of GNR.

E_{stored} in eqn(7.1) Q factor for the elastic strip is obtained as $Q = \frac{2\pi(P_0 A + \frac{1}{2}kA^2)}{E_w w}$. Figure 7.6 shows the plot of Q factor vs. w obtained using this relation. The results are in good agreement with the Q factor computed using MD simulations.

Thus, the drop in Q factor with decrease in size is primarily accounted for by the elastic softening of GNR. The dissipation mechanism discussed before shows that the dissipation rate is a function of τ_1^e and τ_2^e. These are the relaxation times associated with the low and high frequency out-of-plane modes, respectively. The relaxation times are expected to be a function of size. However, we expect the dependence to be weak in comparison with the scaling of $\frac{k}{w}$ with size. The decrease in $\frac{k}{w}$ with the decrease in size then primarily accounts for the observed drop in Q factor.

7.3.4 Temperature Scaling

We studied the effect of temperature on Q factor for GNR with the smallest width. Temperature was varied in the range of 50 K to 300 K. The study was done for a forcing frequency of 40 GHz. Figure 7.8 shows the plot of Q factor vs. temperature. The Q factor increases, and hence dissipation decreases, with the decrease in temperature. Eqn(7.11) shows that $dW \sim a_n^2$. Further, for an oscillator in thermal equilibrium $< a_n^2 > \sim T$. Therefore we expect that $dW \sim T$, assuming other parameters to be constant. As discussed before, the average work done per unit period is a measure of dissipation rate. It can then be concluded that Q factor will scale as $Q \sim T^{-1}$. From the power law fit of the MD data we obtain $Q = AT^{-0.948}$, this is close to T^{-1} scaling.

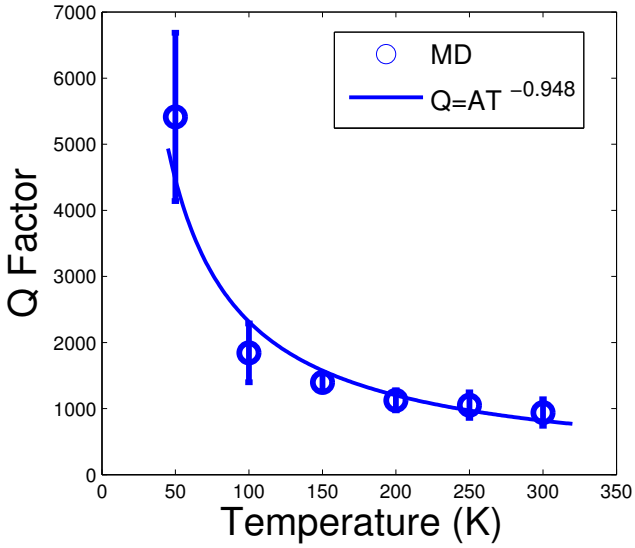

Figure 7.8: Variation of Q factor with temperature for GNR. A power law fit for MD data is also shown.

7.4 Conclusions

The dissipation in GNR under stretching deformation was studied. A non-monotonic dependence of Q factor on the forcing frequency was observed. Using Langevin simulations we identified two mode groups which show opposite variation of dissipation rate with frequency. A bi-relaxation time model was proposed to explain the observed scaling of Q factor. A size study showed that Q factor decreases with the decrease in width. This was attributed to the elastic softening of GNR with decreasing width. The temperature variation of Q factor showed an inverse temperature dependence.

Chapter 8

Conclusions

We used different computational methods to investigate the intrinsic dissipation mechanism in nano-structure. A MD based simulation method was develop to isolate Akhiezer dynamics and study the size and surface effect. We observed that the surface aided in reducing the damping rate for the cases considered. This was understood from the surface scattering of phonons. We, also, identified some deleterious roles of the surface on the Akhiezer damping.

We, then, studied the damping under the flexure mode of operation. The results were compared with the case of stretching deformation. Interestingly, we observed that the Q factor was higher for the bending mode. A reduced order model was considered to understand the observed trend. The role of tension on the Q factor was investigated and a scaling relation was developed.

The next objective of the work involved the development of multi-scale approach to model intrinsic dissipation. We extended the quasi-harmonic framework to describe the non-equilibrium dynamics under high frequencies of vibration. A non-equilibrium stress tensor was derived. A constitutive relation for the time evolution of the non-equilibrium stress was obtained. Methods to obtain the parameters in the constitutive relation were discussed. The method was used to compute the damping rate for different cases. The results were validated against those obtained using MD.

Next, we investigated the thermo-elastic dissipation under high frequency of vibrations. For this purpose, we used the BTE coupled with the elastic strain field. We observed that the finite relaxation time for the heat flux plays an important role under high frequencies of vibration. Corrections to classical expression for the Q factor was provided. Also, the effect of surface scattering on TED was studied.

All of the aforementioned studies involved structures that are essentially three dimensional in nature. We, next, studied the intrinsic dissipation in low dimensional structures. We considered the case of nano-ribbon and two dimensional graphene sheet. A strong coupling between the in-plane and the out-of-plane motion was observed for these structures. We showed that geometric non-linear coupling plays an important role in the loss of energy from the in-plane motion.

Appendix A

A.1 Strain Field

For computing strain field from atomistic data we use a method from previous work [18]. We first provide a brief description of the method. The method is then adapted to deal with the case of a vibrating structure. We consider a collection of atoms. The co-ordinate in the reference configuration for an atom i is given as $\boldsymbol{X}_i$. The system is subjected to a deformation such that the co-ordinate of atom i in the deformed configuration changes to $\boldsymbol{x}_i$. The deformation is assumed to be homogeneous (for non-homogeneous deformation the atoms can be divided into smaller groups such that for each of the smaller groups the deformation is homogeneous). The problem, then, reduces to finding a deformation gradient $\boldsymbol{F}$ that maps $\boldsymbol{X}_i$ into $\boldsymbol{x}_i$. In-order to eliminate rigid body transformation, we consider the motion in the center of mass frame of reference. Let $\boldsymbol{X}_{cm}$ and $\boldsymbol{x}_{cm}$ denote the center of mass for the group of atoms in the reference and deformed configurations, respectively. We define $\boldsymbol{X}_i^c = \boldsymbol{X}_i - \boldsymbol{X}_{cm}$ and $\boldsymbol{x}_i^c = \boldsymbol{x}_i - \boldsymbol{x}_{cm}$. We define tensor $\boldsymbol{A}$ as

$$\boldsymbol{A} = \sum_i \boldsymbol{X}_i \bigotimes \boldsymbol{X}_i \tag{A.1}$$

and $\boldsymbol{B}$ as

$$\boldsymbol{B} = \sum_i \boldsymbol{x}_i \bigotimes \boldsymbol{x}_i \tag{A.2}$$

Here, the symbol $\bigotimes$ refers to the tensor product. In the index notation the components of the tensor product are given as $(\vec{v_1} \bigotimes \vec{v}_2)_{ij} = v_{1i} v_{2j}$, where $\vec{v}_1$ and $\vec{v}_2$ are arbitrary vectors. $\boldsymbol{F}$ is then obtained as

$$\boldsymbol{F} = \boldsymbol{A}\boldsymbol{B}^{-1} \tag{A.3}$$

For a vibrating beam, we have $\boldsymbol{x}_i = \boldsymbol{x}_i(t)$. We computed the strain field for flexure vibration excited in nano-beam using method A. The time instants at which the y co-ordinate of the center of mass attained a maxima were identified. The strain field computation was performed for one such time instant. Let t_1 be

the time instant for which the strain field is determined. We define $\boldsymbol{x}_{ai} = \frac{1}{2\Delta t}\int_{t_1-\Delta t}^{t_1+\Delta t} \boldsymbol{x}_i(t)dt$. Here, Δt is a small time window considered for averaging out the thermal vibrations. The value of Δt was taken to be 200 fs. Since, the structure is dynamically changing one cannot consider a large value of Δt. $\boldsymbol{X}_i$ were taken as the mean equilibrium co-ordinates. The structure was divided into two dimensional bins along x and y directions. The length of bin, in each direction, was taken to be two lattice units. For each bin, $\boldsymbol{B}$ was obtained using Eqn.(A.2) and with $\boldsymbol{x}_i = \boldsymbol{x}_{ai}$. $\boldsymbol{F}$ was then computed using Eqn.(A.3). The Green-Langrangian strain tensor, $\boldsymbol{E}$, is obtained from $\boldsymbol{F}$ as

$$\boldsymbol{E} = \frac{1}{2}\Big(\boldsymbol{F}^T\boldsymbol{F} - \boldsymbol{I}\Big) \tag{A.4}$$

A.2 Mode Shape

The mode shape for the fundamental flexure mode (mode 1) was extracted using the free vibration method from MD. For a beam that is given an initial excitation and undergoes free vibration, the resulting dynamics can be described as a linear combination of the individual modes. Each of the mode behave as a damped harmonic oscillator. The amplitude of the higher order modes decay down rapidly. The resultant displacement profile, then, corresponds to that of mode 1.

We first make an estimate of the decay time for the next higher mode (other than mode 1) that could have been excited. Since the initial velocity perturbation has an anti-node at the center (we used sinusoidal profile for the perturbation), the next higher mode corresponds to mode 3. We consider the case of a nickel beam with cross-sectional area $18\,lc \times 18\,lc$. From beam theory the oscillation frequency, f_3, for mode 3 is estimated to be $f_3 = 96.5568$ GHz. From the observed scaling relation between Q factor and ω, we compute Q_3, the Q factor for mode 3. Q_3 is estimated to be 73.91. From Q_3 the relaxation time for mode 3, τ_3, is determined as $\tau_3 = 243.67$ ps. For $t > \tau_3$ the amplitudes for all the higher modes is expected to decay down appreciably. The dynamic response of the beam will, then, be dominated by the fundamental mode (mode 1). In-order to further check that mode 1 is indeed the dominant mode, we computed the Fourier transform (FFT) of y_{cm}, the y center of mass of the excited beam. Figure A.1 shows the FFT for y_{cm}. The FFT shows a dominant peak corresponding to mode 1 frequency. Mode 1 is, therefore, the dominantly excited mode. Thus, from the displacement profile of the freely vibrating beam mode 1 shape can be inferred.

A velocity perturbation corresponding to a sinusoidal profile was given to the beam. We, then, obtained the displacement profile of the beam after around 500 ps from the initial excitation. The initial time period of 500 ps ensures that all the higher order modes have decayed down. The beam was divided into groups along the length direction. The time at which the y center of mass (com) attained a maximum value was identified. Corresponding to that time instant, the y com of each group was obtained. The y com

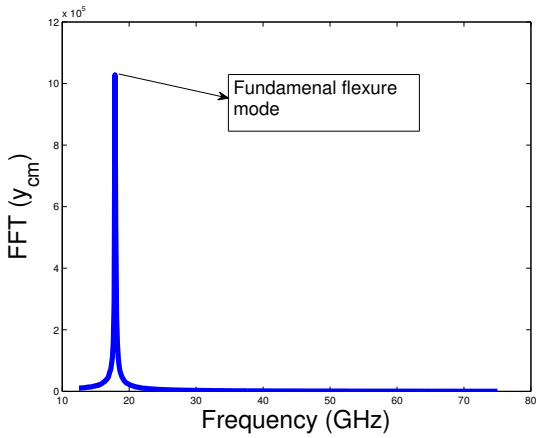

Figure A.1: The FFT of y_{cm} for a beam that was given a velocity perturbation along the y direction.

amplitude of each group gives the displacement profile of the beam under free vibration. Figure A.2 shows the displacement profile obtained. The plot also shows the mode shape obtained using Euler-Bernouli beam theory. The displacement profile obtained from MD shows good agreement with the theoretical mode shape. The displacement profile, as discussed before, corresponds to the fundamental flexure mode.

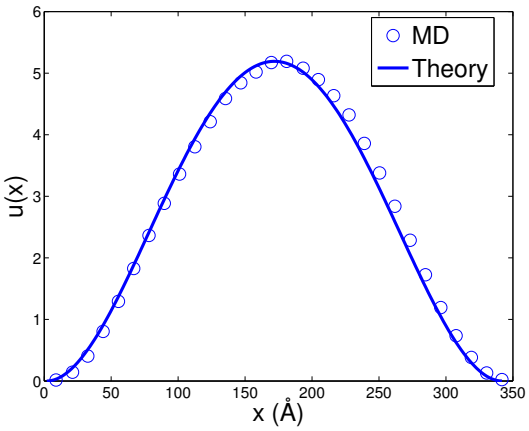

Figure A.2: The displacement profile for a beam under free vibration as obtained using MD. Also, shown is the fundamental mode shape obtained using Euler-Bernouli beam theory.

A.3 Elastic Constants

We use local quasi harmonic method[73] (LQHM) to determine the elastic constants required for beam theory. The free energy, F_i, for an atom i in the LQHM approximation is given as

$$F_i = U_i + \frac{1}{2}\sum_{\alpha=1}^{3}\hbar\omega_{\alpha i} + k_b T\sum_{\alpha=1}^{3} ln(1 - exp^{-\frac{\hbar\omega_{\alpha i}}{k_b T}}) \tag{A.5}$$

Here, U_i is the static potential energy, k_b is the Boltzmann constant, $\hbar$ is the Planck's constant scaled by $\frac{1}{2\pi}$, T is the temperature of system and $\omega_{\alpha i}$ are the vibrational frequencies.

A homogenous cubic crystal is characterized by elastic constants, C_{11}, C_{12} and C_{44}. The presence of surface in a nano-structure modifies these properties. For such a case, the elastic constants are no longer constant but depend on the position of atom. Using LQHM we first determine these constants for each atom. The properties are then averaged over to determine the effective elastic modulus for bending and stretching.

Using elasticity theory, the free energy change, ΔF, for a crystal subjected to strain, ϵ_{ij}, is given as [40]

$$\frac{\Delta F}{V} = \sigma^0_{ij}\epsilon_{ij} + \frac{1}{2}C_{ijkl}\epsilon_{ij}\epsilon_{kl} \tag{A.6}$$

Here, V is the volume of the structure, σ^0_{ij} are the components of residual stress tensor, C_{ijkl} are the elastic constants and ϵ_{ij} are the components of strain tensor.

For a crystal with cubic symmetry and subjected to a strain, $\epsilon_{ij} = \epsilon\delta_{i1}\delta_{j1}$, the above relation reduces to

$$\frac{\Delta F}{V} = \sigma^0_{11}\epsilon + \frac{1}{2}C_{11}\epsilon^2 \tag{A.7}$$

For an atom i with an effective volume V_i, we use the above relation to get $\frac{\Delta F_i}{V_i} = \sigma^{i0}_{11}\epsilon + \frac{1}{2}C^i_{11}\epsilon^2$. Here σ^{0i}_{11} and C^i_{11} are the residual stress and elastic constant associated with atom i. ΔF_i was obtained using Eqn.(A.5) for different values of ϵ. A second-order polynomial fit was performed to get σ^{0i}_{11} and C^i_{11}.

Subjecting the crystal to a strain $\epsilon_{ij} = \epsilon(\delta_{i1}\delta_{j1} - \delta_{i2}\delta_{j2})$ gives $\frac{\Delta F_i}{V_i} = (\sigma^{i0}_{11} - \sigma^{i0}_{22})\epsilon + C^i_{11}\epsilon^2 - C^i_{12}\epsilon^2$. ΔF_i was again obtained using LQHM for different values of ϵ. Using second-order polynomial fit and predetermined values of σ^{i0}_{11} and C^i_{11}, σ^{0i}_{22} and C^i_{12} were determined.

For a cubic crystal, the Young's modulus along the [1 0 0] direction, $E_{[100]}$, is given as [40] $E_{[100]} = C_{11} - 2\frac{C^2_{12}}{C_{11} + C_{12}}$. Thus, the Young's modulus, E_i, associated with atom position i and along the [1 0 0] direction is obtained as $E_i = C^i_{11} - 2\frac{(C^i_{12})^2}{C^i_{11} + C^i_{12}}$. For stretching deformation, all the atoms are subjected to

the same strain. The effective Young's modulus, $E_{stretch}$, is thus derived as

$$E_{stretch} = \frac{\sum_{i=1}^{natoms} E_i}{natoms} \tag{A.8}$$

Table A.1: The values of elastic constants for nickel.

Width (nm)	E_{bend} (GPa)	$E_{stretch}$ (GPa)
3.54	93.379	96.636
4.24	95.743	98.255
4.95	97.551	99.430
5.66	98.881	100.322
6.37	99.874	101.02

Table A.2: The values of elastic constants for copper.

Width (nm)	E_{bend} (GPa)	$E_{stretch}$ (GPa)
3.62	55.165	57.578
4.34	56.760	58.767
5.06	57.913	59.631
5.78	58.786	60.288
6.51	59.470	60.803

For the bending deformation, strain field varies linearly along the lateral direction and the surface atoms experience the maximum strain. The effective Young's modulus in bending, E_{bend}, is, thus, obtained by taking the second moment of E_i along the y axis with the origin as the neutral axis of beam. The neutral axis is defined as the line along which the first moment of Young's modulus vanishes. For a symmetric structure, which is the case here, the neutral axis passes through the beam geometric center in the $y-z$ plane. Let y_i be the y co-ordinate for atoms i with the origin as the neutral axis of beam. E_{bend} is then computed as

$$E_{bend} = \frac{\sum_{i=1}^{natoms} E_i y_i^2}{\sum_{i=1}^{natoms} y_i^2} \tag{A.9}$$

Table A.1 and A.2 provide values of $E_{stretch}$ and E_{bend} for nickel and copper, respectively.

Appendix B

B.1 Non-equilibrium PDF

We derive an expression for the non-equilibrium PDF using the principle of maximum entropy[29, 33]. We consider a collection of $ndof$ harmonic oscillators. Let a_i and v_i denote the displacement and velocity for the ith oscillator. The energy, E_i, for an oscillator i is given as $E_i = \frac{1}{2}m\omega_i^2 + \frac{1}{2}mv_i^2$. Here m is the mass and ω_i denotes the frequency.

We have the following constraints on the system. The mean energy, $< E_n >$, of an oscillator n is given as $< E_n >= kbT_n$. Here, T_n provides a measure of the temperature of the nth oscillator in the non-equilibrium state. We, then, seek to obtain the probability to observe a micro-state i. The PDF is obtained such that the entropy of the system is maximized subject to the imposed constraint. Let A denote the set of the displacement and V denote the set of velocity for all the oscillators for a given micro-state i. Let $P(A, V)$ denote the probability to observe this micro-state. The entropy, S, of the system is then given as

$$S = -\int P(A,V) log P(A,V) dA dV \tag{B.1}$$

The constraint on the mean energy for the nth oscillator is given as

$$\int P(A,V)(\frac{1}{2}m\omega_n^2 a_n^2 + \frac{1}{2}mv_n^2) dA dV = k_b T_n \tag{B.2}$$

We, also, have the normalization constraint as

$$\int P(A,V) dA dV = 1 \tag{B.3}$$

Taking these $ndof + 1$ constraints into account, the extremum problem for the PDF that maximizes the

entropy can be stated as

$$\sup_{P} - \int \left(P(A,V) log P(A,V) + \alpha P + \sum_{n=1}^{ndof} \beta_n (\frac{1}{2} m \omega_n^2 a_n^2 + \frac{1}{2} m v_n^2) P \right) dA dV \tag{B.4}$$

Here, α and β_n are the Lagrange multipliers for enforcing the constraints. Taking the variation of the above Eq. with respect to P we obtain

$$P(A,V) = \frac{1}{Z} \prod_{n=1}^{ndof} exp \left(- \frac{\frac{1}{2} m \omega_n^2 a_n^2 + \frac{1}{2} m v_n^2}{k_b T_n} \right) \tag{B.5}$$

Here, Z is the partition function that normalizes P. We, thus, obtain the PDF for the non-equilibrium state using the maximum entropy principle. We use this PDF to sample the non-equilibrium state and compute the dissipative stress component, σ_{ij}^D

B.2 Stochastic Sampling

The objective of the stochastic sampling approach is to generate the micro-states from a given PDF. For the case of crystalline solids, the PDF is given as a Gaussian function. Using a Gaussian random number generator, the mircostates of a crystalline solid can, therefore, be generated. We will now discuss the details of this algorithm pertaining to our case.

The method requires as an input the mean position of the atoms, the mode eigen-vectors, $\mathbf{e}_i$ and the frequency ω_i. For a perfectly crystalline solid, the mean position of the atoms are generated using the underlying lattice structure. Ni at 300 K has a fcc crystalline structure and was used for our case. Using the mean atomic position the QHM analysis is performed. We, thus, obtain the values of ω_i and $\mathbf{e}_i$. We, next, construct the PDF, $P(a_i)$ for the mode co-ordinates, a_i. For the equilibrium state, $P(a_i)$, is given using Eq.(4.2). For the non-equilibrium state, additional constrains in terms of the mode temperature, T_i, are specified. $P(a_i)$ for such a case is given using Eq.(4.3). We recognize that the PDF for a_i, for either the equilibrium or the non-equilibrium state, are Gaussian functions. Using an algorithm to generate Gaussian random number, different instances of a_i can be obtained. We use the Box-Muller algorithm, and as implemented in the GNU package[16], for our purpose. We, thus, obtain different samples of a_i. For each samples of the a_i values we determine the per atom displacement. Let u_i^j denote the displacement for an atom i along the direction j. u_i^j is obtained from a_n using the linear transformation given as

$$u_i^j = \sum_{n=1}^{nmodes} a_n (e_n)_i^j \tag{B.6}$$

Here, $(e_n)_i^j$ are the components of the eigen-vector $\mathbf{e}_n$ for an atom i along the direction j. For each sample of a_n values, an atomic configuration is thus obtained. The configurations are, then, used to compute the ensemble averages of the required quantities.

References

[1] A. Akhiezer. *Journal of Physics (Moscow)*, 1:277, 1939.

[2] J. Atalaya, A. Isacsson, and J.M. Kinaret. Continuum elastic modeling of graphene resonators. *Nano letters*, 8(12):4196–4200, 2008.

[3] Rustom B Bhiladvala and Z Jane Wang. Effect of fluids on the q factor and resonance frequency of oscillating micrometer and nanometer scale beams. *Physical Review E*, 69(3):036307–036307, 2004.

[4] HE Bömmel and K Dransfeld. Excitation and attenuation of hypersonic waves in quartz. *Physical Review*, 117(5):1245, 1960.

[5] Donald W Brenner, Olga A Shenderova, Judith A Harrison, Steven J Stuart, Boris Ni, and Susan B Sinnott. A second-generation reactive empirical bond order (rebo) potential energy expression for hydrocarbons. *Journal of Physics: Condensed Matter*, 14(4):783, 2002.

[6] J. Scott Bunch, Arend M. van der Zande, Scott S. Verbridge, Ian W. Frank, David M. Tanenbaum, Jeevak M. Parpia, Harold G. Craighead, and Paul L. McEuen. Electromechanical resonators from graphene sheets. *Science*, 315(5811):490–493, 2007.

[7] S Chakram, YS Patil, L Chang, and M Vengalattore. Dissipation in ultrahigh quality factor sin membrane resonators. *Physical review letters*, 112(12):127201, 2014.

[8] Changyao Chen, Sami Rosenblatt, Kirill I Bolotin, William Kalb, Philip Kim, Ioannis Kymissis, Horst L Stormer, Tony F Heinz, and James Hone. Performance of monolayer graphene nanomechanical resonators with electrical readout. *Nature nanotechnology*, 4(12):861–867, 2009.

[9] Garrett D Cole, Ignacio Wilson-Rae, Katharina Werbach, Michael R Vanner, and Markus Aspelmeyer. Phonon-tunnelling dissipation in mechanical resonators. *Nature communications*, 2:231, 2011.

[10] Sudipto K De and NR Aluru. Theory of thermoelastic damping in electrostatically actuated microstructures. *Physical Review B*, 74(14):144305, 2006.

[11] A. Eichler, J. Moser, J. Chaste, M. Zdrojek, I. Wilson-Rae, and A. Bachtold. Nonlinear damping in mechanical resonators made from carbon nanotubes and graphene. *Nature nanotechnology*, 6(6):339–342, 2011.

[12] O Ergincan, G Palasantzas, and BJ Kooi. Influence of surface modification on the quality factor of microresonators. *Physical Review B*, 85(20):205420, 2012.

[13] A. Fasolino, J. H. Los, and M. I. Katsnelson. Intrinsic ripples in graphene. *Nat Mater*, 6(11):858–861, 2007.

[14] SM Foiles, MI Baskes, and MS Daw. Embedded-atom-method functions for the fcc metals cu, ag, au, ni, pd, pt, and their alloys. *Physical Review B*, 33(12):7983, 1986.

[15] Moshe Gitterman. *The noisy oscillator: the first hundred years, from Einstein until now*. World Scientific, 2005.

[16] Brian Gough. *GNU scientific library reference manual*. Network Theory Ltd., 2009.

[17] P Alex Greaney, Giovanna Lani, Giancarlo Cicero, and Jeffrey C Grossman. Anomalous dissipation in single-walled carbon nanotube resonators. *Nano letters*, 9(11):3699–3703, 2009.

[18] PM Gullett, MF Horstemeyer, MI Baskes, and H Fang. A deformation gradient tensor and strain tensors for atomistic simulations. *Modelling and Simulation in Materials Science and Engineering*, 16(1):015001, 2008.

[19] FL Guo, J Song, GQ Wang, and YF Zhou. Analysis of thermoelastic dissipation in circular micro-plate resonators using the generalized thermoelasticity theory of dual-phase-lagging model. *Journal of Sound and Vibration*, 333(11):2465–2474, 2014.

[20] MS Hanay, S Kelber, AK Naik, D Chi, S Hentz, EC Bullard, E Colinet, L Duraffourg, and ML Roukes. Single-protein nanomechanical mass spectrometry in real time. *Nature nanotechnology*, 7(9):602–608, 2012.

[21] Zhili Hao. Thermoelastic damping in the contour-mode vibrations of micro-and nano-electromechanical circular thin-plate resonators. *Journal of Sound and Vibration*, 313(1):77–96, 2008.

[22] Zhili Hao, Yang Xu, and Shiva Krishna Durgam. A thermal-energy method for calculating thermoelastic damping in micromechanical resonators. *Journal of Sound and Vibration*, 322(4):870–882, 2009.

[23] GO Harding and J Wilks. The absorption of sound in dilute solutions of 3 he in liquid helium ii. volume 268, pages 424–436. The Royal Society, 1962.

[24] J Hasson and A Many. Observation of akhiezer and landau-rumer regimes in the frequency dependence of shear-wave lattice attenuation in cds. *Physical Review Letters*, 35(12):792, 1975.

[25] P Heino and Eero Ristolainen. Thermal conduction at the nanoscale in some metals by md. *Microelectronics journal*, 34(9):773–777, 2003.

[26] SP Hepplestone and GP Srivastava. The lattice dynamics of rectangular silicon nanowires. *physica status solidi (c)*, 1(11):2617–2620, 2004.

[27] B Ilic, Y Yang, K Aubin, R Reichenbach, S Krylov, and HG Craighead. Enumeration of dna molecules bound to a nanomechanical oscillator. *Nano Letters*, 5(5):925–929, 2005.

[28] EA Ilin, J Kehrbusch, B Radzio, and E Oesterschulze. Analytical model of the temperature dependent properties of microresonators immersed in a gas. *Journal of Applied Physics*, 109(3):033519, 2011.

[29] Edwin T Jaynes. Information theory and statistical mechanics. *Physical review*, 106(4):620, 1957.

[30] H Jiang, M-F Yu, B Liu, and Y Huang. Intrinsic energy loss mechanisms in a cantilevered carbon nanotube beam oscillator. *Physical review letters*, 93(18):185501, 2004.

[31] Sung Youb Kim and Harold S. Park. The importance of edge effects on the intrinsic loss mechanisms of graphene nanoresonators. *Nano Letters*, 9(3):969–974, 2009.

[32] AA Kiselev and GJ Iafrate. Phonon dynamics and phonon assisted losses in euler-bernoulli nanobeams. *Physical Review B*, 77(20):205436, 2008.

[33] Yashashree Kulkarni, Jaroslaw Knap, and Michael Ortiz. A variational approach to coarse graining of equilibrium and non-equilibrium atomistic description at finite temperature. *Journal of the Mechanics and Physics of Solids*, 56(4):1417–1449, 2008.

[34] Russell M Kulsrud. Adiabatic invariant of the harmonic oscillator. *Physical Review*, 106(2):205, 1957.

[35] K Kunal and NR Aluru. Akhiezer damping in nanostructures. *Physical Review B*, 84(24):245450, 2011.

[36] K Kunal and NR Aluru. Intrinsic loss due to unstable modes in graphene. *Nanotechnology*, 24(27):275701, 2013.

[37] K Kunal and NR Aluru. Phonon mediated loss in a graphene nanoribbon. *Journal of Applied Physics*, 114(8):084302, 2013.

[38] K Kunal and NR Aluru. Intrinsic dissipation in a nano-mechanical resonator. *Journal of Applied Physics*, 116(9):094304, 2014.

[39] SD Lambade, GG Sahasrabudhe, and S Rajagopalan. Temperature dependence of acoustic attenuation in silicon. *Physical Review B*, 51(22):15861, 1995.

[40] Lev D Landau and EM Lifshitz. Theory of elasticity, vol. 7. *Course of Theoretical Physics*, 3:109, 1986.

[41] Changgu Lee, Xiaoding Wei, Jeffrey W. Kysar, and James Hone. Measurement of the elastic properties and intrinsic strength of monolayer graphene. *Science*, 321(5887):385–388, 2008.

[42] MF Lewis. Attenuation of longitudinal ultrasonic waves in insulators at room temperature. *The Journal of the Acoustical Society of America*, 43(4):852–858, 1968.

[43] Pu Li, Yuming Fang, and Rufu Hu. Thermoelastic damping in rectangular and circular microplate resonators. *Journal of Sound and Vibration*, 331(3):721–733, 2012.

[44] Ron Lifshitz. Phonon-mediated dissipation in micro-and nano-mechanical systems. *Physica B: Condensed Matter*, 316:397–399, 2002.

[45] Ron Lifshitz and Michael L Roukes. Thermoelastic damping in micro-and nanomechanical systems. *Physical review B*, 61(8):5600, 2000.

[46] Yuyuan Lin, James A McCarthy, Kenneth R Poeppelmeier, and Laurence D Marks. Applications of electron microscopy in heterogeneous catalysis. *Catalysis by Materials with Well-Defined Structures*, page 193, 2015.

[47] Harold Wesley Lord and Y Shulman. A generalized dynamical theory of thermoelasticity. *Journal of the Mechanics and Physics of Solids*, 15(5):299–309, 1967.

[48] Warren P Mason and TB Bateman. Ultrasonic-wave propagation in pure silicon and germanium. *The Journal of the Acoustical Society of America*, 36(4):644–652, 1964.

[49] AJH McGaughey and M Kaviany. Thermal conductivity decomposition and analysis using molecular dynamics simulations. part i. lennard-jones argon. *International Journal of Heat and Mass Transfer*, 47(8):1783–1798, 2004.

[50] Alan JH McGaughey and M Kaviany. Quantitative validation of the boltzmann transport equation phonon thermal conductivity model under the single-mode relaxation time approximation. *Physical Review B*, 69(9):094303, 2004.

[51] Donald Allan McQuarrie. *Statistical thermodynamics*. HarperCollins Publishers, 1973.

[52] Aydin Nabovati, Daniel P Sellan, and Cristina H Amon. On the lattice boltzmann method for phonon transport. *Journal of Computational Physics*, 230(15):5864–5876, 2011.

[53] AK Naik, MS Hanay, WK Hiebert, XL Feng, and ML Roukes. Towards single-molecule nanomechanical mass spectrometry. *Nature nanotechnology*, 4(7):445–450, 2009.

[54] K S Novoselov, A K Geim, S V Morozov, D Jiang, M I Katsnelson, I V Grigorieva, S V Dubonos, and A A Firsov. Two-dimensional gas of massless dirac fermions in graphene. *Nature*, 438(7065):197–200, 2005.

[55] Pär AT Olsson. Transverse resonant properties of strained gold nanowires. *Journal of Applied Physics*, 108(3):034318, 2010.

[56] G Palasantzas. Quality factor due to roughness scattering of shear horizontal surface acoustic waves in nanoresonators. *Journal of Applied Physics*, 104(5):053524, 2008.

[57] Matthew Pelton, John E Sader, Julien Burgin, Mingzhao Liu, Philippe Guyot-Sionnest, and David Gosztola. Damping of acoustic vibrations in gold nanoparticles. *Nature nanotechnology*, 4(8):492–495, 2009.

[58] Matthew Pelton, Yiliang Wang, David Gosztola, and John E Sader. Mechanical damping of longitudinal acoustic oscillations of metal nanoparticles in solution. *The Journal of Physical Chemistry C*, 115(48):23732–23740, 2011.

[59] Steve Plimpton. Fast parallel algorithms for short-range molecular dynamics. *Journal of computational physics*, 117(1):1–19, 1995.

[60] Sairam Prabhakar and Srikar Vengallatore. Theory of thermoelastic damping in micromechanical resonators with two-dimensional heat conduction. *Microelectromechanical Systems, Journal of*, 17(2):494–502, 2008.

[61] G. Radons, B. Rumpf, and H.G. Schuster. *Nonlinear Dynamics of Nanosystems*. John Wiley & Sons, 2010.

[62] Laura G Remus, Miles P Blencowe, and Yukihiro Tanaka. Damping and decoherence of a nanomechanical resonator due to a few two-level systems. *Physical Review B*, 80(17):174103, 2009.

[63] Johannes Rieger, Andreas Isacsson, Maximilian J Seitner, Jörg P Kotthaus, and Eva M Weig. Energy losses of nanomechanical resonators induced by atomic force microscopy-controlled mechanical impedance mismatching. *Nature communications*, 5, 2014.

[64] Paul V Ruijgrok, Peter Zijlstra, Anna L Tchebotareva, and Michel Orrit. Damping of acoustic vibrations of single gold nanoparticles optically trapped in water. *Nano letters*, 12(2):1063–1069, 2012.

[65] C. Seoánez, F. Guinea, and A. H. Castro Neto. Dissipation in graphene and nanotube resonators. *Phys. Rev. B*, 76:125427, 2007.

[66] C Seoánez, F Guinea, and AH Castro Neto. Surface dissipation in nanoelectromechanical systems: Unified description with the standard tunneling model and effects of metallic electrodes. *Physical Review B*, 77(12):125107, 2008.

[67] JN Sharma and R Sharma. Damping in micro-scale generalized thermoelastic circular plate resonators. *Ultrasonics*, 51(3):352–358, 2011.

[68] Gyaneshwar P Srivastava. *The physics of phonons*. CRC Press, 1990.

[69] Michael A Stroscio and Mitra Dutta. *Phonons in nanostructures*. Cambridge University Press, 2001.

[70] Steven J. Stuart, Alan B. Tutein, and Judith A. Harrison. A reactive potential for hydrocarbons with intermolecular interactions. *The Journal of Chemical Physics*, 112(14):6472–6486, 2000.

[71] Yuxin Sun, Daining Fang, and Ai Kah Soh. Thermoelastic damping in micro-beam resonators. *International Journal of Solids and Structures*, 43(10):3213–3229, 2006.

[72] Z Tang and NR Aluru. Calculation of thermodynamic and mechanical properties of silicon nanostructures using the local phonon density of states. *Physical Review B*, 74(23):235441, 2006.

[73] Z Tang, H Zhao, G Li, and NR Aluru. Finite-temperature quasicontinuum method for multiscale analysis of silicon nanostructures. *Physical Review B*, 74(6):064110, 2006.

[74] Quirin P Unterreithmeier, Thomas Faust, and Jörg P Kotthaus. Damping of nanomechanical resonators. *Physical review letters*, 105(2):027205, 2010.

[75] Joseph F Vignola, John A Judge, Jacek Jarzynski, Maxim Zalalutdinov, Brian H Houston, and Jeffrey W Baldwin. Effect of viscous loss on mechanical resonators designed for mass detection. *Applied Physics Letters*, 88(4):041921, 2006.

[76] TO Woodruff and H Ehrenreich. Absorption of sound in insulators. *Physical Review*, 123(5):1553, 1961.

[77] Arend M van der Zande, Robert A Barton, Jonathan S Alden, Carlos S Ruiz-Vargas, William S Whitney, Phi HQ Pham, Jiwoong Park, Jeevak M Parpia, Harold G Craighead, and Paul L McEuen. Large-scale arrays of single-layer graphene resonators. *Nano letters*, 10(12):4869–4873, 2010.

[78] Clarence Zener. Internal friction in solids. i. theory of internal friction in reeds. *Physical review*, 52(3):230, 1937.

[79] H Zhao, K Min, and NR Aluru. Size and chirality dependent elastic properties of graphene nanoribbons under uniaxial tension. *Nano letters*, 9(8):3012–3015, 2009.

[80] H Zhao, Z Tang, G Li, and NR Aluru. Quasiharmonic models for the calculation of thermodynamic properties of crystalline silicon under strain. *Journal of Applied Physics*, 99(6):064314, 2006.

[81] Guiti Zolfagharkhani, Alexei Gaidarzhy, Pascal Degiovanni, Stefan Kettemann, Peter Fulde, and Pritiraj Mohanty. Nanomechanical detection of itinerant electron spin flip. *Nature nanotechnology*, 3(12):720–723, 2008.

[82] Jie Zou and Alexander Balandin. Phonon heat conduction in a semiconductor nanowire. *Journal of Applied Physics*, 89(5):2932–2938, 2001.